2009

Semi-Automatic Segmentation of Normal Female Pelvic Floor Structures from Magnetic Resonance Images

Xiaolong Li
Cleveland State University

Recommended Citation

Li, Xiaolong, "Semi-Automatic Segmentation of Normal Female Pelvic Floor Structures from Magnetic Resonance Images" (2009). *ETD Archive*. 181.
https://engagedscholarship.csuohio.edu/etdarchive/181

SEMI-AUTOMATIC SEGMENTATION OF NORMAL FEMALE PELVIC FLOOR STRUCTURES FROM MAGNETIC RESONANCE IMAGES

XIAOLONG LI

Bachelor of Engineering in Automation

Nantong University

July, 1999

Master of Science in Mechanical Engineering

Cleveland State University

August, 2004

Submitted in partial fulfillment of requirements for the degree

DOCTOR OF ENGINEERING IN APPLIED BIOMEDICAL ENGINEERING

at the

CLEVELAND STATE UNIVERSITY

November, 2009

This dissertation has been approved

for the Department of Chemical and Biomedical Engineering

and the College of Graduate Studies by

Dissertation Chairperson, Margot S. Damaser

Department of Chemical and Biomedical Engineering
Department & Date

George P. Chatzimavroudis

Department of Chemical and Biomedical Engineering
Department & Date

Paul P. Lin

Department of Mechanical Engineering
Department & Date

Yongjian Fu

Department of Electrical and Computer Engineering
Department & Date

Yuping Wu

Department of Mathematics
Department & Date

ACKNOWLEDGEMENT

I would like to acknowledge my enormous debt to my advisor, Dr. Margot S. Damaser. Her patience, scientifically skeptical nature, and uncannily accurate insights helped me to become more sophisticated in my academic research and make this dissertation finally possible. She is more than an advisor; she is also a mentor, friend and guide in my life.

I would also like to thank Dr. Paul P. Lin for his encouragement and support to convince me pursuing my graduate study. Very little research would have been possible without the guidance and advice from my committee members. I would especially like to thank Dr. George Chatzimavroudis, Dr. Yongjian Fu and Dr. Yuping Wu for all the help and support.

I thank my father Zhongqun Li and mother Peixiu Gu, who have supported and loved me thought my life. This would not have been possible without them. I also need to thank my parents-in-law, who give me reassurance and assistance whenever I was in need.

Finally, thank you to my wife, Haiyan Zhang, for her patience, understanding, and indomitable spirit, which provides an unfailing source of inspiration.

SEMI-AUTOMATIC SEGMENTATION OF NORMAL FEMALE PELVIC FLOOR STRUCTURES FROM MAGNETIC RESONANCE IMAGES

XIAOLONG LI

ABSTRACT

Stress urinary incontinence (SUI) and pelvic organ prolapse (POP) are important health issues affecting millions of American women. Investigation of the cause of SUI and POP requires a better understand of the anatomy of female pelvic floor. In addition, pre-surgical planning and individualized treatment plans require development of patient-specific three-dimensional or virtual reality models. The biggest challenge in building those models is to segment pelvic floor structures from magnetic resonance images because of their complex shapes, which make manual segmentation labor-intensive and inaccurate. In this dissertation, a quick and reliable semi-automatic segmentation method based on a shape model is proposed. The model is built on statistical analysis of the shapes of structures in a training set. A local feature map of the target image is obtained by applying a filtering pipeline, including contrast enhancement, noise reduction, smoothing, and edge extraction. With the shape model and feature map, automatic segmentation is performed by matching the model to the border of the structure using an optimization technique called evolution strategy. Segmentation performance is evaluated by calculating a similarity coefficient between semi-automatic and manual segmentation results. Taguchi analysis is performed to investigate the significance of segmentation parameters and provide tuning trends for better performance. The proposed method was successfully tested on both two-dimensional and three-dimensional image segmentation using the levator ani and obturator muscles as examples. Although the method is designed for segmentation of female pelvic floor structures, it can also be applied to other structures or organs without large shape variation.

TABLE OF CONTENTS

Page

ABSTRACT iv

LIST OF TABLES xii

LIST OF FIGURES xiii

TABLE OF CONTENTS vi

CHAPTER I 1

INTRODUCTION 1

- 1.1 SUI and POP 1
- 1.2 Anatomy of the Female Pelvic Floor 3
  - 1.2.1 Pelvic Bones 3
  - 1.2.2 Levator Ani Muscle 4
  - 1.2.3 Obturator Muscles 4
  - 1.2.4 Vagina 4
  - 1.2.5 Urethra 5
  - 1.2.6 Bladder 5
  - 1.2.7 Uterus 5
  - 1.2.8 Rectum 6
- 1.3 2D, 3D and VR Models of Female Pelvic Floor 6

1.3.1 ‘Real’ World View 9

1.3.2 Node Structure Model 10

1.3.3 Integrated Model 11

1.4 Problem Statement 11

1.4.1 Time-consuming Property 12

1.4.2 Lack of Reproducibility 12

1.5 Objective of Dissertation 13

1.5.1 Easily Extend from 2D models to 3D models 14

1.5.2 Robust 14

1.5.3 Smart 14

1.5.4 Objectively Evaluate Performance 15

1.6 Overview of Dissertation 15

CHAPTER II 17

AN OVERVIEW ON MEDICAL IMAGING AND MEDICAL IMAGE SEGMENTATION 17

2.1 Medical Imaging Modalities 17

2.1.1 Computed Tomography (CT) 18

2.1.2 Ultrasound 20

2.1.3 Magnetic Resonance Imaging (MRI) 23

2.2 Introduction of Medical Image Segmentation 25

2.2.1 Visualization 26

2.2.2 Quantitative Measurement 27

2.2.3 Pre-surgical Planning and Image-guided Surgery 28

2.2.4 Detection of Change 29

2.3 Image Segmentation Techniques 29

2.3.1 Model-free Segmentation Techniques 30

2.3.2 Model-based Segmentation Techniques 37

2.4 Conclusion 43

2.4.1 Imaging Modalities and Image Quality 44

2.4.2 Properties of the Structures in Images 44

2.4.3 Requirements of Application 45

CHAPTER III 46

PROPOSED SEMI-AUTOMATIC SEGMENTATION METHOD 46

3.1 Challenges for Semi-automatic Segmentation of Medical Images 46

3.1.1 Diffuse in Intensity Value 46

3.1.2 Limited In-plan Resolution 47

3.1.3 Difficult to Separate Objects 47

3.2 Model-Based Semi-automatic Segmentation 48

3.2.1 Robust 48

3.2.2 Statistical Analysis to Provide Prior Knowledge 49

3.3 Limitation of Landmark-Based Statistical Model 50

3.4 Overview of Proposed Semi-automatic Segmentation Method 52

3.4.1 Using Distance Field Instead of Landmarks 52

3.4.2 Using Centered Affine Transform to Align Shape model......................... 54

3.4.3 Extraction of Local Image Features by Designed Filter Sequence 54

3.4.4 Using Evolutionary Strategy for Model Matching.................................... 55

3.4.5 Using Taguchi Analysis to Improve the Performance of Segmentation..... 56

CHAPTER IV 59
BUILDING STATISTICAL SHAPE MODEL 59
4.1 Introduction 59

4.2 Training Set Preparation... 64

4.2.1 Performance Requirement... 66

4.2.2 Properties of Target Structures.. 66

4.2.3 Segmentation Results 66

4.3 Manual Segmentation of Training Set Images 67

4.4 Alignment of Segmented Images 70

4.5 Calculating Distance Maps of Aligned Shape Images 77

4.6 Principle Component Analysis 83

CHAPTER V.. 91
LOCAL FEATURE MAP AND MODEL MATCHING 91
5.1 Introduction 91

5.2 Import MRI Data 92

5.3 Window and Level Operation... 92

5.3.1 Linear Mapping 94

5.3.2 Normalized Mapping 95

5.3.3 Histogram Mapping 96

5.3.4 Nonlinear Mapping 97

5.3.5 Noise Reduction 99

5.4 Gradient Calculation 103

5.5 Normalization 108

5.6 Model Matching 109

CHAPTER VI 114
PERFORMANCE EVALUATION AND TAGUCHI ANALYSIS 114
6.1 Performance Evaluation of Segmentation Method 114

6.2 Taguchi Analysis 115

6.2.1 Background of Taguchi Analysis 116

6.2.2 Experimental Design Using Orthogonal Arrays 117

6.2.3 Analyze Performance Using S/N Ratio 122

6.2.4 Significance and Tuning Trend of Parameters 126

6.2.5 Apply Taguchi Method to Proposed Segmentation Method 126

CHAPTER VII 130
TESTING RESULTS 130
7.1 Segmentation Tests 130

7.2 2D Segmentation on the Levator Ani Muscle 132

7.2.1 Build Statistical Model ... 133

7.2.2 Generate Feature Map of Unseen Data ... 136

7.2.3 Model Matching ... 137

7.2.4 Taguchi Analysis ... 138

7.3 3D Segmentation on Obturator Muscles ... 141

7.3.1 Build Statistical Model ... 142

7.3.2 Generate Feature Map of Unseen Data ... 144

7.3.3 Model Matching Results ... 145

7.3.4 Taguchi Analysis ... 147

CHAPTER VIII ... 150

CONCLUSIONS AND FUTURE WORK ... 150

8.1 Conclusions ... 150

8.2 Future Work ... 153

8.2.1 Performance Improvment ... 153

8.2.2 Automatically Build VR Model of Female Pelvic Floor ... 155

REFERENCE ... 158

LIST OF TABLES

Table Page

Table I Complete Experimental Runs with Three 2-Level Variables 119

Table II Taguchi Orthogonal Array for Three 2-level Variables 119

Table III Taguchi Orthogonal Array for Two Interaction Variables 120

Table IV Taguchi Orthogonal Arrays 121

Table V L9 Orthogonal Array and Linear Graph 122

Table VI L27 Orthogonal Array and Linear Graph 127

Table VII Orthogonal Array for Seven 3-level Control Parameters 128

Table VIII Taguchi Control Factors Table 138

Table IX Taguchi L27 Orthogonal Table 139

Table X S/N Table 140

Table XI Significance Index and Trend 140

Table XII Taguchi L27 Orthogonal Table 147

Table XIII S/N Table 148

Table XIV Significance Index and Trend 148

LIST OF FIGURES

Figure Page

Figure 1 Sagittal Section of Female Pelvis (From Gray 1918[23]) 6

Figure 2 Coronal 3D model of female pelvis (Fielding 2000 [24]) 7

Figure 3 VR model of normal female pelvic floor (Damaser 2004) 9

Figure 4 ImmersaDesk Used to Demonstrate VR Model 10

Figure 5 Sample MRI Scan of Female Pelvic Floor 13

Figure 6 Multislice CT (MSCT) 19

Figure 7 Doppler Ultrasound 22

Figure 8 MRI Scanner 24

Figure 9 Reconstruction of Head Anatomy 27

Figure 10 Paranasal Cavities 28

Figure 11 FMRI Segmentation of Human Brain 29

Figure 12 Binary Thresholding 32

Figure 13 Canny Edge Detection for Pelvic Floor MR Image 34

Figure 14 Segmentation of Brain MRI by Using Region Growing Method 36

Figure 15 Segmentation of MRI by Using Active Contour Method 40

Figure 16 Landmarks of Face (T F Cootes 1998) 51

Figure 17 Framework of Proposed Segmentation Method 57

Figure 18 CT Scan of the Female Pelvic Floor 60

Figure 19 Ultrasound of Female Pelvic Floor 61

Figure 20 MRI Scan of Female Pelvic Floor 62

Figure 21 Flow Chart of Building Statistical Model 64

Figure 22 Examples of Training Set Images 65

Figure 23 Manual Segmentation Using Polygon Toolbox (ITK-SNAP) 68

Figure 24 Node Link Map of Live Wire Algorithm 69

Figure 25 Manual Segmentation of the Levator Ani Muscle with Live Wire 70

Figure 26 Affine Transformation 71

Figure 27 Centered Affine Transformations 75

Figure 28 Parameters for Center Affine Transformation 76

Figure 29 Flowchart of Shape Alignment 77

Figure 30 Distance Map 78

Figure 31 Euclidean Distance Map 79

Figure 32 City Block Distance Map 80

Figure 33 Chessboard Distance Map 81

Figure 34 Quasi-Euclidean Distance Map 82

Figure 35 Example of Signed Distance Map 83

Figure 36 Example of Performing PCA on 2D Data Set 85

Figure 37 Example of Window Operation 93

Figure 38 Linear Intensity Mapping 95

Figure 39 Sigmoid Function 98

Figure 40 Modified Sigmoid Intensity Mapping 99

Figure 41 5x5 Discrete Gaussian Smoothing Kernel 101

Figure 42 Example of Anisotropic Diffusion Smoothing 103

Figure 43 Example of Pixels (1) 106

Figure 44 Example of Pixels (2) 107
Figure 45 Example of Gradient Magnitude Normalization 108
Figure 46 Example of Ineffective Model Free Methods 132
Figure 47 Examples of Aligned Levator Ani Muscle 134
Figure 48 A Signed Distance Map of Levator Ani Muscle 135
Figure 49 A Signed Distance Map of Mean Shape and Shape Variation Model 135
Figure 50 Processing of Unseen Data 136
Figure 51 Model Matching Method for Levator Ani Muscle 137
Figure 52 Isosurface of Aligned Shapes of Obturator Muscles from (a) to (h) 142
Figure 53 3D Distance Map of Obturator Muscles from (a) to (h) 143
Figure 54 Shape Model of Obturator Muscles Sample from (a) to (d) 144
Figure 55 Feature Map of Unseen Data 145
Figure 56 Model Matching for Obturator Muscles 146
Figure 57 Overlap of MR Image and Segmentation Result of Obturator Muscles 146
Figure 58 A Combined Model of the Levator Ani Muscle and Obturator Muscles 155
Figure 59 3D Segmentation of the Vessel 156
Figure 60 Segmentation Result with Axial and Coronal MRI Scans 157

CHAPTER I

INTRODUCTION

1.1 SUI and POP

Stress urinary incontinence (SUI) and pelvic organ prolapse (POP) are important health issues that affect millions of American women at a cost of approximately $20 billion annually [1]. According to one study, the population of woman over eighty is the fastest growing segment in the United States and the rate of women who will seek treatment for SUI and POP will double over the next thirty years [2].

Urinary incontinence (UI), which means involuntary loss of urine, has been reported to affect 35% of American women over 50 years of age [3]. UI can be categorized into different types, including stress urinary incontinence, urge incontinence, mixed incontinence, functional incontinence, overflow incontinence, transient continence and deformity incontinence [4]. Among all those types of incontinence, SUI is the most common type and much more prevalent in women than in men [5]. According to current research, approximately 60% of women with incontinence will have stress incontinence [6].

SUI, also called effort incontinence, is any involuntary leakage of urine associated with sneezing, coughing, laughing, or other movement that increases the intra-abdominal pressure, which in turn increases the pressure on the bladder. In females, the urethra is located behind the public symphysis and is supported by numerous structures, including the endopelvic fascia, the anterior vagina, and the arcus tendineus fascia pelvis. If such supports are weakened, the urethra can move downward when abdominal pressure increases and cause urine leakage. For women, some SUI can be caused by physical changes such as pregnancy, childbirth, and menopause. It is reported that 30 percent of women will develop SUI within 5 years after their first vaginal delivery [7].

POP is a common problem especially among older women. It is estimated over 50 percent of the women who have vaginal delivery will experience some form of prolapse in later life [8]. The female pelvic organs, such as uterus, vagina, and bladder are surrounded by a network of muscles, ligaments, and connective tissue that act as a complex support structure that holds those organs in place. POP occurs when the support system weakens or collapses, causing a pelvic organ to slip out of its normal position. Types of POP includes disorders of the anterior vaginal compartment, the posterior vaginal compartment, the apical compartment (uterus or post-hysterectomy vaginal apex), the recto-vaginal space, and the perineum [9]. The typical symptom associated with POP is SUI, and other symptoms include pressure and pain, bowel symptoms and sexual problems [9].

1.2 Anatomy of the Female Pelvic Floor

In recent years, a great deal of research([10], [11], [12]) has been done on investigating the cause of incontinence and prolapse and yet it remains elusive. Part of the reason is limited knowledge of the anatomy of the female pelvic floor. The main components of the female pelvic floor are pelvic bones, bladder, urethra, vagina, uterus, rectum, levator ani muscle, and obturator muscles. The female pelvic floor not only provides support for pelvic organs, such as the bladder, intestines, the uterus, but also is important in maintenance of continence as part of the urinary and anal sphincters [13]. The details about each structures of female pelvic floor are described in the following subsections.

1.2.1 Pelvic Bones

The bony structure of the pelvis is located at the base of spine and composed of several bones: ilium, ischium, public rami, sacrum, and coccyx (tailbone). The pelvic bones are the rigid foundation in which all of the pelvic floor structures anchor [14].

1.2.2 Levator Ani Muscle

Levator ani muscle is a funnel-shaped diaphragm in the pelvis between the lateral hip walls, the pubis anteriorly and the coccyx posteriorly. It is traversed by urethra, vagina, and rectum. The levator ani is the main muscle of the pelvic floor and has a complex shape, which is composed of several separate muscle parts including pubovaginalis, coccygeus, iliococcygeus, pubococcygeus, and puborectalis. It has a crucial role in the maintenance of continence, and damage to the levator ani muscle has been considered a main cause of POP[15].

1.2.3 Obturator Muscles

Obturator muscles lie on the intrapelvic side of the obturator membrane. The origin of the obturator muscles comes from the inferior margin of the intrapelvic pubic ramus and the pelvic surface of the obturator membrane [16]. The obturator muscles are the lateral boundary of the pelvic sidewall and contain the pelvic contents laterally, provide powerful, lateral rotation of the thigh and assist in maintaining the head of the femur in the acetabulum [17].

1.2.4 Vagina

The vagina is a fibromuscular tube with rugal folds that located in the front of the rectum and behind the bladder. The length of the vagina is 8.9 cm on average. The muscular wall of vagina is thin and composed of three layers: mucosa, muscularis, and adventitia [18].

1.2.5 Urethra

The female urethra originates at the trigone of the bladder and terminates anterior at the urethral meatus. The urethra is about 3.5 to 4 cm long and averages 0.6 cm in diameter. Most part of the urethra is merged into the anterior vaginal wall [19]. The urethra has three layers: the inner mucosal layer, the highly vascular submucosal layer and the outer muscular [14].

1.2.6 Bladder

The bladder is pyramidal in shape, with its apex pointing anteriorly towards the superior portion of the public symphysis. The bladder consists of four layers: an outer adventitial layer of connective tissue, a nonstriated muscle layer, a lamina propria, and an inner layer of mucosa [20].

1.2.7 Uterus

The uterus is located inside the pelvis close to urinary bladder and the rectum. The uterus can be divided into three major segments: the fundus of uterus, the corpus uteri and the cervix [21].

1.2.8 Rectum

The rectum is about 20 cm long on average which hooks up with the sigmoid colon at the proximal end and with the anal canal at the distal end [22].

1.3 2D, 3D and VR Models of Female Pelvic Floor

In order to understand the functions of the female pelvic floor, especially how the structures provide support for organs and affect continence and prolapse, a model of the female pelvic floor is required to provide sufficient and accurate anatomical information. However, the female pelvic floor is so complex that it is difficult to visualize from conventional two-dimensional (2D) anatomy images (Figure 1) [23].

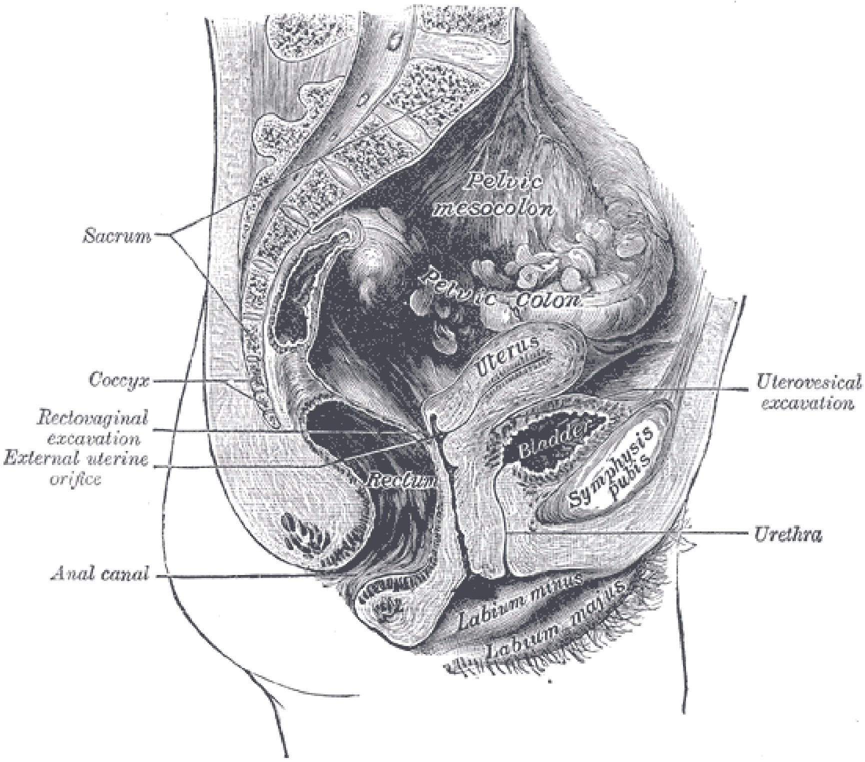

Figure 1 Sagittal Section of Female Pelvis (From Gray 1918[23])

With the development of computer technology, three-dimensional (3D) models are now available and widely used as research tools in a broad number of medical areas. Some researchers have successfully built 3D models of the female pelvic floor with commercial software such as Maya and 3D-Max Studio [24]. Compared to conventional 2D pictures, 3D models provide a more accurate representation of anatomical structures, bones, and soft tissues. 3D models also can be rotated and rendered from different angles of view, providing clinicians with more structure information. Furthermore, 3D models quantify the normal appearance of the female pelvic floor, helping scientists to understand the anatomy of the specific structures responsible for maintaining support in a better way, such as the thickness of levator ani muscle (Figure 2) [24].

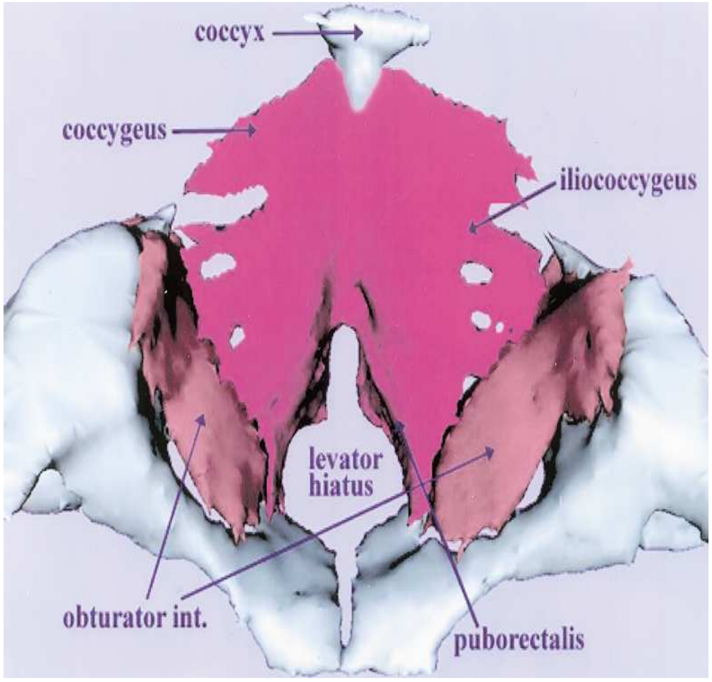

Figure 2 Coronal 3D model of female pelvis (Fielding 2000 [24])

However, even 3D models still have limitations in visualization and interaction. In most cases, 3D models are presented as 2D projections, which make it difficult for people to be fully aware of the complicated geometric structure of the female pelvic floor. 3D models only contain mesh points and mapping textures. Thus, they have to be treated as one piece. Each component in 3D models cannot be flexibly controlled and manipulated. In addition, 3D models are static models. They only can represent geometric shapes and relationship. Biomechanical properties and physiological functions of organs and tissues cannot be revealed in these models.

In 2004, Dr. Margot Damaser at the University of Illinois at Chicago proposed and built a Virtual Reality (VR) model of normal female pelvic floor based on high resolution magnetic resonance image (MRI) [25] (Figure 3). VR is an advanced computer technology used to create an artificial world and allow a user to interact with this computer-simulated environment. A user can be immersed in such a imaginary world that would normally be unavailable due to cost, safety, or perception restrictions, with the ability to navigate through the world and manipulate objects in the world [26].

Figure 3 VR model of normal female pelvic floor (Damaser 2004)

Compared to traditional 3D model, VR model has some unique features. The features are listed in the following subsections.

1.3.1 'Real' World View

The stereo view mode leads people into a 'real' world. Using certain devices such as stereo-view glasses or head-mounted displays (HMD), viewers have the impression that they are in the simulated scenes and the things they feel in VR are exactly same as those they feel in the real world (Figure 4).

Figure 4 ImmersaDesk Used to Demonstrate VR Model

1.3.2 Node Structure Model

VR model is programmed so that each component can be manipulated while visualized. VR models are usually programmed with virtual reality languages such as Virtual Reality Modeling Language (VRML) and Open Inventor (OI). In those languages, objects and scenes are created separately. Each object has its own properties in appearance and behavior. Then, all objects are connected in one world by a node structure: each object is a node and one can enable or disable its connections with other objects (nodes).

1.3.3 Integrated Model

Mechanical properties and physiological functions can be incorporated into the model, which cannot be realized completely in a traditional 3D model. For example, the elasticity of muscles and tissues, the velocity of bloods, the pressure of veins and arteries, the Young's modulus of pelvic bones can all be defined as additional properties of those objects (nodes), which make the model more realistic and accurate compared to traditional 3D models.

VR model of the female pelvic floor can be used in many clinical applications, such as surgical training, surgical planning, and augmented reality. Besides these applications, it also can be used for research and education purposes.

1.4 Problem Statement

The VR model of female pelvic floor proved to be successful and useful. However, it requires improvement in the image segmentation method. Previously, MRI scans of normal female pelvic floor were manually segmented to build VR model. In this process, an expert with the knowledge of anatomy utilizes a mouse to fill regions or label borders of target structures on the image slice. The advantage of manual segmentation is the expert's prior knowledge of a structure's anatomy utilized in the segmentation process so that despite artifacts on the image data such as diffusion and overlapping, a reasonable result can still be obtained. However, there are several disadvantages for manual segmentation.

1.4.1 Time-consuming Property

Although some available software tools can help manual segmentation such as magnetic lasso and region growing, the manual segmentation process is time-consuming and tedious, especially when there are large numbers of MRI slices or complicated shapes of structures and organs.

1.4.2 Lack of Reproducibility

Manual segmentation lacks reproducibility because of the subjectivity and limitation of segmentation tools. Different people can have different segmentation results for the same structure [27]. Sometimes it may not obtain identical segmentation results even for a same person to segment the same structure twice.

The female pelvic floor structures have complicated shapes, which make manual segmentation difficult and sometimes inaccurate. For another, due to the limitation of imaging hardware and imaging protocols, the contrast of soft tissues is low in MRI scans and the in-plane resolution is limited. Thus, the border of structures is blurred, such as for the levator ani muscle, obturator muscles, and the vagina (Figure 5). It is not easy to label the edge of targets accurately even for a trained professional.

Figure 5 Sample MRI Scan of Female Pelvic Floor

1.5 Objective of Dissertation

The objective of this dissertation is to develop a semi-automatic segmentation method to speed up the modeling process of the normal female pelvic floor as well as to increase the accuracy of VR model. Compared to the manual segmentation method, semi-automatic segmentation has the following advantages: a) Semi-automatic segmentation methods rely on computer aided digital image analysis, substantially reducing the time needed for segmentation; (b) Semi-automatic segmentation minimizes the need for intervention of human judgment and thus greatly improves both accuracy and repeatability. The proposed semi-automatic segmentation method of the female pelvic floor shall meet the following requirements.

1.5.1 Easily Extend from 2D models to 3D models

The proposed method requires to be easily extended from 2D models to 3D models. VR models can be built either from groups of 2D contours, using 2D segmentation, or from 3D mesh points, using 3D segmentation. Depending on the shape properties of the target structure, 2D segmentation method or 3D segmentation method is chosen. Thus, the proposed method can easily undergo a dimensional increase or decrease.

1.5.2 Robust

The proposed method shall be robust. There is diversity of structure shapes among different patients. In addition, imaging protocols and imaging parameters are different in MRI scans. Therefore, the proposed segmentation method needs to be robust enough to handle all these differences.

1.5.3 Smart

The proposed method shall be smart. The low contrast of the target in the image generally leads to an error in most segmentation methods. Moreover, in pelvic floor MRI scans, some structures have similar intensity value with the surrounding tissues. In manual segmentation, an expert often utilizes his or her knowledge of the anatomy of the structures while labeling the shapes. Such knowledge shall be incorporated into the proposed segmentation method so it can be smart enough to discern the correct border from image without being misled by local features.

1.5.4 Objectively Evaluate Performance

The performance of segmentation shall be objectively evaluated. Usually the evaluation of segmentation results is subjective, and the most common method is to compare the image segmentation results visually, which is a tedious and time-consuming process and lacks consistency and reproducibility. Moreover, several parameters may be involved in the segmentation process, which requires an objective comparison of different parameterizations of the segmentation method.

1.6 Overview of Dissertation

In this dissertation, a semi-automatic segmentation method is proposed which incorporates the prior knowledge of structure shapes into unsupervised segmentation process. First, a statistical model of shapes is built based on sample images in a training set. Principle component analysis (PCA) is applied to the signed distance map of the structure shapes to generate a mean shape model and a shape variation model. Then local image features are extracted from unseen data by an image-processing pipeline composed of specially designed filters. Based on the statistical model and local image features, unsupervised segmentation is performed by model matching, which can be turned into an optimization process resulting in a best-fit shape. At last, the performance of the segmentation is evaluated by a Dice coefficient function, and the Taguchi method is applied to reveal the index of significance of segmentation parameters. The proposed segmentation method is tested for 2D and 3D images, using the example of levator ani muscle and obturator muscles respectively.

The remaining chapters of the dissertation are organized as follows. Chapter II introduces the imaging modalities for the female pelvic floor and reviews the segmentation methods for medical images. Chapter III introduces the structure and pipeline of the proposed segmentation method. Chapter IV describes how to build a statistical model from training set images. Chapter V talks about extraction of local image features and model matching. Chapter VI gives the details about how to use Taguchi method to tune the segmentation parameters. Chapter VII shows test results of the 2D and 3D segmentation while Chapter VIII contains conclusion and future work, summarizing the major finding of this dissertation. Limitations of this dissertation are also discussed and a promising modification is proposed in this final chapter.

CHAPTER II

AN OVERVIEW ON MEDICAL IMAGING AND MEDICAL IMAGE SEGMENTATION

2.1 Medical Imaging Modalities

Medical imaging refers to applying different kinds of techniques and processes to create images of the human body for clinical purposes or medical science. The resulting medical images will be used to reveal, diagnose or examine disease, or study normal anatomy and physiology of the human body. Clinically, the most popular imaging methods are computed tomography (CT), ultrasound, and magnetic resonance imaging (MRI).

2.1.1 Computed Tomography (CT)

Computed tomography (CT) acts as a diagnostic tool utilizing X-ray to obtain cross-sectional imaging of the human body. Detailed images of organs, bones, and other tissues can be acquired using CT, which was first proposed by the Italian radiologist Alessandro Vallebona in the early 1900’s. Based on the principle of projective geometry, a single slice of the body on radiographic film was obtained. Specifically, the X-ray tube and film are moved synchronously in opposite directions so that points on the focal plane are sharply focused, resulting into the desired image [28]. Some substances and tissues in a human body are more permeable to X-rays than others are. Due to this difference, disparate tissues can have different intensities when the X-ray film is developed.

CT was officially introduced as clinical diagnosis equipment in 1972, and quickly became one the most important imaging methods. With the development of computer technology, CT technology has improved and now the images are created by using an array of individual small X-Ray sensors and a computer. By rotating the X-Ray equipment and sensors around the patient, data is collected from planes with multiple angles. Later on, a microcomputer processes the data to create an image on the screen.

Over the past few years, CT technology has advanced significantly. One new technique of the CT scan, called the multislice CT scan, or MSCT scan, is now widely used in coronary artery disease detection (Figure 6). Since the rotation time has been decreased to less than one second, more slices (16 ~64) can be acquired simultaneously.

MSCT with sub-second rotation times has made possible the scanning of long ranges, shorter scan times and a reduction in movement artifacts [29]. The 3D CT scan is also one of the new techniques and mainly used in angiography and brain scans. The technique involves selecting specific boundaries of the structure on the CT image. Successively narrow section images are then taken and the information from these scans is reassembled to produce a 3D grey-scale-image which may be viewed from different angles and in real-time rotation [30].

Figure 6 Multislice CT (MSCT)

CT is frequently used to detect brain diseases such as stroke, bleeding, blood clot, and brain tumor [31]. Moreover, it is widely used for detecting both acute and chronic changes in the lung parenchyma [32]. MSCT is also widely used for cardiac and cardiovascular imaging [33]. CT is not expensive compared to other imaging methods. Moreover, it is less sensitive to patient movement, which could cause motion artifacts. The main concern about CT imaging is how to reduce the radiation dose for CT examinations without affecting the image quality. A high radiation dose results in a high-quality scan since the contrast of the objects is higher. On the contrary, a lower dose leads to more image noise and results in low contrast images. However, as the radiation dose increases, so does the associated risk of radiation-induced cancer. It is estimated that a radiation exposure of 1200 millirem can induce a potential radiation-induced cancer chance around a million to one [34]. Although a great deal of effort has been undertaken to minimize the radiation dose during the scan, given the increasing number of CT scans being obtained, the increasing exposure to radiation in the population may still be a public health issue. For example, radiation doses with MSCT scans are 30 - 50 times higher than those associated with a chest x-ray [29].

2.1.2 Ultrasound

Ultrasound imaging, sometimes also called sonography, involves using high-frequency sound waves to travel through a part of body to produce images of the inside structures. Humans are capable of hearing sound with frequencies range from 20 to 20,000 cycles per second (20-20,000 Hertz or Hz), and any frequency greater than that range is called ultrasound.

Ultrasound is a soft-tissue modality, since it cannot provide useful image of bones or bodies of gas such as found in the lung and bowel. Compared to CT and X-ray, ultrasound has some unique features.

2.1.2.1 None Ionizing Radiation

Ultrasound does not utilize ionizing radiation. Instead, an ultrasound signal is sent out by a transmitter. The ultrasound signal passes through the body, partly reflected from two tissues interfaces with different acoustic impedance. The reflected signal is detected by the transducer, processed by computer and then is converted to an image on a screen: the stronger the reflected signal, the higher intensity of the image.

2.1.2.2 Real-time Image

Ultrasound imaging can create real-time images. A real-time image is still a 2D view while keeping constantly updated. The structures within a 2D image can be better demonstrated by visualizing the changes that occur within that image over time. Real-time sonography is very useful to visualize moving objects, such as a fetal heart. Also the texture and shape of the target structure can be enhanced in the image by sweeping the transducer beam through the object, providing more details to the operator [35].

2.1.2.3 Quantitative Measurement

Ultrasound imaging provides quantitative measurement and imaging of the blood flow. With the Doppler, a special form of ultrasound, both the speed and direction of flowing blood can be measured and illustrated in color pictures (Figure 7).

Figure 7 Doppler Ultrasound

Doctors utilize Doppler technique to evaluate blood flow through the major arteries and veins of the human body. A transcranial Doppler ultrasound (TCD) can be used to reveal blocked or reduced blood flow in the major arteries that could result in a stroke potentially. Also it can show blood clots in leg veins that could break loose and block blood flow to the lungs [36].

2.1.3 Magnetic Resonance Imaging (MRI)

Magnetic resonance imaging (MRI) is a noninvasive medical imaging technique, which is widely used in radiology to visualize internal structures and functions of the human body.

MRI obtains image slices of inside structures of the body based on the interaction among radio frequency pulses, magnetic fields, and body tissue [31]. The measured targets are mobile hydrogen nuclei, which are the majority of elements in the body [37].

Hydrogen nuclei are capable of absorbing energy if exposed to short wave radio pulses at their resonance frequency. After the absorption of this energy, the nuclei release this energy so that they return to their initial state of equilibrium. The transmission of energy by the nuclei as they return to their initial state is what is observed as the MRI signal [38]. The resulting image primarily reflects the water protons in the patient, as well as their chemical association with proteins, etc.

The main components of the MRI scanner are its magnet and radio frequency systems (Figure 8) [31]. The magnet system is the largest, as well as the most expensive component of the scanner and usually consists of a permanent magnet and a resistive electromagnet or superconducting electromagnet [31]. Even though the superconducting electromagnet is the most expensive magnet, it is actually the most commonly used type because of its outstanding performance. The strength of the magnet is measured in Tesla (T). Clinical magnets generally have a magnetic field strength in the range 0.1—3.0 T [39]. Magnetic field strength plays an important role in determining image quality. Higher magnetic fields increase the signal-to-noise (S/N) ratio, and allow for higher resolution and faster scanning. However, higher field strengths generally are associated with more expensive magnets and higher maintenance costs [40].

Figure 8 MRI Scanner

The radio frequency system consists of two parts: transmission system and receiver system. The radio frequency transmission system consists of a radio frequency generator, a power amplifier, and a transmitting coil. The power of the transmitter is variable, but a peak output power of up to 35 kW and a consistent average power of 1kW are generally required for high-end whole-body scanners [38]. The radio frequency receiver consists of the coil, pre-amplifier and signal processing system. Sometimes if a small region of the body is scanned, a better quality image can be achieved by using a close-fitting coil. Different kinds of coils are available for clinical diagnosis. External coils can fit flexibly around part regions of the body, such as the head, neck, knee, wrist, and breast, while the internal coil is put inside the structure of the body, such as the rectum.

2.2 Introduction of Medical Image Segmentation

Segmentation is the first as well as the most important step in building the proposed VR model since only accurate segmentation makes a reasonable and reliable anatomic model. The goal of segmentation is separation of structures of interest from background and each other based on one or more of several properties, such as texture, color, distribution of the densities of the image elements, and motion field, etc. The result of segmentation is either an image with labeled regions or a set of contours describing the region's boundaries. As for medical images, the purpose of segmentation is usually to extract known anatomic structures from images such as the heart, the brain, the knee, the spine and the liver, or to label abnormalities in tissues or organs such as tumors and cysts [41] .

Segmentation allows the quantitative measurements of structures and thus can assist doctors in confirming the existence of certain diseases and evaluating their severity. In addition, segmentation results can be used to build an anatomical atlas, which is valuable for pre-surgical planning. Furthermore, dynamic or adaptive segmentation can track anatomical changes over time, making it very useful in image-guided surgery. The most general applications of medical image segmentation are described in the following sections.

2.2.1 Visualization

Based on segmentation results such as contour and labeled pixels or voxels, we can create surface models, which give a 3D view from any angle. The surfaces of models can be generated from different kinds of mesh elements such as hexahedral mesh, tetrahedral mesh, pyramid mesh, or prism mesh. The smaller mesh elements, the smoother the surface. Different textures are then mapped to the surface. Directions, intensities, and the color of the lighting source also need to be defined to make the model look more realistic (Figure 9).

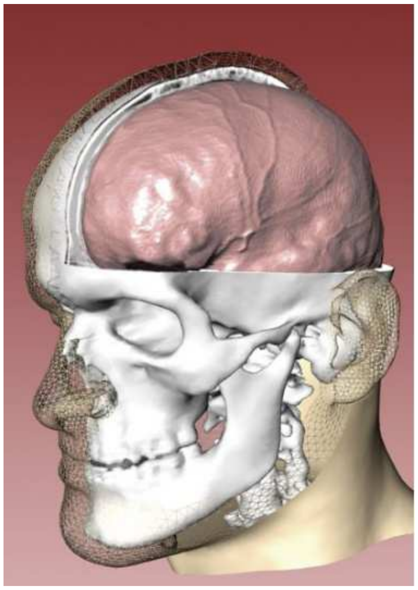

Figure 9 Reconstruction of Head Anatomy

2.2.2 Quantitative Measurement

Quantitative measurements of structures and organs in medical images are often used in medical studies, and accurate measurements can only be acquired by proper segmentation. Usually the quantitative measurements are focused on geometric properties of the structure such as position, length, angle, thickness, surface area, and volume. For example, in the study of women with unilateral defects in the public portion of the levator ani muscle, the cross-sectional areas of the muscles are usually smaller than normal ones. Segmentation of the levator ani muscle followed by a quantitative measurement of the cross-sectional area is the usual way to evaluate the degree of muscle loss [42].

2.2.3 Pre-surgical Planning and Image-guided Surgery

Segmentation is a significant part in pre-surgical planning and image-guided surgery. For example, in order to remove tumors from organs such as brain or liver, surgeons need to operate carefully to avoid anatomical hazards such as arteries or functional areas (Figure 10). Before the operation, patients will have MRI or CT scans. Based on the segmentation of those scans, safe surgical trajectories can be accurately designed. During the procedure, a fast scanning technique such as ultrasound can generate real-time images of the operation area, and the simultaneous segmentation results will help the surgeon to confirm that the pre-planned operation path is being followed.

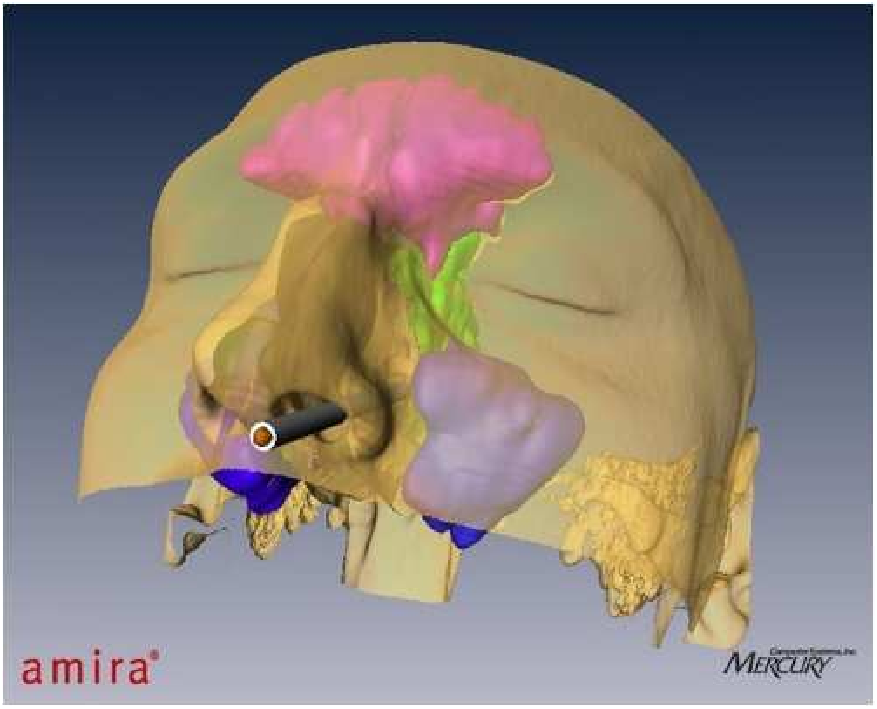

Figure 10 Paranasal Cavities

2.2.4 Detection of Change

Segmentation is widely used to analyze dynamic images such as Functional MRI (FMRI). FMRI is a relatively new neuroimaging technique, which allows measurements of the hemodynamic response related to neural activity in the brain or spinal cord. During the imaging, MRI scans are acquired over time, and the change of activities in certain brain areas, which could be related to some movements of the body, can be detected by tracking the change of segmentation results from fixed spots (Figure 11).

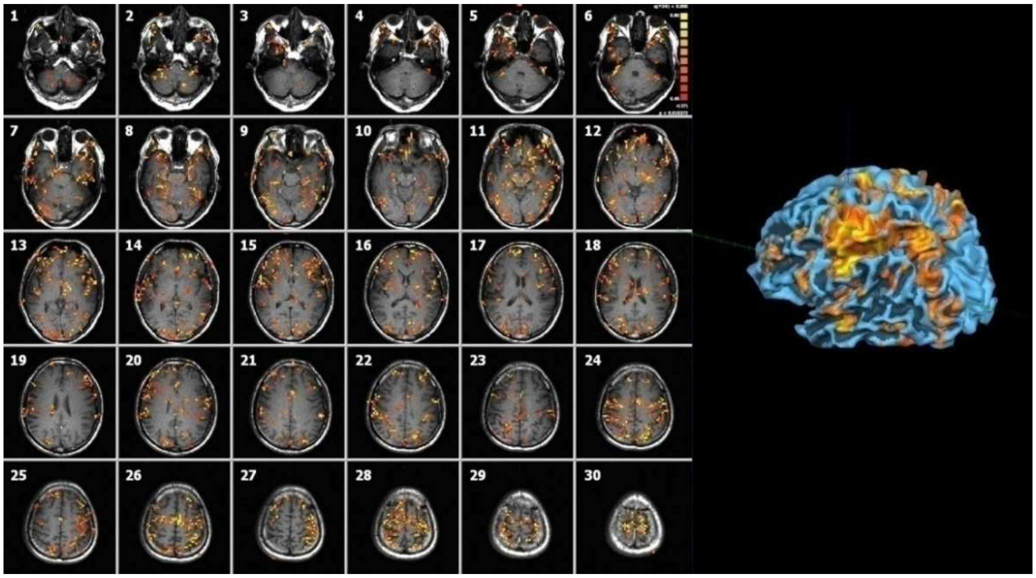

Figure 11 FMRI Segmentation of Human Brain

2.3 Image Segmentation Techniques

The input for a segmentation pipeline is grayscale digital images, such as the imaging results from MRI or CT scans. These images can be stored in either a 2D-file or a 3D-file format. Most of existing segmentation algorithms are developed for 2D images although some of them can be extended to 3D.

There is a large variety of techniques available for segmenting images. They can be divided into two categories: model-free segmentation methods and model-based segmentation methods. Model-free segmentation methods are based on local features as well as properties of the image itself and no prior knowledge is required. On the contrary, model-based methods use a training set to build a 'Golden Model', fit this model to unseen data, and then the best fit shape is determined as the results of segmentation.

2.3.1 Model-free Segmentation Techniques

Model-free segmentation methods, sometimes called unsupervised segmentation methods, are based on local image properties such as intensity value, gradient magnitude, and textures. Image statistics tools such as histogram, mean, variance, and entropy can be used in this kind of segmentation. The following methods are the most frequently used model-free techniques.

2.3.1.1 Thresholding

Thresholding is one of the most widely used segmentation techniques for digital images. It separates the structures of interest based on signal intensity of these digital images. The thresholding operation can change the pixel values or categorize pixels into different groups based on one or more specified values, i.e. threshold values. There are two basic types of thresholding methods: binary thresholding and general thresholding. When the binary thresholding method is applied, a grayscale image can be transformed into a binary image by changing the pixels' values according to the rules described in Figure 13(a). If the intensive value of a pixel is less than the upper threshold and greater than the lower, the output of this pixel (i.e. inside value) is defined as 1 (white), Otherwise, the output (i.e. outside value) is defined as 0 (black) (Figure 13(b)). The generated binary images are usually taken as inputs for further morphological image processing such as opening, closing, eroding, and dilation.

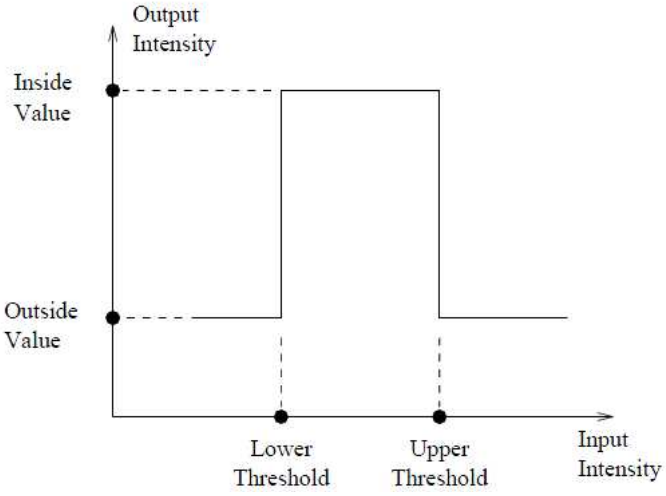

(a) Binary Thresholding Function

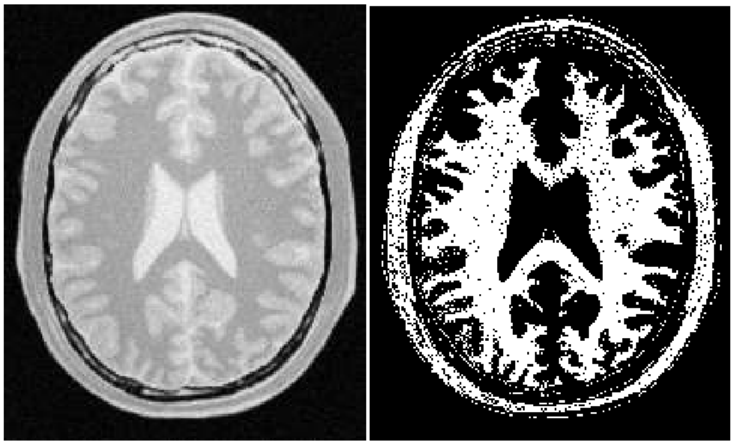

(b) Binary Thresholding for Brain Image

Figure 12 Binary Thresholding

As for general thresholding, pixel intensities can be transformed with flexibility. One can define a threshold value, and any pixel with intensity value below or above this threshold will be replaced by a predefined value while all other pixels remain unchanged. Alternatively, one can define a lower threshold value as well as an upper threshold value, and all pixels with intensity value within the threshold range will be replaced by a predefined value while all other pixels remain unchanged. The output of general thresholding is an image with a highlighted region of certain intensity, thus separating the structure of interest from the background.

There are some other thresholding techniques used in medical image segmentation including multi-thresholding and adaptive thresholding. Through multi-thresholding, the number of significant intensity levels can be found, and an optimum value between any two consecutive significant intensity levels can be selected to segment the images [43].

Different from multi-thresholding, adaptive thresholding is a technique to change the threshold dynamically over the image. With different threshold based on difference in the pixels, this method can deal with changing lighting conditions in the image, e.g. those occurring due to a strong illumination gradient or shadows [44]. The Thresholding method has already been used in CT images to segment bones and soft tissues from background [45]. It also has been used in brain MRI images to segment brain tissues [46]. The key to effective thresholding is to choose a proper threshold value. The thresholding segmentation method is simple and fast. However, it is sensitive to noise in low contrast images and usually generates isolated pixels instead of connected regions.

2.3.1.2 Edge Detection

Edge detection method extracts discontinuities in the digital image and the results can be used for segmentation. It is because the pixels on the border of structure often have much higher or lower intensity values than those of neighboring pixels. Many operators can be used to extract edges, and most commonly used is the Canny operator in image segmentation since it can give continuous border/contour of objects [47]. Canny edge detection consists of four steps:

1) Noise Reduction

Edge detectors are susceptible to noise so Canny detectors smooth the raw image by using a filter based on the first derivative of a Gaussian.

2) Edge Magnitude and Orientation Computation

A structure's edge may have a variety of directions, so the Canny algorithm uses four filters to detect horizontal, vertical, and diagonal edges and calculate the gradient magnitude.

3) Directional Non-maximal Suppression

In this step, a search is carried out to determine if gradient magnitude achieves a local maximum in the gradient direction.

4) Hysteresis Edge Labeling

There is one high threshold value which is used for marking the border/contour of high confidence, and another low threshold value will be used to track faint sections (Figure 13) [48].

Although the Canny edge detector is a powerful tool for 2D image segmentation, it cannot be directly applied to 3D volume images[49].

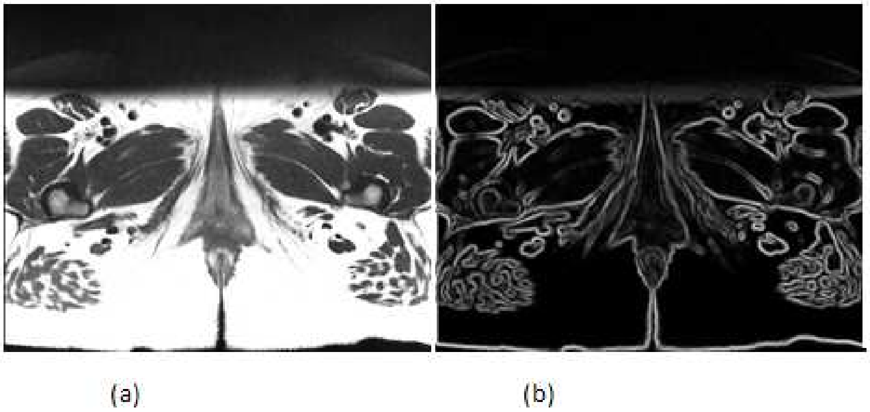
(a) (b)

Figure 13 Canny Edge Detection for Pelvic Floor MR Image

2.3.1.3 Clustering

Clustering means classifying objects into different groups according to certain properties, such as intensity, color, texture, and connectivity. Segmentation is used to determine to which data group a pixel or voxel naturally belongs. The most popular and simple technique is K-means clustering which usually consists of four steps:

1) K cluster centers are chosen randomly.

2) Each pixel in the image is assigned to the cluster to minimize the squared or absolute difference between the pixel and the cluster center.

3) The cluster centers are recalculated by averaging all of the pixels in the cluster.

4) Repeat the above step 2) and 3) until certain termination criteria are met.

The most common termination criterion is that there is no change in cluster membership compared to the previous iteration [50]. Although convergence is guaranteed with this algorithm, the optimal solution may be not achieved. Some other clustering methods are developed based on the method of K-means. Some of them have achieved great improvement of image segmentation. These methods include fuzzy C-means, which gives the possibility of certain pixels belonging to each cluster. By setting the threshold value of the possibility, each cluster can contain greater or fewer pixels [51]. In addition, all clustering algorithms can easily be extended from 2D to 3D.

2.3.1.4 Region Growing

Region growing algorithms have lot of applications in medical image segmentation. Region growing method has proved to be a very effective approach. The purpose of region growing is to produce spatially connected regions based on intensity homogeneity as well as geometrical proximity. A simple approach of region growing segmentation is to start with a seed region (user-defined pixels) that is confidently considered to be inside the target object. The pixels in the neighboring region are evaluated to determine if they belong to the object based on certain criteria (Figure 14). This process will continue and repeat until a certain stop condition is satisfied [52].

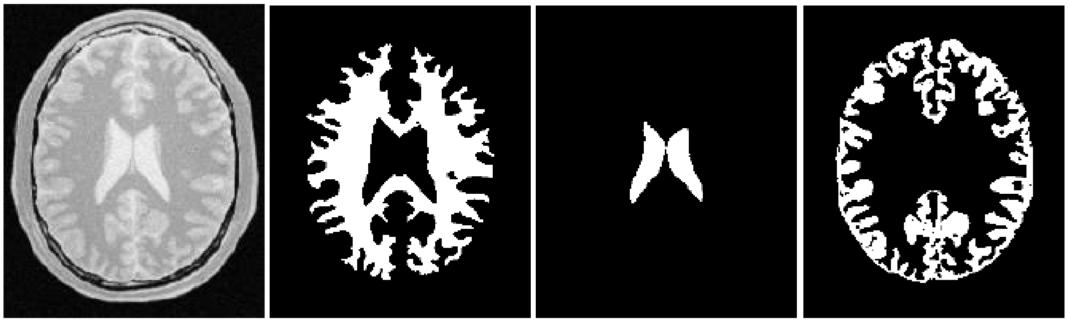

Figure 14 Segmentation of Brain MRI by Using Region Growing Method

The performance of region growing segmentation is largely based on merging and termination criteria. The simplest merging criterion is to evaluate an intensity value to determine if it is inside a specific interval.

Another criterion for merging pixels is to minimize the error of misclassification. The objective is to find a threshold that classifies the image into two clusters. Therefore, the area under the histogram for one cluster, locating on the other cluster's side of the threshold, can be minimized. The region growing method can easily be extended from 2D to 3D applications in medical image segmentation [53]. The advantage of region growing methods is their simplicity. The major disadvantage is that they are based on point wise comparisons, which can give jagged borders.

2.3.2 Model-based Segmentation Techniques

Model-based segmentation means that a model representing an object is obtained through a training set and is matched to unknown image data later. During the matching process, the model's shape and additional properties are varied to improve the match iteratively. Some typical model-based segmentation techniques are discussed in following subsections.

2.3.2.1 Golden Images

The simplest model-based method is to use a typical example of an object as a 'Golden Image'. In order to register the golden image to new data, a correlation operation is performed. Once the golden image is created, the registration will search for the proximate position of the structure in a new image. This method can be used in those applications that the objects of interest have fixed shape and size. The good thing for this method is quality examination of standard industrial products. However, in the application of segmentation of medical images, most structures and organs of human body have variability in both shape, size and texture, thus limiting the precision of this method [54].

2.3.2.2 Deformable Templates

Deformable templates give a simple and compact representation of similar objects with variations in shape. Because the objects found in the same family can be deformed to each other, an ideal template can be created. Depending on the intrinsic properties of the objects, a template can be created by a polygonal boundary model or a triangulation model. The deformation of the template is constricted by defining the range of angle and ratio of length. When matching the template to a new image, the transformation parameters will be iteratively updated to change the template shape. By this means, the objective function is minimized and the best match between the deformed template and the edges in the image is achieved [55]. The method can be effective in certain cases but it is also complicated. The performance of the segmentation is mainly based on how a template is built; however, there is no general method to build templates or to choose the nodes for the polygonal boundary model. Determining how to represent the shape by triangles is based on observation and experience.

2.3.2.3 Active Contours

Active contours, known as snakes (also called an active surface in 3D segmentation), was a method first introduced in 1987 and has been used more and more frequently in medical image segmentation [56]. An active contour is a flexible spine, which detects specified properties of an image and can dynamically fit to the edges of a structure by minimizing an energy function. Initially, it is placed close to an object's gradient [56]. The forces that control the curve/surface regularity are called 'internal forces'. In other words, the curve/surface is given the physical properties of elasticity and rigidity, which guarantee that curve/surface is always smooth while attracting to the boundary of objects (Figure 15). Successful applications have been reported on segmentation of the brain [57], bones [58], and lung [59] . The active contour or surface method has limitations in the following areas:

1) The method depends on the initial positions of the contour or surface, which need to be carefully placed by the user.

2) The method depends on the quality of images. It is prone to give an error result when it is applied to a low contrast image: it either includes different structures in one contour, or misses a part of structure.

3) The method is complicated and requires a lot of computation during iterations.

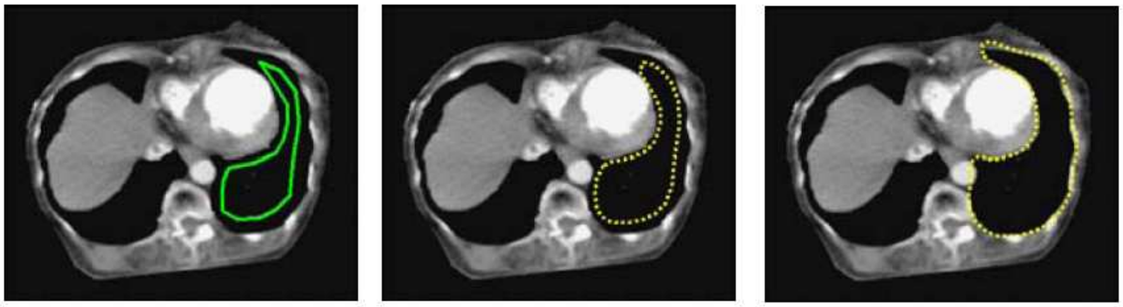

Figure 15 Segmentation of MRI by Using Active Contour Method

2.3.2.4 Deformable Fourier Models

Usually, deformable curves and shapes can be expressed as the parameterizing functions. Staib and Duncan represent the shapes of objects in medical images using Fourier descriptors of closed curves/surface [60]. For example, a closed curve can be expressed as:

$$\bar{x}(s) = \begin{bmatrix} x(s) \\ y(s) \end{bmatrix} = \begin{bmatrix} a_0 \\ b_0 \end{bmatrix} + \sum_{k=1}^{\infty} \begin{bmatrix} a_k & b_k \\ c_k & d_k \end{bmatrix} \begin{bmatrix} \cos 2\pi ks \\ \sin 2\pi ks \end{bmatrix} \tag{1}$$

Where a_0, c_0, a_1, b_1, c_1, d_1, …. are called Fourier coefficients and can be computed by the following equations:

$$a_0 = \frac{1}{2\pi} \int_0^1 X(S) ds \tag{2}$$

$$a_k = \frac{1}{2\pi} \int_0^1 X(S) \cos 2\pi ksds \tag{3}$$

$$b_k = \frac{1}{2\pi}\int_0^1 X(S)\sin 2\pi k s ds \tag{4}$$

$$c_0 = \frac{1}{2\pi}\int_0^1 Y(S) ds \tag{5}$$

$$c_k = \frac{1}{2\pi}\int_0^1 Y(S)\cos 2\pi k s ds \tag{6}$$

$$d_k = \frac{1}{2\pi}\int_0^1 Y(S)\sin 2\pi k s ds \tag{7}$$

The choice of coefficients affects the curve complexity. By truncating the Fourier series, a compact representation of a smooth curve can be obtained, where a_0 and b_0 define the translation of the curve and the rest follows the parametric form of an ellipse. By placing limits on each coefficient, the shape can be constrained to some degree but not in a systematic way. The method of deformable Fourier models is somewhat similar to the statistical models described below, but is not as general. For instance, it has difficulty to represents open boundaries [61].

2.3.2.5 Finite Element Models

Finite element models (FEM) can be applied to model variable image objects as physical entities with properties of internal stiffness and elasticity [62]. Pentland used three dimensional models which act like lumps of elastic clay [63]. They drive modes of vibration of suitable base shape, such as an ellipsoid, and build up shapes from different modes of vibration. They can fit models to range data by an interactive process, and can compare different heads by comparing the parameters. Models built by FEM are relatively easy to construct and represent a compact parametric shapes family [64].

2.3.2.6 Statistical Models

Statistical analysis is used to describe important properties of large data with a small set of meaningful values. Recently, lot of research has been done to determine the use of statistical models for medical image segmentation [65]. Statistical models retrieve shape information from a set of labeled training data. The most widely used statistical model is the active shape model (ASM), proposed by T. F. Cootes in 1995 [66]. Each shape in the training set is described by a set of corresponding points called landmarks. These sets of landmarks are rotated, scaled, and aligned to get a mean shape with variable point positions. Thus, the shapes can be represented by a point distribution model (PDM). Principle component analysis (PCA) is then applied to reduce the dimension of the PDM and eigenvectors with the biggest eigenvalues represent the greatest variation in shape. In order to segment the new data, the model needs to be rotated, scaled and positioned again and the shape variation parameters need to be adjusted to get a best fit. ASM has achieved great success in medical image segmentation of organs such as brain [67], bones [68]], heart [69], lung and kidney [70], and also has been widely used in face recognition [71].

A direct extension of the ASM approach leads to the active appearance models (AAM) [72]. Beside the shape information, the textual information is also included in the model. The statistical shape model and statistical texture are built separately in a similar way and then combined together using a weight vector. Compared to ASM, AAM is more powerful, especially for those objects with complex texture information; however, since the model contains both shape variation parameters and texture variation parameters, model searching (fitting) will take more time than ASM [72].

2.4 Conclusion

Model free segmentation methods are based on local image features and properties. The advantage of these methods is that no training process is needed and one can quickly apply them to segment data. However, the disadvantage is that the segmentation is based on the quality of the image and can be easily misled by noise in the image. Thus, this method is mostly applied to high quality images, in which the target objects have high contrast and are easily identified. Although model-free methods are generally low-level segmentation methods, they could be used during the process of a high-level segmentation pipeline, or as preprocessing filters.

An advantage of model-based segmentation methods is that the strong statistical background makes them very robust even if the quality of the analyzed data is poor. The prior information about an object’s appearance helps to compensate for missing texture information. However, some disadvantages do exist: the training process is long, and optimization takes a lot of time and is not suitable for modeling objects which can only be identified in a special context or which do not have a fixed shape, e.g. matching clouds, stones, trees, or blood vessels.

As a conclusion, in segmentation of medical images, no one method is good for all applications but adequate segmentation could be obtained by using a variety of segmentation methods. What kind of segmentation methods should be applied depends on the following considerations.

2.4.1 Imaging Modalities and Image Quality

Since quality of image is different due to different imaging modalities (CT, MRI or ultrasound) and even for the same modality, different imaging protocols or imaging parameters can cause differences in the resulting images. Images with high contrast of the target structure can use model-free segmentation methods with the benefits of fast and easy implementation, while segmentation of low contrast images should consider model-based methods for a robust and reliable segmentation.

2.4.2 Properties of the Structures in Images

Some structures such as muscle and soft tissue have low contrast in images, while some structures such as bone and bladder have higher contrast. Moreover, textures and shapes are varied, even for the same kind of structures [73]. Model-free methods are sensitive to intensity value while model-based methods are sensitive to shape variations.

2.4.3 Requirements of Application

Segmentation can be used for varieties of applications such as to identify pathological organs, have quantitative measurements, and perform image registration and modeling. Different applications have different requirements and criteria for segmentation. Accuracy and efficiency are important for all applications; however, no golden method is available to meet both, and most algorithms require a tradeoff between accuracy and efficiency to meet the specific requirements of the application.

CHAPTER III

PROPOSED SEMI-AUTOMATIC SEGMENTATION METHOD

3.1 Challenges for Semi-automatic Segmentation of Medical Images

Recently, many researchers have put great efforts into developing algorithms for semi-automatic segmentation of medical images ([74],[75],[76]). However, there are several challenges remaining for such algorithms.

3.1.1 Diffuse in Intensity Value

In medical images, structures and organs are often diffuse in intensity and lack strong edges. Currently, most of the semi-automatic segmentation methods are either based on the intensity value used to label the region of objects, or based on a gradient value to delineate the edge of objects [77]. Those semi-automatic segmentation methods can achieve satisfying results where good quality and high contrast images can be acquired [78]. However, for segmentation of medical images, those methods generally do not give satisfying results [41].

3.1.2 Limited In-plan Resolution

In medical images, in-plane resolution is limited because of hardware restrictions and the imaging method itself. MRI can acquire higher resolution images than CT or ultrasound, but it also has to be limited in certain ranges [79]. Since higher resolution leads to smaller voxel volume, the received signal intensity is decreased, as is the signal-to-noise (S/N) ratio. With limitations on in-plane resolution, small structures such as the vagina and urethra in MR images of the female pelvic floor are not easily separated from background [80]. Furthermore, lower resolution means fewer pixels or voxels are contained in the shape of structures, thus small structures cannot give smooth borders with intensity-based segmentation methods [80].

3.1.3 Difficult to Separate Objects

In medical images, many structures and organs have similar intensity values, creating a challenge for segmentation methods to separate objects from each other automatically, based only on local image features such as intensity and gradient value [81]. Typically, this effect cannot be removed by simple pre-processing techniques such as histogram equalization [82].

3.2 Model-Based Semi-automatic Segmentation

In order to solve the challenges mentioned above, model-based methods have been introduced into semi-automatic segmentation [83]. Model-based segmentation methods are based on local image features and on prior knowledge of anatomy to identity structures and organs in medical images[84]. There are several model-based methods that can be used in semi-automatic segmentation such as deformable templates, active contours, Fourier models and FEM, but the utmost used is statistical model methods [85]. A statistical model not only represents an object of interest, but also describes how its shape might deform based on a statistical analysis of shapes of same class of objects. Compared to other segmentation methods, statistical models have the following advantages [86].

3.2.1 Robust

Strong statistical background in general makes the models very robust even if the quality of image data is not good. Usually, the statistical models describe the shape variation of an object using mean shape models and shape variation models that are generated based on analysis of shapes of objects in the training set [87]. With combinations of the two models, a new instance of shape for this object can be created to fit into unseen image data [88]. This process is not only based on local image properties, but also based on the two shape models mentioned above.

3.2.2 Statistical Analysis to Provide Prior Knowledge

The prior information about an object's appearance helps to compensate missing information. Sometimes, part of a border of structure is missing in an image because of diffusion or noise or artifacts. For manual segmentation, a trained professional can make a reasonable guess of the missing part based on his or her knowledge of anatomy of the structure as well as the available information of the structure in the image [89]. Statistical shape models perform in a similar way, but the knowledge of anatomy of the structure comes from the statistical analysis of structure shapes in training set [87]. However, statistical shape models also have some limitations.

3.2.2.1 Labor Intensive

The training process is labor intensive. Sample images of structures for the training set need to be carefully examined to ensure they can cover most shape variations [88]. Images in the training set also need to be manually segmented by professionals to generate a reliable shape model [88]. At last, the segmentation results need to be normalized before performing a statistical analysis.

3.2.2.2 Time-consuming

The fitting process could take a long time because of multiple control parameters [88]. Model fitting means variation of shape based on the local image features as well as statistical shape models. Many control parameters are involved in this process such as location, scales, rotation angles, moving speed, and weightings. Some complicated statistical shape models can have even more control parameters.

3.2.2.3 Limitation of Statistical Analysis

Statistical shape models are not suitable for modeling objects that do not have fixed shapes, but they do allow variation of shapes to a certain degree [65]. However, for objects with large shape variation, reliable shape models cannot be obtained from statistical analysis. For example, the shape of the bladder can vary a lot due to filling and emptying status [90]. Therefore, it is not suitable to use statistical model for semi-automatic segmentation of the bladder.

3.3 Limitation of Landmark-Based Statistical Model

The most frequently used statistical model for medical image segmentation is the Active Shape Model (ASM), proposed by T.F.Cootes in 1995 [66], which was briefly introduced in Chapter II, section 2.3.2.6. In his statistical model, each shape in the training set is described by a set of corresponding points called landmarks (Figure 16) [71]. There are three types of landmark points. Type 1): Application-dependent points, such as the center of an eye or corners of mouth in the face model; type 2): Application-independent points, the highest point, lowest point or curvature extreme in the model; type 3): Other points, which can be interpolated from the above-mentioned points.

Those set of landmarks are rotated, scaled, and aligned to get a mean shape with variable point positions. Thus, the shapes can be represented by a point distribution model (PDM). PCA is then applied to reduce the dimension of the PDM, and eigenvectors with the biggest eigenvalues represent the greatest variation in shape.

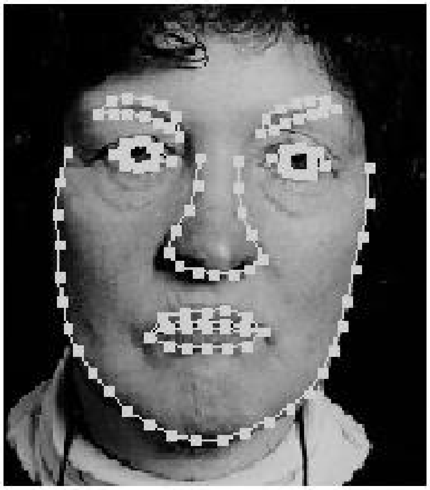

Figure 16 Landmarks of Face (T F Cootes 1998)

Although ASM has achieved great success in face recognition [71], the model has some limitations when applied to medical image segmentation:

1) Manually labeling each corresponding point in images is time-consuming and labor intensive, and sometimes it is impossible for people to identify all the correspondent points of the structures visually.

2) Performance of the model is based on the proper selection of application-dependant landmarks, and this process is subjective and has no standards. It is mostly based on observation and experience.

3) Normalization of landmarks model is computationally intensive. To compare the equivalent landmark points of different samples, they must be aligned with respect to a set of axes by rotating, scaling, and translating operations. In Cootes' algorithm, each landmark point needs to be weighted and must solve a large equation set to get global minimization for the weight matrix [66].

4) It is difficult to extend the method from 2D to 3D images. The reason is obvious: to identify and label each corresponding point in 3D images is much more difficult than in 2D images, and sometimes it is highly impractical.

3.4 Overview of Proposed Semi-automatic Segmentation Method

In this dissertation, a semi-automatic segmentation method is proposed, which can be applied on both 2D and 3D MR images of the female pelvic floor. The proposed segmentation method is a statistical model-based method and contains the following features.

3.4.1 Using Distance Field Instead of Landmarks

Instead of using landmarks, the proposed semi-automatic segmentation method is based on a statistical model of a distance field. The distance field is an operator normally applied to binary images, which contain only black and white pixels. It is a representation of a digital image by assigning to each pixel the distance to the nearest non-zero pixel [91]. The distance field was first introduced by Pfaltz and Rosenfeld [92], and has been used in various applications, such as blurring, path finding, motion planning in robotics, pattern matching and so on [93]. It can also be used in pattern recognition to classify certain objects in an image by defining a threshold [93] . Compared to the statistical models based on landmarks, the distance field has the following advantages.

1) It does not require manual labeling of corresponding landmark points slice by slice. Instead, the distance field is automatically generated from a series of binary mask images, which separate target structures from the background of MRI images [93]. As a result, it can greatly decrease the time to build a statistical model.

2) It is a more robust and reliable statistical model. Since the distance field covers all the pixels inside and outside of the target structure, it can capture all possible anatomical features of the shape of the structure [94]. The calculation of the distance field map is automatic and unsupervised, thus the statistical model is more objective and reliable.

3) It is easy to extend the method from 2D to 3D images since calculation of the distance field is based on vectors and matrix operations.

4) The distance value can be directly used for updating contour or surface movement in model searching since it represents the closest path from the current position to the border of target structures.

3.4.2 Using Centered Affine Transform to Align Shape model

Similar to the ASM/AAM method, the corresponding points in distance field images, which are generated from images in the training set, need be well aligned with respect to a set of axes before performing the statistical analysis. However, instead of using a weight matrix for each pixel and solving a large set of equations to obtain alignment parameters, the proposed segmentation method applies a centered affine transform between each of two distance field images [95]. To reduce the effect of the randomly selected initial shape, this procedure will be iterated several times. During the process, a pair of 2D or 3D distance field images are converted into vectors and a centered affine transform between these two vectors is composed of linear transformations (rotation, scaling) and a translation (shift).

3.4.3 Extraction of Local Image Features by Designed Filter Sequence

A specially designed image filter sequence is applied to an unseen image to extract the local image features, including windowing, smoothing/noise reducing, contrast enhancement, and feature extraction.

3.4.3.1 Windowing Filter

Medical image data are usually 12 to 16 bits, while the grayscale display of the computer provides only 8 bits (256 levels). Thus a windowing filter is required to select a certain rang of intensity values for display. For this filter, windowing parameters need to be carefully chosen since inappropriate windowing display can ruin contrast information and some features of target structure can be missing.

3.4.3.2 Smoothing/Noise Reducing Filter

In general, the noise signal has higher frequency than a normal signal in medical images. Consequently, a low pass filter can be used to remove or reduce noise [96]. However, small features of the structure may also be smoothed out by applying a low pass filter. In order to keep the features of the edge of structures, an anisotropic diffusion filter is the pipeline.

3.4.3.3 Edge Enhancement Filter

The statistical model is based on the shape information of the structures, i.e., the boundaries of objects in images. Proper features can be extracted from the image with an edge enhancement operation [97]. Moreover, during the model fitting process, edge properties of the structure are the most important local image features that affect the performance and result of segmentation.

3.4.4 Using Evolutionary Strategy for Model Matching

Given the statistical model and image features of unseen data, the model-based segmentation is to first superimpose the model over a given image and then change the model parameters until the model is as close to the target image as possible [85]. In this dissertation, an Evolutionary Strategy (ES) is applied to update the evolutionary contour or surface in the parameter space to obtain the optimal value.

3.4.5 Using Taguchi Analysis to Improve the Performance of Segmentation

To evaluate the performance of the proposed segmentation method, the results of the semi-automatic segmentation will be compared with those of manual segmentation. A similarity value will be calculated using the Dice coefficient equation [98]. Then Taguchi analysis will be performed based on the Dice coefficient to tune the control parameters of segmentation to improve performance [99]. Taguchi method is a technique to lay out the experimental plan in the logical, economical, and statistical way [100]. It is usually used where the output depends on many inputs. By systematically choosing certain combinations of variables, the Taguchi method can separate their individual effects without having to tediously and uneconomically run the process using all possible combinations of values of those variables [100]. After Taguchi analysis, the significance index of segmentation parameters can be generated, and the trends of tuning parameters for better performance can be finally acquired.

The framework of the proposed segmentation method is shown in the following chart (Figure 17) to provide tuning trends for better performance.

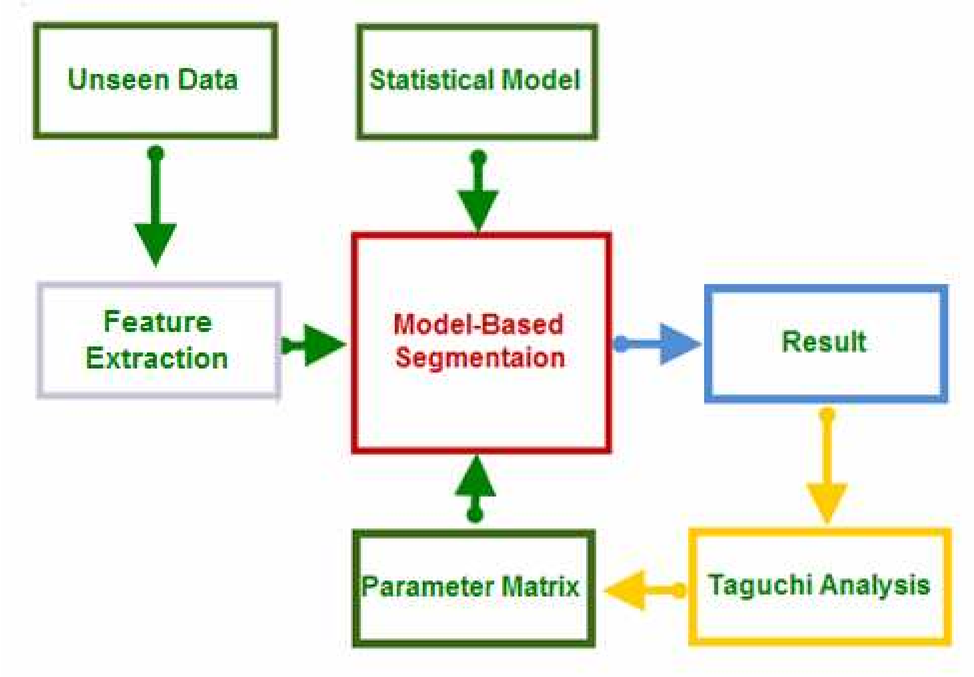

Figure 17 Framework of Proposed Segmentation Method

First, a statistical model is built based on images of the structure in the training set. Images are manually segmented and aligned, and PCA is performed to generate a mean shape model and a shape variation model, which contain the most shape variations for target structures. Then local feature map of unseen image data is obtained by a specially designed filtering sequence, including contrast enhancement, noise reduction, smoothing, and edge extraction. With the shape model and feature map, automatic segmentation is performed by matching the model to the border of structures using ES method, an optimization technique based on evolution and adaptation. At last, segmentation performance is evaluated by calculating a similarity coefficient between semi-automatic and manual segmentation results. Since several segmentation parameters are involved in segmentation, Taguchi analysis is performed to investigate the significance of segmentation parameters and provide tuning trends for better performance.

Details of how to build the statistical model will be covered in Chapter IV. The systematic approach to image feature extraction and model matching will be deliberately described in Chapter V. The performance evaluation and Taguchi analysis will be discussed in Chapter VI.

CHAPTER IV

BUILDING STATISTICAL SHAPE MODEL

4.1 Introduction

A statistical shape model is one kind of mathematical representation of prior knowledge of structure shapes [65]. It not only describes what the general shape a structure looks like but also determines how it can vary based on statistical analysis of shape features. Building a statistical shape model is the key process of the proposed semi-automatic segmentation method, and only a robust and accurate statistical model can lead to reliable segmentation results. Several steps are involved in building the statistical shape model. At first, a training set is established by choosing normal patient examples from image database. Clinically, several imaging methods can be use to get images of the female pelvic floor such as CT, MRI and ultrasound. CT has the problem of radiation and has limited application in the evaluation of the pelvis because of low contrast of soft tissues (Figure 18). Nevertheless, it may be part of abdominal scanning (e.g. for tumors), and has uses in assessing bone fractures [101].

Figure 18 CT Scan of the Female Pelvic Floor

Ultrasound can be used to evaluate lower urinary tract and pelvic floor dysfunctions. It can also be used to evaluate the dynamic response of female pelvic floor muscles as well as to identify gallstones [102]. Some researchers also use ultrasound to evaluate the anatomy of the levator ani muscle [103]. However, the signal of ultrasound is noisy, and the borders of soft tissues and muscles are not clear enough for accurate segmentation (Figure 19). An ultrasound image has low contrast, resulting in difficulty in separating one structure from surrounding tissues and organs [104]. Sometimes, the structure is blurred with the background, which makes it impossible for identification and segmentation even with post processing of images.

Figure 19 Ultrasound of Female Pelvic Floor

Compared to CT and ultrasound, MRI gives the best contrast for soft tissue, playing a main role in pelvic floor imaging applications [105]. Moreover, sensitivity for the detection of fluid and its ability to direct multi-planar imaging make MRI superior to other imaging modalities in the investigation of the anatomy of the female pelvic floor [106]. In general, MRI has the following advantages.

1) MRI does not use X-Rays or any other type of ‘ionizing’ radiation. Alternatively, powerful magnetic fields and radio frequency fields are used to acquire images, so MRI provides a safer imaging technique.

2) MRI has the ability to change the imaging plane by choosing radio frequency pulse bandwidth, which is also called ‘slice selection’. Therefore, the patient’s body does not need to be moved during the MRI scan.

3) MRI scans can provide more detailed information about soft tissue than CT and ultrasound. In addition, MRI can give clearer difference between normal and abnormal tissue than CT scan [25] (Figure 20). MRI has the ability to adjust the contrast of scans by changing the radio waves and magnetic fields, which in turn change the received signal intensity. By changing the contrast settings, different structures and tissues can be highlighted. Sometimes contrast agents are also used in MRI but it is noteworthy that they are not made of iodine [107].

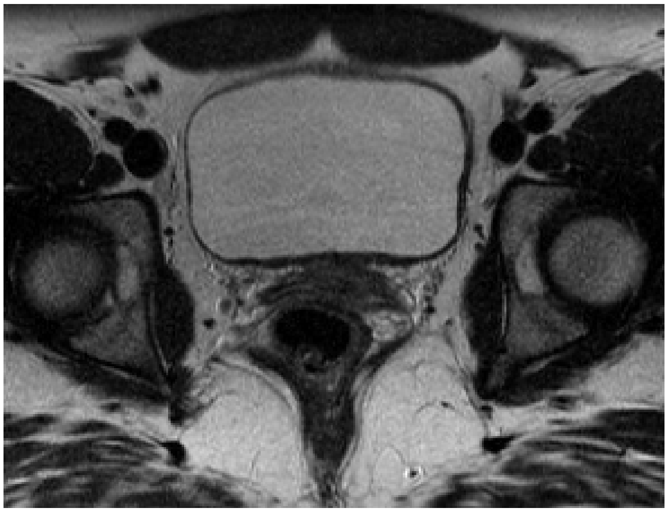

Figure 20 MRI Scan of Female Pelvic Floor

However, MRI is more expensive and slower than CT. In addition, CT is better than MRI for imaging bone structures. MRI is not applicable for some patients who have received certain types of surgical clips, metallic fragments, cardiac monitors, or pacemakers [105].

To create an accurate statistical shape model, MRI scans of normal female pelvic floor are used as training set samples since they can provide better contrast for soft tissues. All the MRI slices are examined by a trained professional (radiologist) to ensure that the target structures are normal and intact. Besides, the candidate images are confirmed to have sufficient shape variations for target structures, thus a robust shape variation model can be obtained. In the next step, these MRI scans are manually segmented by a live wire algorithm to generate binary mask images, which separate target structures from image background. The binary mask images are then cropped to obtain the region of interest (ROI) image, which only contains the shape information of target structures. Because of diversity of shapes among different patients and different imaging protocols, the binary ROI images are aligned to filter out position, rotation, and scaling information. In this way, the filtered images are normalized, and should only contain shape features of target structures. A centered affine transformation is used to align training shapes here. Distance maps are calculated based on the aligned images. A distance map can translate shape features into distance values to nearest shape point, i.e., pixel or voxel of structure edge. At last, PCA is applied to the distance map to extract the most salient features of shapes. As a result, a mean shape model, a shape variation model, and according eigenvalues are obtained and will be used for segmentation of unseen image data. The framework of building the statistical model mentioned above is shown in Figure 21, and the remaining sections describe the detailed steps.

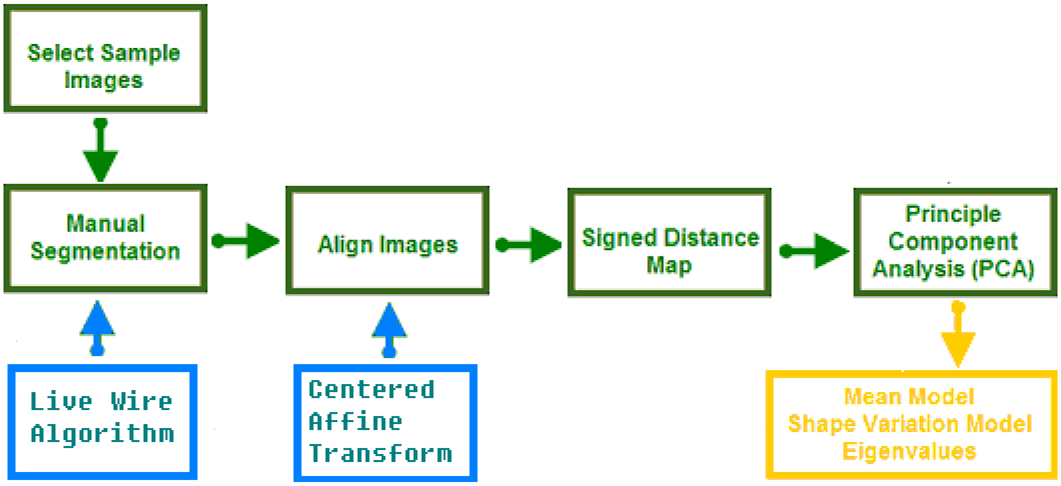

Figure 21 Flow Chart of Building Statistical Model

4.2 Training Set Preparation

The training set consists of a collection of raw image data, containing the shape information of the target structures. Selection of samples for the training set is the first step to derive a statistical model. There are three requirements for training set candidates in this study:

1) The image data is from healthy women with normal pelvic floor structures.

2) The image has good quality and no artifacts. Shape information of the target structures needs to be correct and intact, and the border of target structures can be clearly identified from images.

3) There are sufficient shape variations in the candidate images. In the study, training set images were selected from a MRI database at the Cleveland Clinic, and the image data was preprocessed to eliminate the patient's name and other identifying

information. All images data was inspected and confirmed by the Radiologist, Dr. Joseph C. Veniero MD, PhD (Radiologist of Section of Abdominal Imaging, Diagnostic Radiology Department of Cleveland Clinic) (Figure 22).

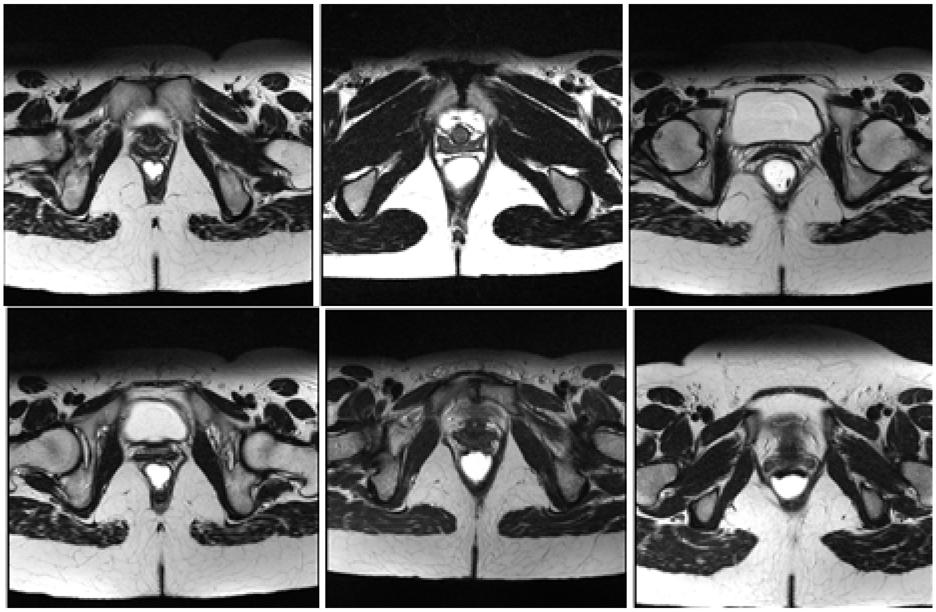

Figure 22 Examples of Training Set Images

Performance of the statistical model-based segmentation method has a close relation to the quality and quantity of training set samples. In order to derive a robust and reliable statistical model to represent the shape features of target structures, a certain quantity of samples with sufficient shape variation are required to be put into training set. Similar to neural network training, if the shape features of a target structure is considered as an unknown map, more data samples generally means more mesh points available and a smoother map can be constructed. However, those mesh points need to be evenly separated and cover each part of the map, otherwise the generated map will lose integrity.

On the other hand, more training samples do not necessarily mean that a better statistical model can be obtained. Redundant data, which has similar properties of other data in the training set, not only lowers the computational efficiency, but also decreases the performance of model searching in image segmentation. Putting redundant data into a training set can cause unbalanced property distributions in a generated statistical model.

The size of a training set is determined arbitrarily, and there is no certain standard that can be referred to. Generally, it depends on how many samples are available; but some rules can help to choose the proper size of training set [108].

4.2.1 Performance Requirement

For applications requiring quick processing, such as real-time target tracking and detection, a small training set can be used for modeling. On the contrary, if applications require high accuracy, a large training set needs to be used.

4.2.2 Properties of Target Structures

For those structures with complicated shapes, a large training set is more likely to be used for modeling than a small one.

4.2.3 Segmentation Results

If the performance of segmentation is not satisfactory and segmented images cannot capture key features of the target structures, more samples need to be put into the training set to rebuild the statistical model.

4.3 Manual Segmentation of Training Set Images

The purpose of manual segmentation is to separate target structures from the image background and the results are usually stored as a binary mask, which contain only two intensity values: 1 represents a white region and 0 represents black region. Manual segmentation is subjective, and prior knowledge of anatomy of the target structures and their normal appearance in MRI scans are essential for an accurate and reliable segmentation. Besides, software also plays an important role in improving the performance of manual segmentation.

Several software tools can be used to perform manual segmentation of medical images, such as Amira (www.amiravis.com), ImageJ (rsbweb.nih.gov/ij), and ITK-SNAP (www.itksnap.org/pmwiki/pmwiki.php). Amira is commercial software developed by Mercury while ImageJ and ITK-SNAP are both open source and free software. All of them provide some interactive segmentation tools that can help to speed the manual segmentation process. In ITK-SNAP and ImageJ, a polygon toolbox is used for segmentation by manually labeling points in the border of the target structure and automatically connecting those points to generate a contour (Figure 23). The polygon method is ok for simple shapes that are mainly composed of lines, but for complicated shapes composed of smooth curves, such as the levator ani muscle and obturator muscles, the generated contour is coarse and cannot accurately represent the shapes. Although smoothing algorithms can be applied to the contours afterwards, they also change the shape and area information and lead to inaccurate segmentation [109].

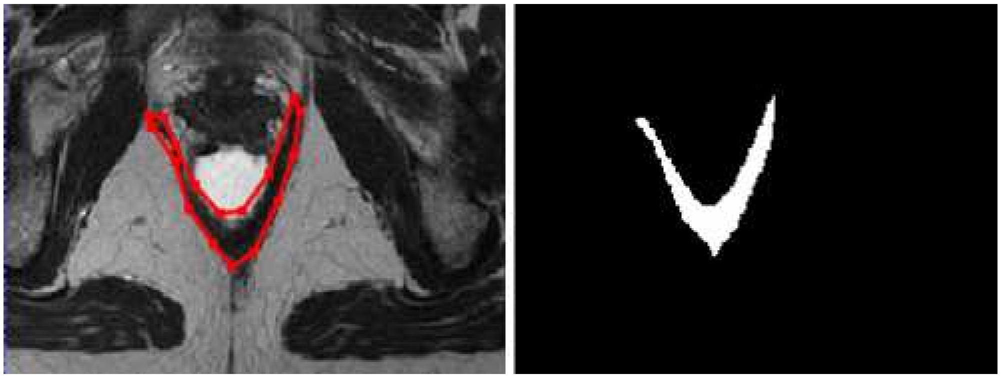

Figure 23 Manual Segmentation Using Polygon Toolbox (ITK-SNAP)

Compared to polygon tools, the live wire toolbox provided by Amira is much more suitable for manual segmentation of elastic objects. The live wire algorithm, sometimes also called intelligent scissors or magnetic lasso, was proposed by Eric Mortensen and William Barrett in 1995 [110]. During the segmentation, the user clicks on a pixel of a structure’s border as a seed point, and the program can stick to the contour of the structure as closely as possible by computing a path from the seed point to the mouse cursor. In order to compute such a path, the original image is converted to a node map in which each pixel is taken as a node. Each node is connected by links to its eight neighboring nodes, and the cost value of each link is the derivative of intensities across that link (Figure 24).

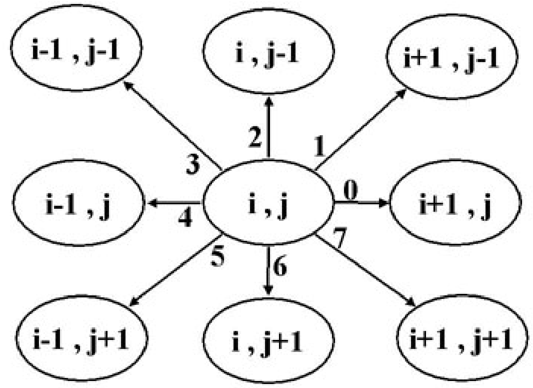

Figure 24 Node Link Map of Live Wire Algorithm

The path (live wire), which now can be represented as a sequence of links, is computed by finding the minimum cost path from the seed point to the current mouse position. Figure 25(a) shows how a live wire (in yellow) can be closely attracted to the border of levator ani muscle. Figure 25(b) is the result of manual segmentation where the levator ani muscle is labeled in red color. Figure 25(c) shows the binary result of manual segmentation where target structure is in white and background is in black. The final step of manual segmentation is to define the ROI, which only contains the target structure (Figure 25(d)). Analysis performed on ROI rather than on the entire image will greatly increase computational efficiency of building the statistical model and the modeling search process in a semi-automatic segmentation.

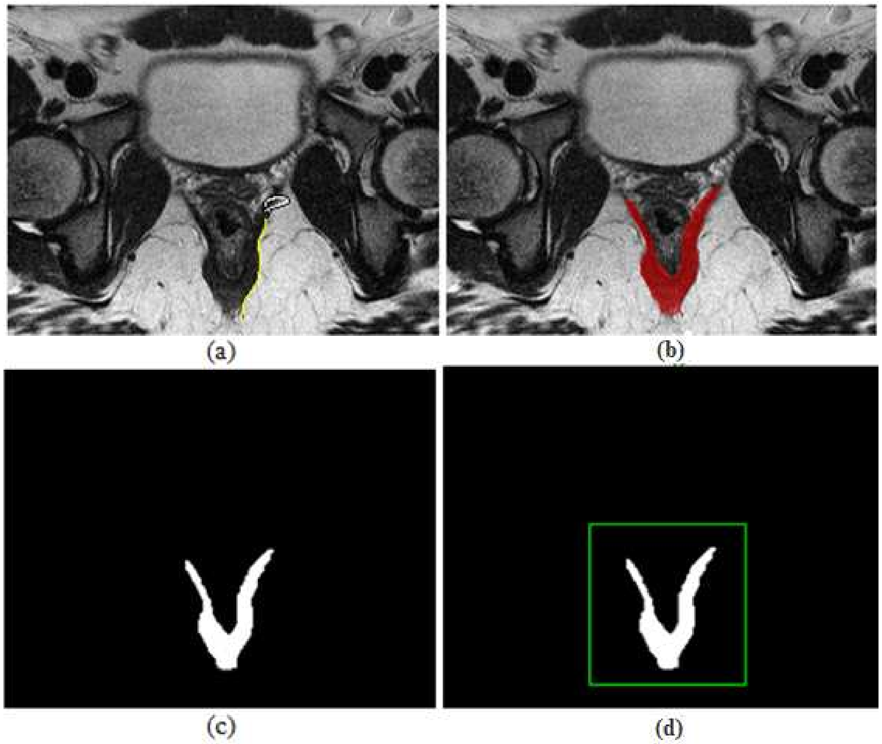
(a) (b) (c) (d)

Figure 25 Manual Segmentation of the Levator Ani Muscle with Live Wire

4.4 Alignment of Segmented Images

The proposed modeling method works by examining the statistics of the coordinate points of the distance maps of structures shapes. In order to compare equivalent points from different shapes, the binary masks of the target structure must be aligned in the same way with respect to a set of axes. The purpose of alignment is to filter out the differences in shapes due to translation, scaling, and rotation, which may be caused by differences in the human body or imaging parameters. Two issues need to be considered here for alignment. One is how to align any two shapes and the other is how to align multiple shapes.

In this dissertation, a robust image registration method, called centered affine transformation, is applied to align any two shapes of training set images. Different from rigid body transformation, which only contains translations and rotations, an affine transformation between two vector spaces (affine spaces) is composed of linear transformation (rotation, scaling, or shear) and a translation (Figure 26). An affine transform can be centered by specifying the center point of rotation, which usually is the centroid of structure [111].

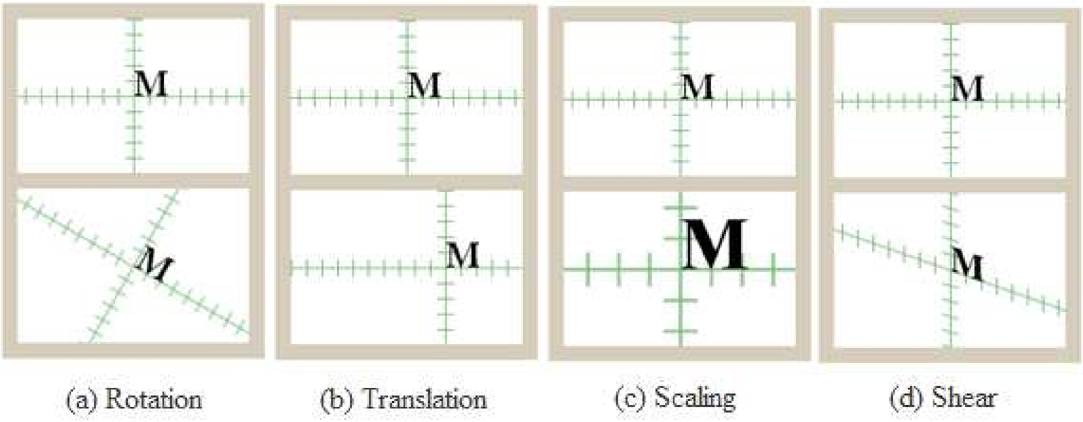

(a) Rotation (b) Translation (c) Scaling (d) Shear

Figure 26 Affine Transformation

In 2D images, suppose that a coordinate (x, y) is a point of structure before the transformation and that (u, v) is the location of that point after the transformation. Then the translation, scaling, rotational and shear transformations can be expressed by equation (8),(9),(10),(11) respectively [111]:

$$\begin{bmatrix} u \\ v \end{bmatrix} = \begin{bmatrix} x \\ y \end{bmatrix} + \begin{bmatrix} a \\ b \end{bmatrix} \tag{8}$$

$$\begin{bmatrix} u \\ v \end{bmatrix} = \begin{bmatrix} c & 0 \\ 0 & d \end{bmatrix} \begin{bmatrix} x \\ y \end{bmatrix} \tag{9}$$

$$\begin{bmatrix} u \\ v \end{bmatrix} = \begin{bmatrix} \cos\theta & -\sin\theta \\ \sin\theta & \cos\theta \end{bmatrix} \begin{bmatrix} x \\ y \end{bmatrix} \tag{10}$$

$$\begin{bmatrix} u \\ v \end{bmatrix} = \begin{bmatrix} 1 & S \\ 0 & 1 \end{bmatrix} \begin{bmatrix} x \\ y \end{bmatrix} \tag{11}$$

Where a and b denote the shift of origin of the old coordinates, c and d denote scaling coefficients of x and y respectively, θ denotes the rotation angles, and S denotes the shear factor in the x direction. Thus, an affine transformation can be expressed as:

$$\begin{bmatrix} u \\ v \end{bmatrix} = \begin{bmatrix} \cos\theta & -\sin\theta \\ \sin\theta & \cos\theta \end{bmatrix} \begin{bmatrix} c & 0 \\ 0 & d \end{bmatrix} \begin{bmatrix} 1 & S \\ 0 & 1 \end{bmatrix} \begin{bmatrix} x \\ y \end{bmatrix} + \begin{bmatrix} a \\ b \end{bmatrix} \tag{12}$$

We can see from the equation (12) that several linear transformations can be combined into a single one, so the affine transformation can also be expressed as:

$$P^{'} = AP + B \tag{13}$$

In which, A and B can be expressed as:

$$A = \begin{bmatrix} a11 & a12 \\ a21 & a22 \end{bmatrix} \tag{14}$$

$$B = \begin{bmatrix} b1 \\ b2 \end{bmatrix} \tag{15}$$

Similar to a 2D affine transformation, 3D affine transformation can also be expressed with the equation (13), with coefficient matrix expressed as:

$$A = \begin{bmatrix} a11 & a12 & a13 \\ a21 & a22 & a23 \\ a31 & a32 & a33 \end{bmatrix} \tag{16}$$

$$B = \begin{bmatrix} b1 \\ b2 \\ b3 \end{bmatrix} \tag{17}$$

As there are six parameters for a 2D affine transformation and twelve parameters for a 3D affine transformation, respectively, the alignment problem turns into finding the value of those parameters that can minimize the difference of two shapes. The difference of two shapes can be described by the sum of the squared Euclidean distance between pairs of correlation points, expressed by the following equation:

$$d(P, P') = \sum_{i=1}^{N} \left\| P_i - P'_i \right\| \tag{18}$$

The optimal translation vector can be obtained from the difference of the centroid of the two shapes (Cp and Cp’), which are express as:

$$Cp = \frac{1}{N}\sum_{i=1}^{N} P_i \qquad (19)$$

$$Cp' = \frac{1}{N}\sum_{i=1}^{N} P_i' \qquad (20)$$

The remaining parameters can be solved by using a standard optimization method such as derivative-free method or Lagrange multipliers [112]. MATLAB (product of the Math Works) incorporates those methods in its optimization toolbox, which can be used in the alignment application. The testing results of a centered affine transformation based on synthetic images are shown in Figure 27. The moving image has different pose (angles), size, and position (centroid coordinates) from the fixed images. With a centered affine transformation, the moving image is well aligned to the fixed image.

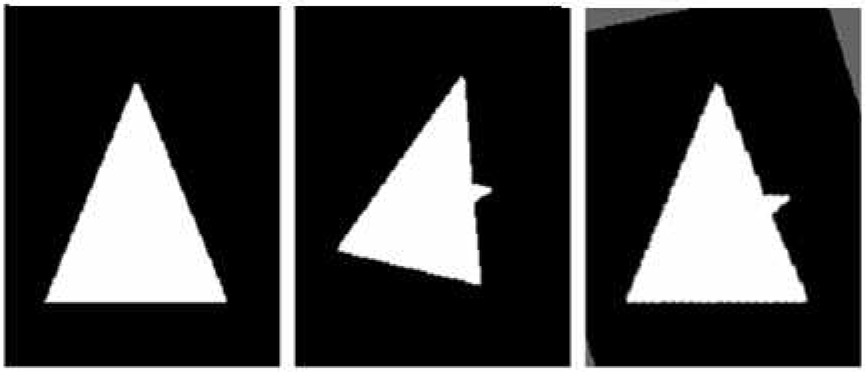

(a) Fixed Image (b) Moving Image (c) Result

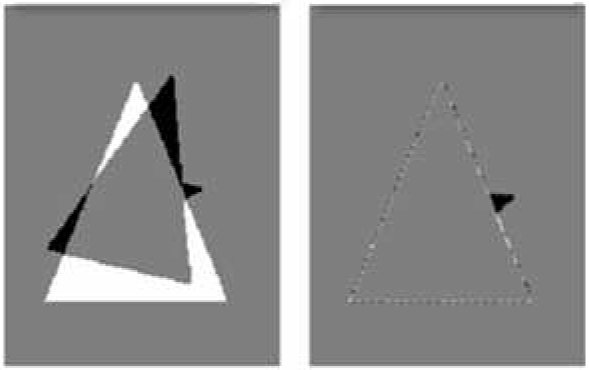

(d) Overlapped Image before Transformation (e) Overlapped Image after Transformation

Figure 27 Centered Affine Transformations

Results of transformation parameters are show in Figure 28.

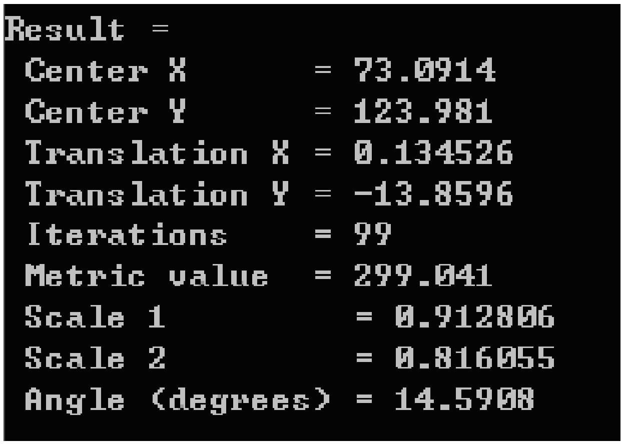

```
Result =
 Center X      = 73.0914
 Center Y      = 123.981
 Translation X = 0.134526
 Translation Y = -13.8596
 Iterations    = 99
 Metric value  = 299.041
 Scale 1         = 0.912806
 Scale 2         = 0.816055
 Angle (degrees) = 14.5908
```

Figure 28 Parameters for Center Affine Transformation

The method of alignment of two shapes also can be applied to alignment of multiple shapes. By arbitrarily selecting one shape from the training set as an initial shape (G_m), all the other shapes (S_i) can be aligned to it using the method described above. A mean shape can be generated from those aligned shapes by equation (21):

$$\bar{S} = \frac{1}{N}\sum_{i=1}^{N} S_i \tag{21}$$

Where S_i ($i=1....N$) are shapes that have been aligned to the initial shape. To reduce the effect of random selection of the initial shape, this procedure is executed for several iterations, and the similarity of two consecutive iterations is utilized to monitor convergence. The iteration stops automatically until the similarity value is greater than a predefined threshold. The flowchart of this method is shown in Figure 29, where κ denotes the similarity value and ε denotes the error threshold.

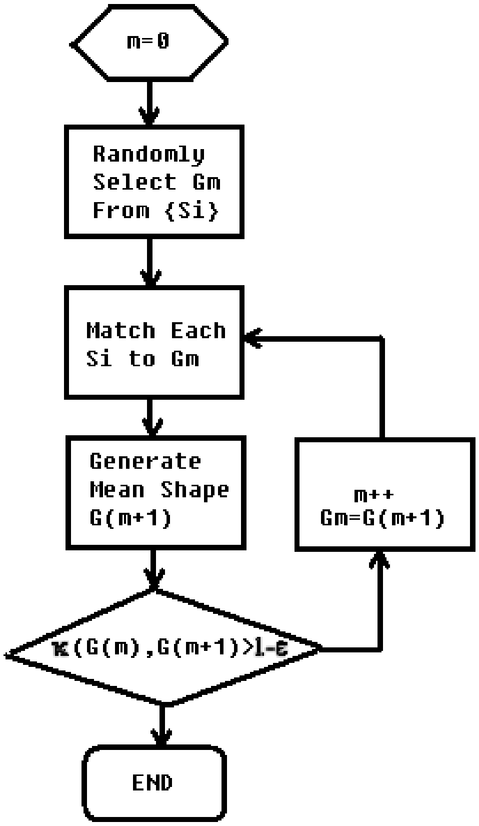

Figure 29 Flowchart of Shape Alignment

4.5 Calculating Distance Maps of Aligned Shape Images

The distance map is an operator normally applied to binary images and it is a representation of distance proximity of the point sets. Given a two-dimensional binary image I(x, y) by dividing all the pixels into the object pixels and the background pixels, the distance map I_d of this image is a matrix that assigns each object pixel with the distance to the nearest background pixel and is expressed in Equation (22):

$$I_d(x,y) = \begin{cases} 0 & (x,y) \in Background \\ \min(\| x - x0, y - y0 \|, \forall (x0, y0) \in Background & (x,y) \in Object \end{cases} \quad (22)$$

Where ||x, y|| is a distance metric.

The result of the transformation is a gray scale image that looks similar to the input image. The gray scale intensities of points inside foreground regions are changed to show the distance to the closest boundary from each point (Figure 30).

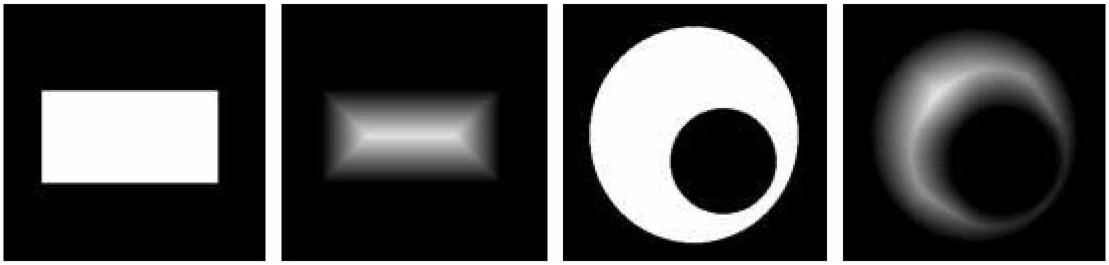

Figure 30 Distance Map

Distance maps are used for various applications, such as image and video blurring, path finding, and motion planning in robotics [113]. In image analysis, it can be used to measure objects or find relationships between objects [114]. Furthermore, it can also be used to classify certain objects in an image as foreground or background by defining a threshold. Several types of distance transformations are available, depending upon which distance metric is being used to determine the distance between pixels. The most commonly used distance operators are chessboard, Euclidean, city block and quasi-Euclidean [115].

The Euclidean distance map uses the form of a L2 norm, and is defined by equation (23):

$$\| x, y \| = \sqrt{x^2 + y^2} \qquad (23)$$

As shown in Figure 31(a), the pixel with value 0 stands for the border of an object while the pixel with value 1 denotes a pixel inside the object, and the red line is the path from that pixel to upper-right border pixel. Therefore, the length of red line is the Euclidean distance value, calculated as 1.414. By calculating the length of all eight paths, we can get a Euclidean distance transform map that is shown in Figure 31(b).

The Euclidean distance map is very useful since it represents the way that distances are measured in the real world. The metric is isotropic in that distances are independent of object orientation. However, it is difficult to calculate efficiently for objects with complex shapes in digital images [116].

0	0	0
0	1	0
0	0	0

Image

1.41	1.0	1.41
1.0	0.0	1.0
1.41	1.0	1.41

Distance Transform

Figure 31 Euclidean Distance Map

Several other metrics are used to calculate approximate distances between two pixels, such as city block, sometimes also called Manhattan metric. City block uses the

L1 norm where the distance is measured by the sum of horizontal and vertical steps in the path between two pixels [115]. The city block distance metric is defined in equation (24):

$$\| x, y \| = | x | + | y | \tag{24}$$

If each pixel is considered as a node and only connected to the four neighboring nodes in horizontal and vertical direction, then the city block distance is the minimum number of nodes that pass though when travel from one pixel to another. In Figure 32 (a), the city block path from inside pixel to the upper-right border pixel is shown in red line, therefore the distance value is equal to 2, which is shown in Figure 32 (b).

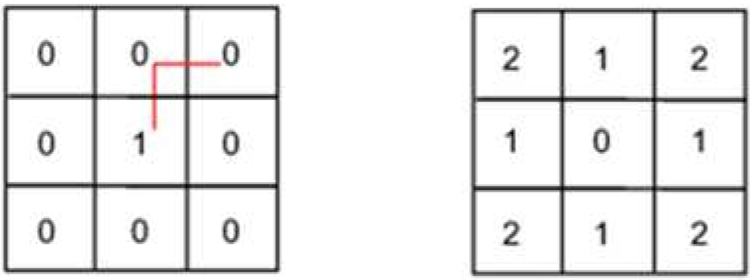

(a) Image (b) Distance Map

Figure 32 City Block Distance Map

Another approximation of Euclidean distance is the chessboard metric. Similar to the city block, the chessboard metric use an 8-connected node to calculate the distance between two pixels, while the node at a diagonal direction is considered to have the same distance as that in vertical and horizontal directions. In Figure 33(a), the chessboard path from inside pixel to the upper-right border pixel is show in red line, since all neighboring pixel are conceded to have same unit of distance value, the result is calculated as 1, which is shown in Figure 33 (b).

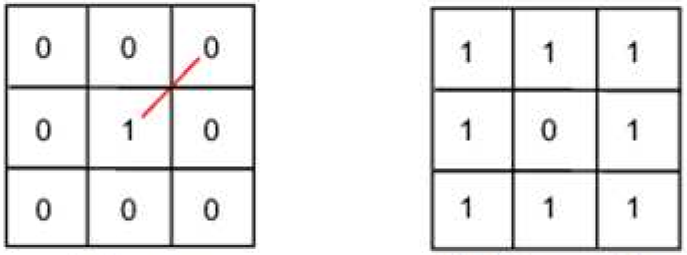

(a) Image

(b) Distance Map

Figure 33 Chessboard Distance Map

Both city block and chessboard approximation distance maps are easy to calculate, however, that is accomplished by sacrificing the accuracy. Compared to these two distance maps, the quasi-Euclidean distance map can better approximate the Euclidean distance metric while retaining the simplicity of calculation [117]. The quasi-Euclidean distance metric measures the minimum path between two pixels by a set of horizontal, vertical, and diagonal line segments, which is a hybrid method of city block and chessboard (Figure 34).

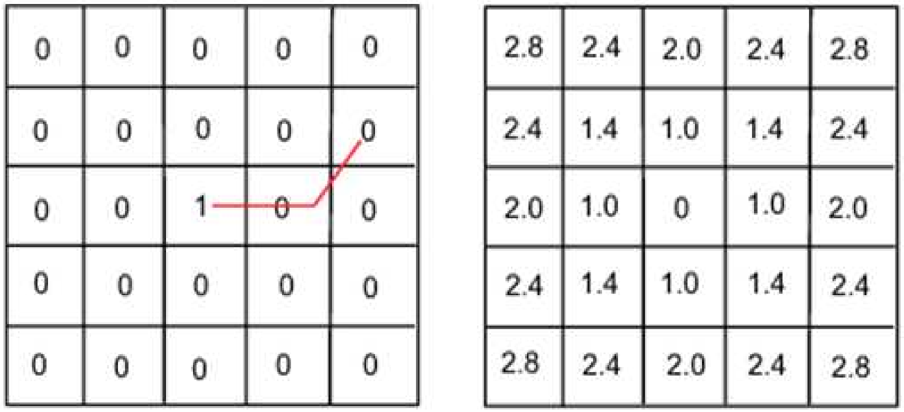

0	0	0	0	0
0	0	0	0	0
0	0	1	0	0
0	0	0	0	0
0	0	0	0	0

(a) Image

2.8	2.4	2.0	2.4	2.8
2.4	1.4	1.0	1.4	2.4
2.0	1.0	0	1.0	2.0
2.4	1.4	1.0	1.4	2.4
2.8	2.4	2.0	2.4	2.8

(b) Distance Map

Figure 34 Quasi-Euclidean Distance Map

In this dissertation, the quails-Euclidean metric is used to calculate the distance map of the training samples because structures of the pelvic floor have complex shapes. The distance map is calculated twice, during which the second calculation is based on inverted binary image (from white to black or from black to white), thus a signed distance map can be acquired by combining two distance maps with positive distance inside the shape and negative value outside the shape (Figure 35). The advantage of signed distance map is that it not only determines how close a given point x is to the boundary of shape (where distance is zero), but also tells if the pixel is inside or outside the boundary. In the later model matching (segmentation), such a signed distance map can guide the evolutionary contour or surface to update to the correct directions.

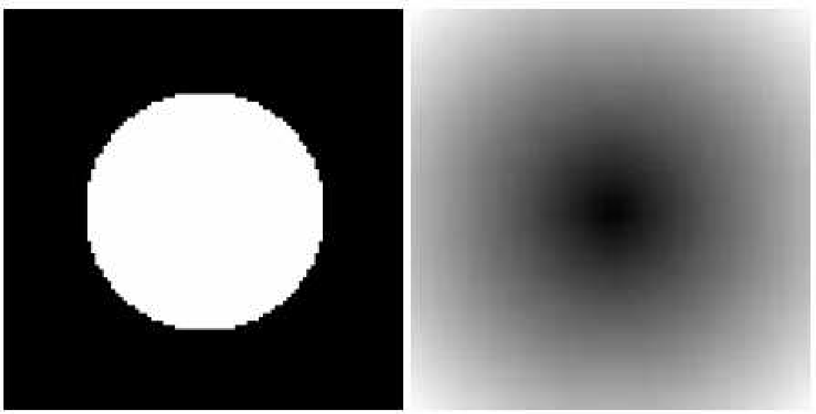

Figure 35 Example of Signed Distance Map

4.6 Principle Component Analysis

To model the variation of shapes in the training set, principle component analysis (PCA) is applied to signed distance maps. PCA is a standard data mining method that is mostly used in a variety of applications to find out inherent data structure [118]. The objective of PCA is to reduce the dimensionality of data set while still keeping the most variability. If a data set contains a large number of variables, modeling a data set is complicated or impractical. Furthermore, it is very likely those variables are correlated with each other. Thus, modeling a data set based on these correlated variables is inaccurate and unreliable. With the application of PCA, correlated variables can be transformed into a number of uncorrelated variables, and the most significant uncorrelated variables are defined as principle components [118]. Thus, the statistical model can be built based on the limited numbers of principle components (independent variables), and the model is capable of modeling the most of variability of the original data set.

In order to perform a dimensionality reduction, PCA uses a method to project a higher-dimensional data set samples into a subspace of much lower dimensionality. An example of performing PCA on 2D data set by projection method is illustrated in Figure 36. By projecting the data set to the one-dimensional space (i.e. axis) X' (in red line), where contains the largest variation, the first principle component is obtained as PC_1.Again, by projecting the subspace orthogonal to the first subspace, i.e. the axis Y' (in red line) perpendicular to the X', the second principle component is acquired as PC_2. Both principle components have their own direction and magnitude, and any point in the original data set can be express as the sum of the mean plus a linear combination of PC_1 and PC_2, which are expressed as:

$$x_i = \bar{x} + k_1 \cdot PC_1 + k_2 \cdot PC_2 \tag{25}$$

$$\bar{x} = \frac{1}{N}\sum_{i=1}^{N} x_i \tag{26}$$

In which, k_1 and k_2 represent coefficients for principle component PC_1 and PC_2 respectively.

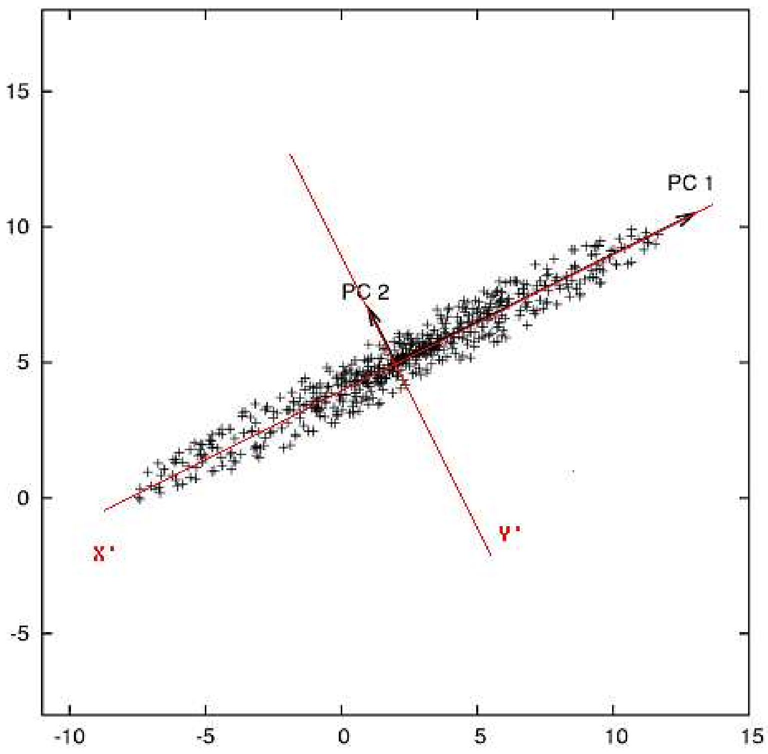

Figure 36 Example of Performing PCA on 2D Data Set

The principle components are usually sorted one by one with the most significant component at first position and the least significant one at last position. The principle components with less significance can be left out to reduce the dimensionality [79]. This is reasonable since the small variations in a data set often stand for the noise. For example, a point in above 2D data set can also be approximately expressed as:

$$x_i = \overline{x} + k_1 \cdot PC_1 \tag{27}$$

The dimensionality of the data set has been reduced to one-dimension since PC_1 covers the majority of variations.

Similar to 2D projection, 3D data set can be projected to a 2D surface containing the most variation. In this 2D space, the first and second principle components can be acquired using the same 2D projection method described above. Then a data set is projected to an axis perpendicular to the 2D surface. In this way, the third principle component can be acquired. Obviously, those three principle components are orthogonal to each other. 3D data set can be expressed as linear combinations of three, two, or one principle components. Similar to equation (27), 3D data set now can be expressed in a more general form:

$$x_i = \overline{x} + \sum_{i=1}^{M} ki \cdot Pi \tag{28}$$

Where Pi (i=1,…,M) is the most significant *M* principle components of the data set.

The projection method is intuitive for 2D or 3D data set, but impractical for the data set with the high dimensionality. In practical, PCA is performed as an eigenanalysis of the covariance matrix of the data set [79]. Let X be Nth dimensional vector expressed by the column vector, which stands for the original data set, and there will be an orthogonal transformation P matrix with N by N dimensions so that:

$$Y = P^T X \tag{29}$$

Where the covariance matrix of Y is a diagonal matrix and $P^{-1} = P^T$. If Cov (Y) and Cov(X) are used to denote the covariance matrix of Y and X respectively, The following equation (30) and equation (31) can be derived based on rules of the matrix operation.

$$\mathrm{Cov(Y)} = \frac{1}{\mathrm{n}-1}\mathrm{YY}^{\mathrm{T}}$$

$$= \frac{1}{\mathrm{n}-1}(\mathrm{P}^{\mathrm{T}}\mathrm{X})(\mathrm{P}^{\mathrm{T}}\mathrm{X})^{\mathrm{T}}$$

$$= \frac{1}{\mathrm{n}-1}\mathrm{P}^{\mathrm{T}}\mathrm{XX}^{\mathrm{T}}\mathrm{P}$$

$$= \mathrm{P}^{\mathrm{T}}\mathrm{Cov(X)P} \tag{30}$$

$$\mathrm{PCov(Y)} = \mathrm{Cov(X)P} \tag{31}$$

P can be rewritten as:

$$\mathrm{P} = \begin{bmatrix}\mathrm{P1} & \mathrm{P2} & \ldots & \mathrm{Pn}\end{bmatrix} \tag{32}$$

In addition, Cov(Y) can be expressed as:

$$\mathrm{Cov(Y)} = \begin{bmatrix} \mathrm{k1} & \ldots & \ldots & \ldots & 0 \\ \ldots & \mathrm{k2} & & & \ldots \\ \ldots & & \ldots & & \ldots \\ \ldots & & & \ldots & \ldots \\ 0 & \ldots & \ldots & \ldots & \mathrm{kn} \end{bmatrix} \tag{33}$$

Equation (34) can be derived based on equation (32) and (33):

$$\begin{bmatrix} k1P1 & k2P2 & \ldots & knPn \end{bmatrix} = \begin{bmatrix} cov(X)P1 & Cov(X)P2 & \ldots & Cov(X)Pn \end{bmatrix} \tag{34}$$

Where Pi is an eigenvector of the covariance matrix of X and the ki is an according eigenvalue. When these eigenvalues are sorted from large to small, the eigenvector with the biggest eigenvalue is the most significant principle component.

This study assumes that there are n aligned and scaled shapes in the training set, they are described as vectors (Si, i=1..n),and each shape consists of m points signed distance map, so those shapes can be expressed as column vectors, and the average shape can be obtained through the alignment:

$$\overline{S} = \frac{1}{n}\sum_{i=1}^{n} Si \tag{35}$$

The covariance matrix thus can be given as:

$$Cov(S) = \frac{1}{n}\sum_{i=1}^{n} (Si - \overline{S})(Si - \overline{S})^{T} \tag{36}$$

The principle component of shape variation can be obtained as eigenvectors of Cov(S), Φi and according eigenvalue λi (λi>= λi+1). If the first t eigenvectors are selected as principle components for modeling, a new shape instance can be generated by the following equation:

$$S' = \bar{S} + \sum_{i=1}^{t} bi \cdot \phi i \tag{37}$$

Vector b is called the shape variation control vector. Since the eigenvalue λi calculated in the PCA is the maximum of likelihood estimates for the variations, the according standard deviation is:

$$\sigma i = \sqrt{\lambda i} \tag{38}$$

It has been approved by applying the limits to the shape variation vector b with the following Equation:

$$bi \leq \pm 3\sqrt{\lambda i} \tag{39}$$

A new shape instance that is similar to the training set shapes can be generated in this way [66].

In this chapter, a modeling method of statistical shape model is elucidated. A reliable and accurate model is essential for proposed model-based segmentation method. Building such a model involves several steps. At first, a proper imaging technique is required to obtain the raw image data. In this study, MRI was used for the female pelvic floor imaging since it has better contrast for soft tissue and high resolution compared to CT and ultrasound. Secondly, a certain number of image data is examined and selected into training set, and then manual segmentation of structure shape is performed with live wire tools. Thirdly, shapes of structure are aligned using a centered affine transformation and a mean shape model can be generated. Fourthly, signed distance maps are calculated based on aligned structures shapes, using quasi-Euclidean distance metric. Compared to other distance metric, the quasi-Euclidean distance metric is more accurate but still has decent computational efficiency. Finally, PCA is performed to obtain the shape variation models using eigenanalysis. Eigenvectors are sorted by eigenvalues and only the first several vectors are chosen to build the statistical shape model. With mean shape model and shape variation model, a new instance of structure that has the similar shape to those in the training set can be generated with limited changes of shape control parameters.

CHAPTER V

LOCAL FEATURE MAP AND MODEL MATCHING

5.1 Introduction

Given a statistical shape model and a new image, the proposed segmentation method first generates a local feature map from the image and then superimposes the mean model over the feature map. During the matching process, the image feature map will attract a contour or surface to the boundaries of the target structure while the variation model will maintain the shape in a reasonable way. Several steps are involved in extraction of the local feature map from unseen images, including importing MRI data, adjusting the window and level value, reducing noise and calculating the gradient magnitude. Details of these steps are described in the following sections.

5.2 Import MRI Data

The MRI scans are saved as Digital Imaging and Communication in Medicine 3.0 (DICOM), a digital imaging standard created by the American College of Radiology (ACR) and National Electrical Manufacturers' Association (NEMA) [119]. The objective of this standard is to aid in storing, distribution, and viewing of medical images, such as CT, MRI, and ultrasound. DICOM is a comprehensive set of standards, which specify a file format definition as well as a network communication protocol [120]. A single DICOM file contains a header and a body of image data. The file header consists of both standardized fields and free-form fields; the former are a public DICOM dictionary while the latter are a DICOM shadow dictionary [121]. In this study, a MATLAB DICOM parser is used to import DICOM image file and decode compressed image data.

5.3 Window and Level Operation

Medical images are typically recorded with 16-bit intensities so each pixel or voxel of the image is represented by an integer from 0 to 65535. Since each structure has its own intensity distribution, intensity range that best represents the target structures is usually selected for display or study. The method to define the intensity range is called window operation, which consists of two parameters: window center and window width [122]. If a selected intensity range is from I_L to I_H, a window center (W_C) is defined in equation (40):

$$W_C = \frac{1}{2}(I_L + I_H) \tag{40}$$

A window width (W_W) is defined in equation (41):

$$W_W = I_H - I_L \tag{41}$$

Figure 37 demonstrates that two different window operations are performed on the same MRI scan. From the images, the levator ani muscle and obturator muscles are better displayed with the window setting W_C =197 and W_W =212 (Figure 37(b)), while the bladder is better displayed with W_C =282 and W_W =79 (Figure 37(c)).

For a series of MRI scans with the same imaging protocol, the same window parameter should be applied to extract information from the target structure; however, a window setting that works well for one protocol will probably be useless with a different protocol or on a different MRI scanner [122].

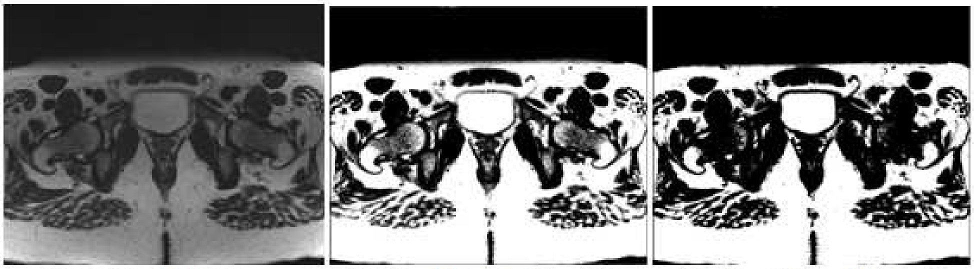
(a) Original MRI Scan (b) Wc=197 and Ww=212 (c) Wc=197 and Ww=79

Figure 37 Example of Window Operation

A level operation is another method that allows the user to adjust the contrast and brightness of the digital image to enhance the target structure. Level operation sometimes is also called intensity mapping. Although medical images are able to recorded with 16-bit intensities, they only can be displayed with 8-bit grayscale intensities, i.e., from 0 to 255. The selected intensity window needs to be mapped to 8-bit grayscale intensities for display, while other pixels with values outside of the window are either mapped to 0 for black or 225 for white. The intensity window can also be mapped to a smaller intensity range, in which the low threshold is greater than 0 and the high threshold is less than 255. Several intensity mapping methods can be performed on the MRI scans as detailed below.

5.3.1 Linear Mapping

Linear mapping is a typical mapping method that forces a dynamic range of intensities to be fit within a particular intensity scale [123]. The linear mapping equation is expressed as:

$$\mathrm{Output} = [\mathrm{Input} - (\mathrm{Wc} - \frac{1}{2} \times \mathrm{W_W})] \times \frac{(\mathrm{M_H} - \mathrm{M_L})}{\mathrm{W_W}} + \mathrm{M_L} \qquad (42)$$

Where M_L denotes the low threshold for mapping intensities and M_H denotes the high threshold for mapping intensities. Linear mapping is shown in the Figure 38. The human eye is limited in its ability to discern the small intensity difference since it is too similar. With certain level operations, the ratio between the mapping range and the window width can be greater than 1, thus the intensity difference in the original image is enlarged and people can see more details of target structure [124]. This is also called contrast enhancement.

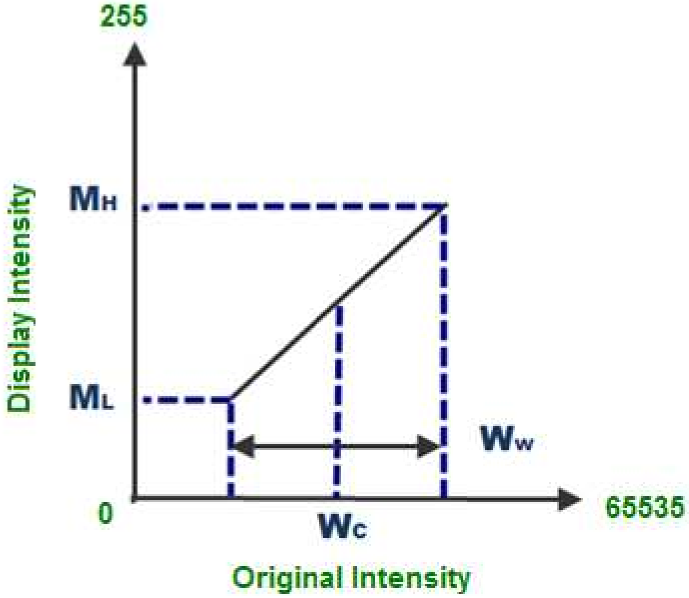

Figure 38 Linear Intensity Mapping

5.3.2 Normalized Mapping

In normalized mapping, the grayscale intensities in the output image are transformed to have a mean of zero and a variance of one using the following equations.

$$\text{Output} = \frac{(\text{Input} - \mu)}{\sqrt{\sigma^2}} \tag{43}$$

$$\mu = \frac{1}{N}\sum_{i=1}^{N} \text{Ii} \tag{44}$$

$$\sigma^2 = \frac{1}{N}\sum_{i=1}^{N} (\text{Ii} - \mu)^2 \tag{45}$$

Where Ii (i=1...N) is all the intensity values in a selected intensity window, μ is the mean and σ^2 is the variance [123]. This intensity mapping is particularly useful in medical image registration applications as a preprocessing step to the evaluation of mutual information metrics [125].

5.3.3 Histogram Mapping

Histogram mapping, also called histogram equalization, is a method, which can alter the intensity distribution in an original image to a Gaussian distribution in a mapped image [123] . Consider a 2D image (M x N) which contains L levels of grayscale intensities. The possibility of an occurrence of a pixel of certain intensity I can be expressed as:

$$P(I) = \frac{n_I}{M \times N} \tag{46}$$

Where $0 \leq I \leq L$, and the cumulative distribution for intensity I can be expressed in Equation (47):

$$CD(I) = \sum_{J=0}^{I} P(J) \tag{47}$$

In order to get a Gaussian distribution of intensity in the new image, the mapped cumulative distribution needs to be linear across the new intensity value range, i.e., 0 to 255. This requires a transformation of intensity values based on the following equation:

$$I' = T(I) = \mathrm{round}\left(\frac{CD(I) - \mathrm{Min}(CD)}{M \times N - \mathrm{Min}(CD)} \times 255\right) \tag{48}$$

In which, Min (CD) is the minimum value of the original cumulative distribution.

5.3.4 Nonlinear Mapping

Compared to the linear mapping, nonlinear mapping utilizes a smooth and continuous nonlinear transformation function instead of a linear function. Among different kinds of nonlinear functions, the sigmoid function is one of the most widely used, with the goal to focus attention on a particular set of values and progressively attenuate values outside that range [123]. A sigmoid mapping is expressed as:

$$P(x) = \frac{1}{1+e^{-x}} \tag{49}$$

A sigmoid curve is shown in Figure 39.

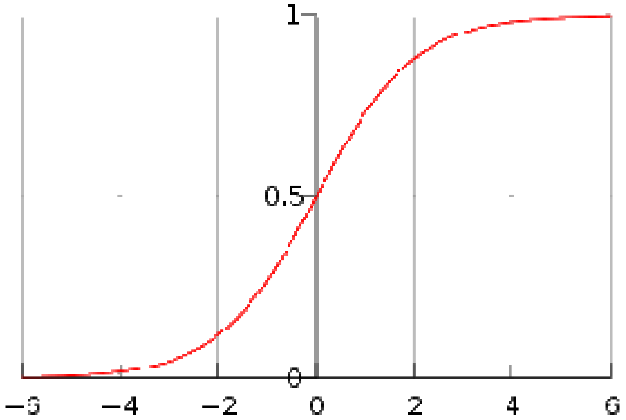

Figure 39 Sigmoid Function

In this study, a nonlinear sigmoid mapping is applied for intensity mapping of MR images. However, the sigmoid function used here is modified by adding two control parameters. It is expressed as:

$$P(x) = \frac{1}{1+e^{-(\frac{x-\beta}{\alpha})}} \tag{50}$$

In which, α defines the width of the input intensity range, i.e. intensity window, and β defines the intensity around which the range is centered (Figure 40(a) and (b)).

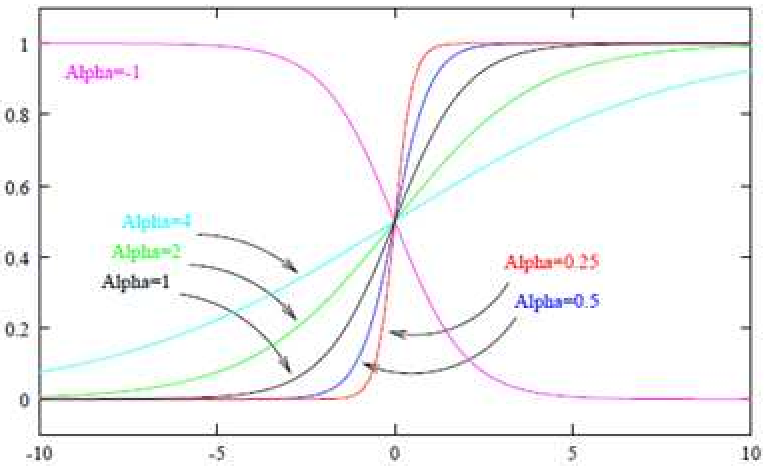

(a) Alpha

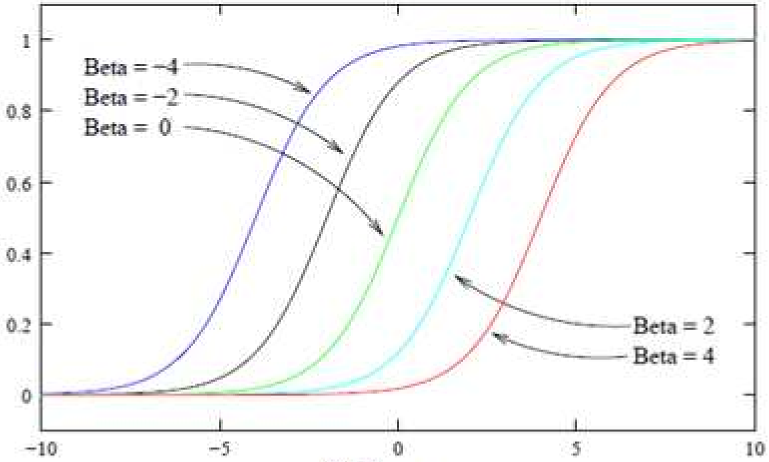

(b) Beta

Figure 40 Modified Sigmoid Intensity Mapping

5.3.5 Noise Reduction

For medical images, noise is always involved in the signal due to the limitations of imaging hardware and protocols. Noise reduction is one the most important objectives for medical image processing. Almost all model-free segmentation methods are sensitive to noise in images. Although mode-based methods are more robust, too much noise still can lead to an unsatisfying segmentation result.

Usually, an image is smoothed to remove certain noise by applying a convolution operation onto the image with a certain smoothing kernel, such as a Gaussian convolution kernel. In a 2D image, a continuous Gaussian kernel is defined by equation (51):

$$G(x, y) = \frac{1}{2\pi\sigma^2} e^{-\frac{x^2+y^2}{2\sigma^2}} \qquad (51)$$

The distribution of the above kernel has zero mean and variance of one. In digital image processing, the Gaussian kernel is expressed in a discrete form with a certain size. For example, a 5x5 Gaussian kernel is shown in Figure 41. The kernel is symmetric in both vertical and horizontal directions, and the sum of all kernel elements equals to 1 (by multiplying 1/273 to each kernel element), which guarantee the stability of convolution operation on image data.

$$\frac{1}{273}\begin{array}{|c|c|c|c|c|}\hline 1 & 4 & 7 & 4 & 1 \\ \hline 4 & 16 & 26 & 16 & 4 \\ \hline 7 & 26 & 41 & 26 & 7 \\ \hline 4 & 16 & 26 & 16 & 4 \\ \hline 1 & 4 & 7 & 4 & 1 \\ \hline \end{array}$$

Figure 41 5x5 Discrete Gaussian Smoothing Kernel

The drawback of the Gaussian smoothing method is that it also tends to blur the sharp boundaries in the image while removing the noise. Even smoothing does not obliterate boundaries of the image, it tends to distort the fine structure of the image and thereby changes subtle aspects of the anatomical shapes [126].

As a proposed method here, an anisotropic diffusion algorithm is used to reduce noise of MRI scans without removing significant features of edges of the structure. Anisotropic diffusion was proposed by Perona and Malik in 1990 [109], so it is also called a Perona-Malik diffusion. In anisotropic diffusion algorithm, a Gaussian smoothed image can be taken as a solution to a heat diffusion equation with respect to a certain time value t. The heat diffusion equation is in the form of

$$\frac{\partial g(x,y,t)}{\partial t} = \nabla \cdot \nabla g(x,y,t) \tag{52}$$

$$f(x,y) = g(x,y,0) \tag{53}$$

$$g(x,y,t) = G(\sqrt{2t}) \otimes f(x,y) \tag{54}$$

In which, f (x, y) is an input image, g (x, y, t) is a Gaussian smoothed image with parameter of t, and G is a Gaussian kernel. Anisotropic diffusion includes a variable conductance term, which depends on the differential results of the images. Smoothing can be controlled by formulating this variable conductance. The modified heat diffusion equation can be expressed as:

$$\frac{\partial g(x,y,t)}{\partial t} = \nabla \cdot c(|\nabla g(x,y,t)|)\nabla g(x,y,t) \tag{55}$$

$$c(|\nabla g(x,y,t)|) = e^{-\frac{|\nabla g(x,y,t)|^2}{2k^2}} \tag{56}$$

In which, c is the variable conductance term. At a certain time slice, with Gaussian smoothing filter G (2t), the original image is smoothed. Since the edges of the structure in the smoothed images have higher gradient magnitude than that of a non-edge region, the conductance is reduced, and the smoothing effect is limited. Beside the time-dependant gradient magnitude, the conductance value is also depends on k, the conductance parameter. The parameter k controls the sensitivity of the process to the structure edge.

There are two control parameters for an anisotropic diffusion filter, t and k, while t can be also looked as σ, the width of the discrete Gaussian smooth kernel.

Equation (37) is a nonlinear partial differential equation and can be solved by using a finite forward difference method in discrete space of x, y and t [109]. Thus, an iteration number also needs to be defined when using anisotropic smoothing. The flowing image (Figure 42) shows an example of an anisotropic diffusion with the control parameters assigned as k= 3, σ = 0.25 and iteration =5.

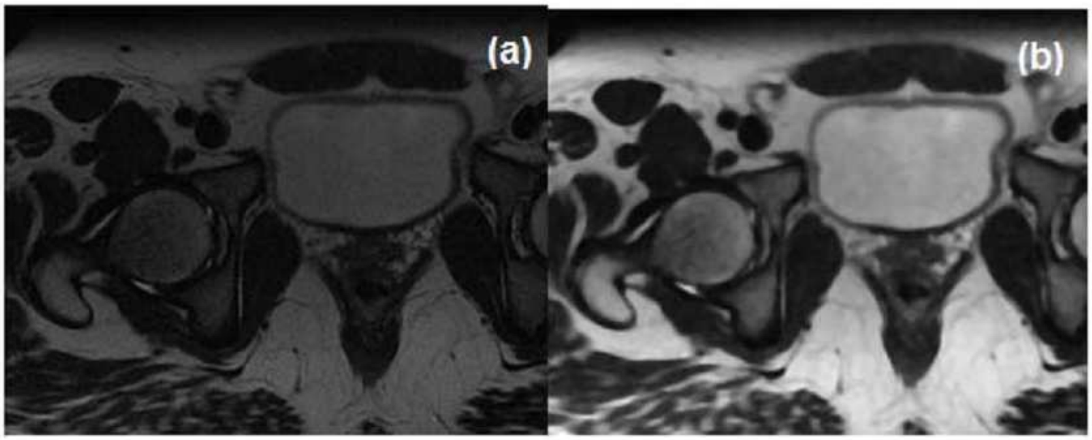

Figure 42   Example of Anisotropic Diffusion Smoothing

5.4 Gradient Calculation

For extracting features of edges of target structures in local images, the gradient maps are calculated from smoothed MRI scans. A gradient map describes how the intensity of each pixel or voxel changes by providing two pieces of information: The magnitude of gradient tells how quickly the intensity changes, and the direction of the gradient tells in which direction the intensity changes most rapidly. In medical images, the sharp intensity changes are often across the edges of structures, so gradient magnitude maps are especially useful for extracting all of the possible structure edges based on local image information.

Mathematically, the gradient of a continuous function with two variables is defined as a vector with the components given by the partial derivatives of variables and can be expressed as:

$$\nabla f(x, y) = \left(\frac{\partial f}{\partial x}, \frac{\partial f}{\partial y}\right)$$

$$= \frac{\partial f}{\partial x}\vec{i} + \frac{\partial f}{\partial y}\vec{j} \qquad (57)$$

However, for a 2D image, since the intensity function is discrete, partial derivatives of the function can only be defined by assuming there is an underlying continuous function, and intensities are sampled at image points of this continuous function. Although the derivatives at any point are functions of intensity values of all the image points, approximation of derivatives of certain points can be calculated using the limited image points in a surrounding area.

The gradient magnitude of a continuous function is calculated in the form of equation (58):

$$\left|\nabla f(x,y)\right| = \sqrt{(\frac{\partial f}{\partial x})^2 + (\frac{\partial f}{\partial y})^2} \tag{58}$$

The approximate gradient magnitude of the discrete points can be calculated by equation (59).

$$\left|\nabla f(x,y)\right| = \left|\frac{\partial f}{\partial x}\right| + \left|\frac{\partial f}{\partial y}\right| \tag{59}$$

Approximate gradient magnitude is usually calculated by performing a convolution operation on the target image by certain convolution kernels. Different kernels can be used with lesser or larger degrees of accuracy and the most commonly used methods are called Roberts and Sobel [123]. The Roberts Cross operator consists of a pair of 2x2 convolution kernels and performs a simple 2-D spatial gradient measurement on an image (equation (60) and (61)).

$$G_x = \begin{bmatrix} 1 & 0 \\ 0 & -1 \end{bmatrix} \tag{60}$$

And

$$G_y = \begin{bmatrix} 0 & 1 \\ -1 & 0 \end{bmatrix} \tag{61}$$

For the pixels in the example shown in Figure 43:

P_1	P_2
P_3	P_4

Figure 43 Example of Pixels (1)

The gradient can be calculated by equation (62):

$$G = |P1 - P4| + |P2 - P3| \tag{62}$$

The Roberts Cross highlights regions of high spatial frequency, which often correspond to the edges.

The Sobel Operator consists of a pair of 3x3 kernels (equation (63) and (64)).

$$G_x = \begin{bmatrix} 1 & 0 & -1 \\ 2 & 0 & -2 \\ 1 & 0 & -1 \end{bmatrix} \tag{63}$$

And

$$G_y = \begin{bmatrix} 1 & 2 & 1 \\ 0 & 0 & 0 \\ -1 & -2 & -1 \end{bmatrix} \tag{64}$$

Similarly, for the pixels shown in the example shown in Figure 44, the gradient can be calculated as:

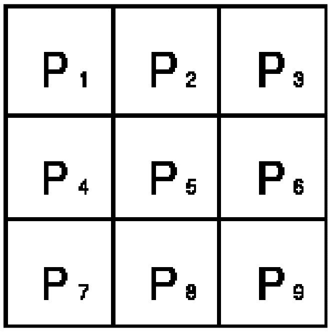

Figure 44   Example of Pixels (2)

$$G = |(P1 + 2 \cdot P2 + P3) - (P7 + 2 \cdot P8 + P9)| + |(P3 + 2 \cdot P6 + P9) - (P1 + 2 \cdot P4 + P7)| \quad (65)$$

Compare to Robert Cross, Sobel operator is more accurate. Furthermore, it can be easily extended to a 3D image, using the following convolution kernel (equation (66), (67) and (68)):

$$G(:,:,-1) = \begin{bmatrix} 1 & 2 & 1 \\ 2 & 4 & 2 \\ 1 & 2 & 1 \end{bmatrix} \qquad (66)$$

And

$$G(:,:,0) = \begin{bmatrix} 0 & 0 & 0 \\ 0 & 0 & 0 \\ 0 & 0 & 0 \end{bmatrix} \qquad (67)$$

And

$$G(:,:,1) = \begin{bmatrix} -1 & -2 & -1 \\ -2 & -4 & -2 \\ -1 & -2 & -1 \end{bmatrix} \tag{68}$$

5.5 Normalization

The gradient magnitude needs to be normalized before using as an input for model match. A reciprocal filter is applied to a gradient magnitude image (equation (69)).

$$N(x) = \frac{1}{1 + G(x)} \tag{69}$$

An example of gradient magnitude normalization is shown in Figure 45.

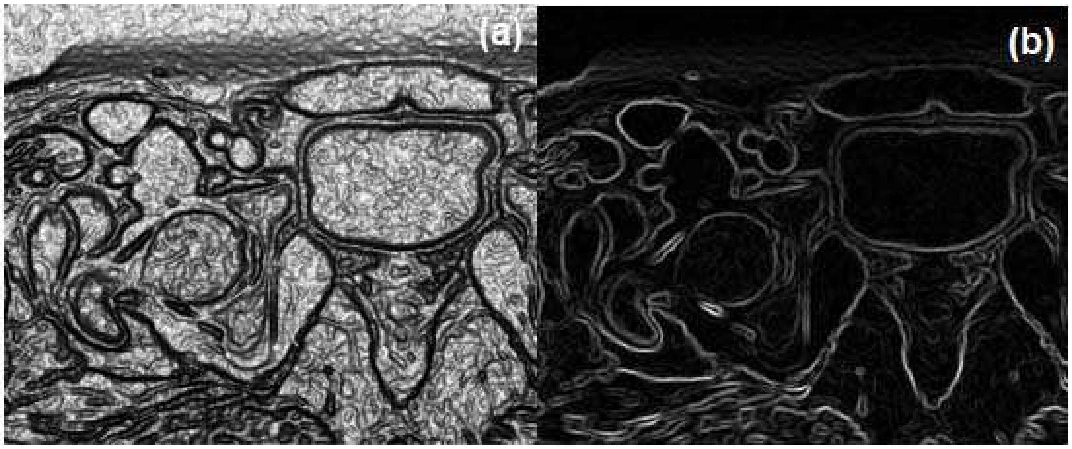

Figure 45 Example of Gradient Magnitude Normalization

5.6 Model Matching

Given a statistical model and an image feature map, the model-based segmentation of unseen data is to first superimpose an initial contour or surface over the image and then update the curve or surface with the guidance of a feature map and shape model. A statistical model allows one to describe the target structure and its shape variations in a compact way. On one hand, a new instance of shape can be generated by assigning proper values for few control parameters of principle components of variances. On the other hand, an image feature map contains local image features (normalized gradient magnitudes) of boundaries of the structures. During the matching process, the image feature map will attract the model to the boundaries of target structures while the statistical model will maintain the contour or surface shape in a reasonable way. The contour or surface evolves until the stop criterion is achieved, the stop criterion can be either a predefined error threshold or the number of iterations. The iterative change of evolutionary contour or surface can be expressed in equation (70).

$$\Delta = \mathrm{Se}(i+1) - \mathrm{Se}(i) = J \cdot [S_f(I)(c+\xi)\,|\nabla \mathrm{Se}(i)|] + K \cdot [S_m(i) - \mathrm{Se}(i)] \tag{70}$$

Where the J and K are scale values that define the weight of influence of local image features and shape models, respectively. The first term of Equation(70) is based on Casella's boundary detection model [127], where S_f is the image feature map, Se is the evolutionary curve or surface, ξ is the curvature of the contour or surface, and c is a positive real constant which controls the propagation step of the evolutionary curve or surface.

In the first term, S_e will be attracted to feature map S_f, while keeping the smoothness of the evolving contour or surface.

In the second term, S_m (i) is the best-fit shape model for the current contour or surface Se (i). Since the statistical shape model has filtered out position rotation and scaling information, such information needs to be restored in the model matching. A proposed new shape instance is expressed in equation (71).

$$S_m(i) = M(R(i), \theta(i))[S'(i)] + T(i) \qquad (71)$$

Where M(R(i), θ(i)) is a rigid body transformation, θ (i) is the rotation angle, R(i) is the scaling, and T(i) is the translation vector. S'(i) is determined by mean shape and principle components of the shape variation model and can be expressed in equation (72).

$$S'(i) = \bar{S} + \sum_{j=1}^{t} Bj(i) \cdot \phi j(i) \qquad (72)$$

Where B is the shape control parameter vector and Φ is the principle component vector composed of the j largest eigenvectors. The problem can be turned into an optimization process, which tries to find a proper shape control parameter and transformation parameter that minimize the difference between the model and the current shape. Such a difference can be expressed as an energy/cost function in the form of:

$$E = \mathrm{diff}(S_m(i), S_e(i)) = \sqrt{\sum_{i=1}^{N} (S_{e,pi} - S_{m,pi})^2} \tag{73}$$

The parameters of a new shape instance (θ, R, T, B) are obtained by using an evolutionary strategy (ES). ES is one of three main research areas of Evolutionary Algorithms. It is mainly used for variable optimization. The first ES was developed in 1962 at Technical University of Berlin and was used for proportional–integral–derivative (PID) control of nonlinear systems. After that, different types of ES were developed and applied in a variety of applications such as image processing, computer vision, task scheduling and car automation [128]. Compared to Genetic Algorithms (GA), another main research area of Evolutionary Algorithms, ES is easier to implement and faster than GA because of the following differences [129]:

1) GA uses binary strings while ES uses real values to present parameters of optimization.

2) GA incorporates both crossover and mutation while ES only uses mutation.

Among all ES, the most widely used is two-member ES, which is sometimes called (1+1)-ES. (1+1)-ES uses a mutation-selection scheme, in which a child was generated from its parents and then the performance was compared with the two members. The better one is selected for the next generation while the other is discarded. Here is the general scheme of (1+1)-ES:

1) Generate a parent vector X=(x1, x2, …, xm). Each parameter is chosen randomly while also satisfies the constraints.

2) Create a child vector by mutation. A random vector of size X with normal distribution is added here:

$$X' = X + N(0, \sigma) \tag{74}$$

3) Compare the results of X’ and X, choose the better one for the next generation.

4) Repeat step 2) and 3) until a satisfactory solution is reached.

While being applied in the model matching, the (1+1)-ES updates the parameter vector by testing random permutation of the parameters. At first, (1+1)-ES explores the parametric space, which is composed of the shape control vector and the transform vector (scaling, translation, and rotation). Secondly, the child parameter vector is randomly generated around the current position (parent parameter vector) by adding a randomly generated vector with normal distribution. The covariance matrix of the child parameter is then calculated. The variances in the matrix are increased when the new point produces higher fitness values, and are decreased when the new point produces lower fitness values.

This chapter describes how to extract local image feature map from unseen image data and how to segment target structures based on feature map and statistical shape model. In this study, a specially designed filter sequence is applied on unseen MR images to get the border of target structure. First, a nonlinear sigmoid intensity mapping function is used for windowing and leveling operation to enhance the contrast of target structure. Compared to linear mapping function, the modified sigmoid function is smoother in intensity mapping and window center and window width can be flexibly defined. Secondly, an anisotropic filter is applied to reduce noise and smooth image. Compared to Gaussian filter, anisotropic filter can better keep the feature of the border of structures. Thirdly, gradient magnitude is calculated with Sobel operator, which can be used in both 2D and 3D images. Lastly, the gradient magnitude is normalized using a reciprocal filter.

With the statistical shape model and feature map of unseen data, segmentation is done by model matching, using ES. An initial smooth contour or surface is put inside the structure and then the feature map attracts the contour or surface to the border of structures while the statistical shape model maintains the shape of contour or surface in a reasonable way. The weights can be defined for shape model and feature map respectively to control the influence on the contour or surface. (1+1) ES is applied to update of shape model parameters. (1+1) ES has the advantages of easy implementation and high computational efficiency, which make it good candidate for real-time image application.

CHAPTER VI

PERFORMANCE EVALUATION AND TAGUCHI ANALYSIS

6.1 Performance Evaluation of Segmentation Method

Although extensive research has been conducted on developing different algorithms for medical image segmentation, evaluation of segmentation results thus far has been largely subjective and the most common method for evaluation is to compare the image segmentation results visually with manually segmented reference images [130]. The subjective and supervised evaluation is a tedious and time-consuming process and lacks consistency and reproducibility. Evaluation scores may vary from one evaluator to another, since each has his or her own standards for accessing the quality of segmentation results [131]. In this study, the target structures have complicated shapes and lot of control parameters are involved in segmentation process. Therefore, an unsupervised performance evaluation method is required, which enables the objective comparison of different parameterizations of the proposed segmentation method.

In this dissertation, a similarity value of semi-automatic segmentation results and the value of manual segmentation results are used to evaluate the performance of the semi-automatic segmentation. Specifically, for 2D images, the area of overlapped regions and the area of total regions are calculated respectively, and a Dice coefficient equation is used to calculate the similarity value:

$$\eta = \frac{2|X \cap Y|}{|X| + |Y|} \tag{75}$$

Where X is the area of region of semi-automatic segmentation, Y is the area of region of manual segmentation, and $X \cap Y$ is the overlapped area of two regions. For 3D images, the similarity value can also be acquired using the same equation with volume calculated instead of area.

6.2 Taguchi Analysis

For the proposed segmentation method, several parameters need to be set as constant values, such as α and β for the sigmoid intensity mapping, k and σ for the anisotropic smoothing, and J, K, c for the model matching. However, it is difficult to define an optimal value for each parameter since running experiments on every possible combination of those values to find a suitable one is inefficient and impractical. Here, the

Taguchi method is used to analyze the significance of each variable in the performance of the segmentation process. The Taguchi method is a technique to lay out the experimental plan in logical, economical, and statistical way and is typically used where the output value depends on many inputs [132]. By using the Taguchi experimental design method based on the orthogonal table, Taguchi analysis can quickly reveal the significance of each control parameters with fewer experimental runs and provide tuning trends of control parameters for better performance.

6.2.1 Background of Taguchi Analysis

Taguchi analysis method, based on statistical analysis, was designed by a Japanese engineer Genichi Taguchi in 1950's. The purpose of Taguchi analysis was to improve the performance of a manufacturing system [133] . However, recently, it has been more and more widely applied to diverse areas such as engineering, biotechnology, marketing, and advertising because of its robustness and efficiency [134].

In traditional manufacturing systems, performance or quality of products was measured by some criteria, such as cost of labor, deliverables meeting the specifications, percentage of scrapped parts, percentage of defective products and failure rate etc[100]. However, these criteria are all measurement of the results and cannot provide guidance for a system design. For example, by studying the failure rate, the primary failure module may be displayed, showing the main reason to cause product failure. Nevertheless, when this module is redesigned, other module may become more sensitive to this change and contribute to a higher failure rate. As the result, more changes need to be made afterwards. The process of redesign, test, finding problem and providing a solution will be iterated until no problem is found. Such an approach is a time-consuming and costly process.

Different from the traditional design methods, Taguchi's definition of a robust design is: 'a product whose performance is minimally sensitive to factors causing variability (at the lowest possible cost)' [135]. By systematically choosing certain combinations of variables from the system, the Taguchi method makes it possible to separate the variables' individual effects without having to tediously and uneconomically run the process using all possible combinations of values of those variables [136].

6.2.2 Experimental Design Using Orthogonal Arrays

It turns out that in many applications, the objective function usually depends upon several different control parameters and for each parameter, one can usually focus on two or three different good values, or levels. However, this still leads to a large number of combinations. The Taguchi analysis method provides a method to determine the individual effect of each parameter by experimenting with some of the combinations, i.e. a subset of the parameters' domain. The principles in selecting proper subset are based on two ideas: balance and orthogonality.

6.2.2.1 Balance

Assume that a variable (control parameter) can take n different values (levels), $v_1 \ldots v_n$. , and a total of m experiments will be conducted, then a set of experiments is balanced with respect to the variable v. If: (i) m = kn, for some integer k, and (ii) each of the values, v_i, is tested in exactly k experiments. An experiment is balanced if it is balanced with respect to each variable under investigation [137].

6.2.2.2 Orthogonality

The idea of balance ensures an equal chance to each level of each variable. Similarly, equal attention needs to be paid on combinations of two variables. Assume that there are two variables, A (values: a1…an) and B (values: b1…bm), then the set of experiments is orthogonal if each pair-wise combination of values, (ai, bj) occurs in the same number of trials [137].

For examples, consider an objective function with three variables, each of which can be set at two different values. For convenience, these values are denoted as levels 1 and 2 respectively. A complete investigation requires $2^3 = 8$ total of experimental runs, as shown in Table I.

RUN	A	B	C
1	1	1	1
2	1	1	2
3	1	2	1
4	1	2	2
5	2	1	1

6	2	1	2
7	2	2	1
8	2	2	2

Table I Complete Experimental Runs with Three 2-Level Variables

However, according to the Taguchi orthogonal array, the experiment only requires four runs (Table II). Here, the total number of experiment runs (m) equal to 4, the variable value level (n) equals to 2 and thus k equals to 2 based on the above listed equation: $m = kn$.. Since each variable value is tested twice, the experiment design is balanced. Also for each pair wise combination of values, it occurs once in the experimental runs, thus the experiment design is orthogonal.

RUN	A	B	C
1	1	1	1
2	1	2	2
3	2	1	2
4	2	2	1

Table II Taguchi Orthogonal Array for Three 2-level Variables

The above table is called the L4 array table since it contains four runs. It is specially designed for a problem with up to three 2-level control parameters. If there are only two 2-level control parameters then the first two columns in the table are used for Taguchi analysis and the third column will be ignored. However, if there is an interaction between the two parameters, which means that changing one parameter value may be affect the other one, the third column can be used for the interaction value (Table III).

RUN	A	B	A&B
1	1	1	1
2	1	2	2
3	2	1	2
4	2	2	1

Table III Taguchi Orthogonal Array for Two Interaction Variables

In addition to the L4 array table, there are more tables for different numbers of control parameters with different levels. L9 is for up to four 3-level control parameters and L27 is for up to thirteen 3-level control parameters. How to choose a proper orthogonal array table is based on the following rules [99]:

1) Determine how many control parameters need to be analyzed and how many levels for each parameters.

2) Find the total degree of freedom (DOF) by the following rules:

a) The overall mean always uses 1 DOF.

b) For each control parameter, if the number of level is n, then the DOF is n-1. For example, if the control parameter A has 3 levels, which nA=3, the DOF of A is nA-1=3-1=2.

c) For each two factor interaction, the DOF is the product of their individual DOF, for example, there are two control parameters A, B with nA =3 and nB =3, and there is an interaction between AB, then DOF of AB = (nA -1)(nB -1), the total DOF=1+(nA-1)+(nB -1)+ (nA -1)(nB -1)=9.

3) Select a standard orthogonal array using the following two rules: a) The number of runs of orthogonal array is equal to or greater than the total DOF; b) The orthogonal array shall be able to accommodate the parameter level combinations in the experiment.

The standard orthogonal arrays are shown in Table IV and the information about the runs and levels are provided as well. Using the two factors example above, since the total DOF is 9, L4, L8 cannot be used, while L9 is the best candidate.

Orthogonal Array	**No. Runs**	**Max. Factors**	**Max. of Columns at these Levels**			
			2-Level	**3-Level**	**4-Level**	**5-Level**
L4	4	3	3			
L8	8	7	7			
L9	9	4		4		
L12	12	11	11			
L16	16	15	15			
L'16	16	5			5	
L18	18	8	1	7		
L25	25	6				6
L27	27	13		13		
L32	32	31	31			
L'32	32	10	1		9	
L36	36	23	11	12		
L'36	36	16	3	13		
L50	50	12	1			11
L54	54	26	1	25		
L64	64	63	63			
L'64	64	21			21	
L81	81	40		40		

Table IV Taguchi Orthogonal Arrays

4) Assign control parameters to appropriate columns using the following principles: a) Assign interactions according to the linear graph and interaction table; b) Keep some columns empty if not all columns can be assigned. For example, An L9 orthogonal array is reviewed below, which shows in Table V.

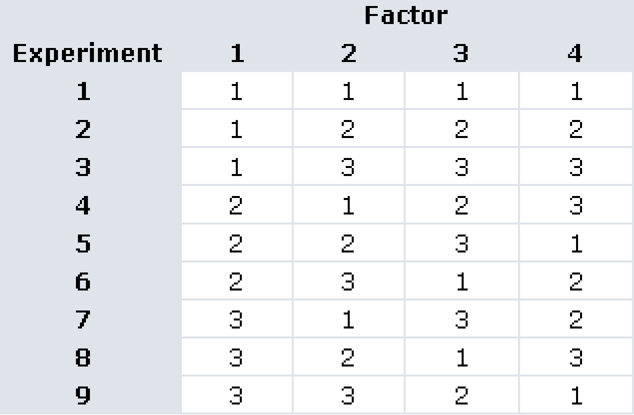

	Factor			
Experiment	1	2	3	4
1	1	1	1	1
2	1	2	2	2
3	1	3	3	3
4	2	1	2	3
5	2	2	3	1
6	2	3	1	2
7	3	1	3	2
8	3	2	1	3
9	3	3	2	1

Table V L9 Orthogonal Array and Linear Graph

The right side is a linear graph, which shows that interaction of first parameter, and second parameter can be put in column 3 or column 4. Thus, applying the rules listed above, an L9 orthogonal table will be utilized, with control parameter A put in column 1, control parameter B put in column 2, the interaction of A and B put in column 3 and the column 4 left blank.

6.2.3 Analyze Performance Using S/N Ratio

After the experimental design has been selected and all the experimental runs have been conducted, the outcome from each experimental run can be used to analyze the significance of each control parameter and determine how to adjust the values/levels for a better performance. To perform the analysis, the Taguchi method uses a statistical measurement of performance called loss function. Traditional design methodologies have a viewpoint that as long as performance value falls in certain specification, it can be considered as good design. Different from that, Taguchi asserted that there is loss when the performance value is not the best one, which can be expressed as a function of deviation from the best performance [99]. The greater the deviation from target value, the greater is the loss. This function is defined as loss function mentioned above. To measure the loss in a single output value x, the loss function can be expressed in equation (76).

$$L(x) = k \cdot (x - t)^2 \tag{76}$$

In which k is the loss coefficient, x is the measured value and t is the target value. For a sample set, an average loss function can be express in equation (77).

$$L_{avg} = k \cdot [\sigma^2 + (\mu - t)^2] \tag{77}$$

In which σ is the standard deviation of the sample and μ is the mean value. The total loss can be express in equation (78).

$$L = n \cdot L_{avg} \tag{78}$$

Where n is the number of samples. In order to minimize the loss function, Taguchi proposed another measurement function called Signal-to-Noise(S/N) ratio, which is borrowed from electrical control theory [138]. The S/N ratio takes both the mean and the variability of outcome into account. It can approve that by maximizing the S/N ratio, loss is minimized, and the performance is tuned to the target value. Depending on the criteria for the performance to be optimized, there are four types of S/N ratio equations [138].

6.2.3.1 The S/N ratio for Smaller-the-better Type of Problem

$$\eta = -10 \log_{10} [\frac{1}{n} \sum (y_i{}^2)] \tag{79}$$

In which y_i is the output value for each experimental run and n is the total experimental runs. This equation is used while the output value is expected to be as small as possible, such as error or failure rate. However, when an ideal value is finite number and its maximum or minimum value is defined, this equation can also be applied by changing the objective equation as

Output’=Output-Ideal value (80)

6.2.3.2 The S/N ratio for Larger-the-better Type of Problem

$$\eta = -10 \log_{10} [\frac{1}{n} \sum (\frac{1}{y_i{}^2})] \tag{81}$$

This equation is used when an output value as large as possible target is expected. It has similar form as smaller-the-better equation while using the invert of output instead.

6.2.3.3 The S/N ratio for Signed-target Type of Problem

$$\eta = -10\log_{10}[\frac{1}{n-1}\sum(y_i - \mu)^2] \tag{82}$$

In which $\mu = \frac{1}{n}\sum_{i=1}^{n} y_i$ is the mean value of all output values. This equation is used when the output can be both positive and negative, such as the rate of change.

6.2.3.4 The S/N ratio for Nominal-the-best Type of Problem

$$\eta = 10\log_{10}[\frac{\mu^2}{\sigma^2}] \tag{83}$$

$$\text{Where } \mu = \frac{1}{n}\sum_{i=1}^{n} y_i \text{ and } \sigma^2 = \frac{1}{n-1}\sum_{i=1}^{n}(y_i - \mu)^2 \,. \tag{84}$$

This equation can be applied to the cases where a specified value is most desired, neither a smaller value nor a large one is desirable. In another word, the outputs have the least variation around the specific value.

Higher S/N ratios are indicative of experimental conditions that will be more robust. In another word, loss function is smaller and performance is closer to the target value. The statistically significant results found in the analysis using S/N ratios will show the significance of each parameters and reveal that how to tune these parameters to achieve better performance.

6.2.4 Significance and Tuning Trend of Parameters

First, a trend table can be obtained by picking the levels with highest S/N ratio, and then the distance table is calculated using the following equation (85).

$$\text{Distance} = (\max(S/N) - \min(S/N) \qquad (85)$$

Then the significance index table, in which the significance of each parameter is sorted, is calculated by normalizing the distance table using the following equation (86).

$$\text{Index} = \text{Distance} / \text{Maximum Distance} \qquad (86)$$

6.2.5 Apply Taguchi Method to Proposed Segmentation Method

For the proposed segmentation method, there are seven control parameters (factors), in which α and β indicate sigmoid intensity mapping, k and σ indicate anisotropic smoothing, and J, K, c indicate model matching. Each parameter with three levels was assigned a number: 1: lowest value; 2: mean value; and 3: highest value. Since there are no interactions among them, the total DOF is equal to $1+(3-1)\times 7=15$. From Table IV, it is clear that the L27 orthogonal table is the best choice. L27 is designed for up to thirteen three-level parameters (Table VI).

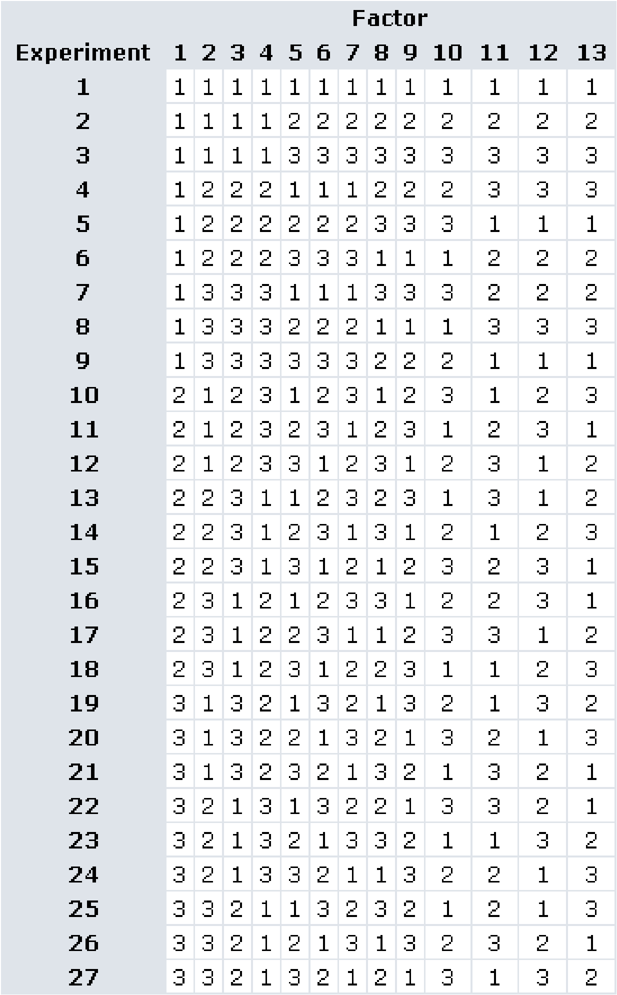

	Factor												
Experiment	**1**	**2**	**3**	**4**	**5**	**6**	**7**	**8**	**9**	**10**	**11**	**12**	**13**
1	1	1	1	1	1	1	1	1	1	1	1	1	1
2	1	1	1	1	2	2	2	2	2	2	2	2	2
3	1	1	1	1	3	3	3	3	3	3	3	3	3
4	1	2	2	2	1	1	1	2	2	2	3	3	3
5	1	2	2	2	2	2	2	3	3	3	1	1	1
6	1	2	2	2	3	3	3	1	1	1	2	2	2
7	1	3	3	3	1	1	1	3	3	3	2	2	2
8	1	3	3	3	2	2	2	1	1	1	3	3	3
9	1	3	3	3	3	3	3	2	2	2	1	1	1
10	2	1	2	3	1	2	3	1	2	3	1	2	3
11	2	1	2	3	2	3	1	2	3	1	2	3	1
12	2	1	2	3	3	1	2	3	1	2	3	1	2
13	2	2	3	1	1	2	3	2	3	1	3	1	2
14	2	2	3	1	2	3	1	3	1	2	1	2	3
15	2	2	3	1	3	1	2	1	2	3	2	3	1
16	2	3	1	2	1	2	3	3	1	2	2	3	1
17	2	3	1	2	2	3	1	1	2	3	3	1	2
18	2	3	1	2	3	1	2	2	3	1	1	2	3
19	3	1	3	2	1	3	2	1	3	2	1	3	2
20	3	1	3	2	2	1	3	2	1	3	2	1	3
21	3	1	3	2	3	2	1	3	2	1	3	2	1
22	3	2	1	3	1	3	2	2	1	3	3	2	1
23	3	2	1	3	2	1	3	3	2	1	1	3	2
24	3	2	1	3	3	2	1	1	3	2	2	1	3
25	3	3	2	1	1	3	2	3	2	1	2	1	3
26	3	3	2	1	2	1	3	1	3	2	3	2	1
27	3	3	2	1	3	2	1	2	1	3	1	3	2

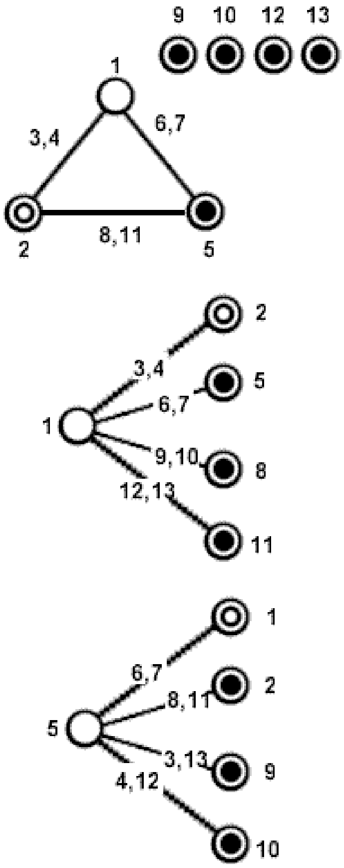

Table VI L27 Orthogonal Array and Linear Graph

The interaction of factors is shown in the right-side linear graph, and the independent factors can be .put on column 1,2,5,9,10,12,13, shown as Table VII.

Experimental Runs	Sigmoid Mapping		Anisotropic Filter		Model Matching		
	α	β	k	σ	J	K	c
1	1	1	1	1	1	1	1
2	1	1	2	2	2	2	2
3	1	1	3	3	3	3	3
4	1	2	1	2	2	3	3
5	1	2	2	3	3	1	1
6	1	2	3	1	1	2	2
7	1	3	1	3	3	2	2
8	1	3	2	1	1	3	3
9	1	3	3	2	2	1	1
10	2	1	1	2	3	2	3
11	2	1	2	3	1	3	1
12	2	1	3	1	2	1	2
13	2	2	1	3	1	1	2
14	2	2	2	1	2	2	3
15	2	2	3	2	3	3	1
16	2	3	1	1	2	3	1
17	2	3	2	2	3	1	2
18	2	3	3	3	1	2	3
19	3	1	1	3	2	3	2
20	3	1	2	1	3	1	3
21	3	1	3	2	1	2	1
22	3	2	1	1	3	2	1
23	3	2	2	2	1	3	2
24	3	2	3	3	2	1	3
25	3	3	1	2	1	1	3
26	3	3	2	3	2	2	1
27	3	3	3	1	3	3	1

Table VII Orthogonal Array for Seven 3-level Control Parameters

The output of each experimental run is calculated using the following equation (87).

$$\text{Output}=1-\text{Similarity} \tag{87}$$

Since the objective is to minimize the outcome, equation (79) representing the smaller-the-better type of problem is used to calculation the S/N ratio.

In this chapter, a performance evaluation method is developed for proposed semi-automatic segmentation method. The performance is indicated by the similarity value of semi-automatic and manual segmentation results, which is calculated by the Dice coefficient equation. In addition, Taguchi analysis is applied to reveal the significance of each segmentation parameter quickly with fewer experimental runs. Taguchi analysis is very efficient when the output depends on many control parameters. Moreover, it can provide tuning trend of each parameter for better segmentation performance. For 2D and 3D segmentation of female pelvic floor structures, Taguchi orthogonal table L27 is selected to design experimental runs based on the DOF value and all seven segmentation (control) parameters are placed in independent variable columns. The output of each experimental run is 1-similarity. Since the objective is to maximize the similarity value of semi-automatic segmentation and manual segmentation, an equation representing smaller-the better type of problem is used to calculate the S/N ratio.

CHAPTER VII

TESTING RESULTS

7.1 Segmentation Tests

In this study, the proposed segmentation method is tested on both 2D images and 3D images. Although many structures of the normal female pelvic floor can be segmented by applying the proposed methods, the levator ani muscle and obturator muscles were chosen as examples for 2D and 3D segmentation, respectively, because of the following factors.

1) Levator ani and obturator muscles are important for SUI and POP. Previous research has confirmed the association with abnormalities of the levator ani muscle and prolapse. Laxity of the levator ani muscle can lead to the widening of the

genital hiatus, which is a potential initiation of POP [139]. In general, the damage degree of the muscles can be evaluated with quantitative measurement of geometric shapes [140].

2) Levator ani and obturator muscles have complex shapes in MR images, which make it difficult to segment the images manually (Figure 46(a)).

3) Levator ani and obturator muscles have low contrast on MR images, making it difficult to segment the images by model free methods. Moreover, they have a similar intensity value to the surrounding structures and the borders of structure cannot be clearly identified. In practical study, the model free methods are usually misleading in such situations. For example, since the rectum and the levator ani muscle have similar intensity values, the methods of thresholding and contouring cannot separate these two structures effectively. In Figure 46 (b), with intensity based thresholding, the border of levator ani muscle is fused into the border of rectum muscular wall, also, there are several black islands in the region of levator ani muscle which cannot moved by adjusting threshold values. In Figure 46 (c), the green contour is the result of contour-based segmentation and the segmented region obviously contains part of rectum. For comparing, correct border of levator ani muscle with manual segmentation is shown in yellow contour.

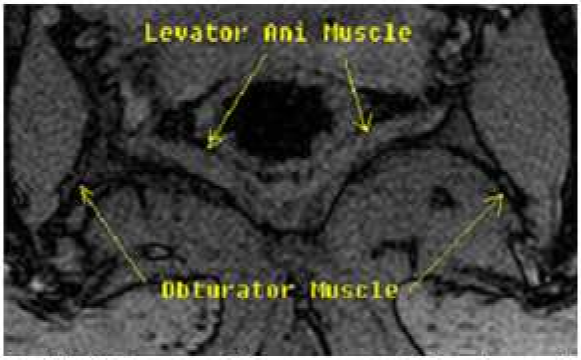

(a) Original MR Image of Levator Ani Muscles and Obturator Muscles

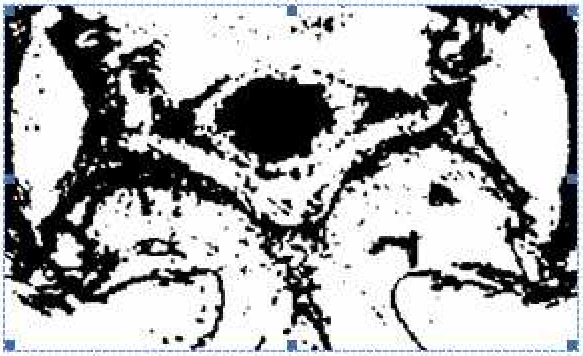

(b) Intensity Based Segmentation (Thresholding)

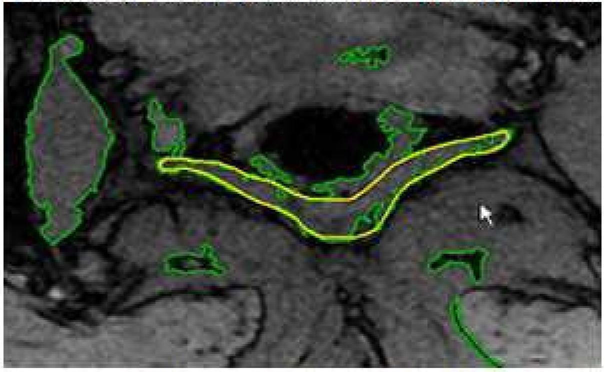

(c) Contour Based Segmentation Cannot Correctly Find the Border of Levator Ani Muscle
(The Yellow Contour Is Done by Manual Segmentation)

Figure 46 Example of Ineffective Model Free Methods

7.2 2D Segmentation on the Levator Ani Muscle

To semi-automatically segment the levator ani muscle, first, a statistical model was built based on the training set images; secondly, the local image feature map was generated by applying a sequence of filters on unseen image data. The feature map and statistical model were taken as the inputs for model matching. Finally, the segmentation results were evaluated using the Dice coefficient equation, Taguchi analysis was applied to tune the control parameters to improve performance. Details of each step of segmentation are given in the following subsections.

7.2.1 Build Statistical Model

From an MRI database at the Cleveland Clinic, 24 examples of MRI slices were selected for the training set. The selected slices were confirmed to contain normal pelvic floor structures and cover typical shape variations of the levator ani muscle. Each slice was manually segmented by live wire methods to generate a binary mask, which separates the structure's shape from the background.

First, the region of interest (ROI) was cropped based on the binary masks. The image only contains a structure of levator ani muscle with the dimension of 160 by 160 pixels. All of the cropped images were aligned using the method of centered affine transformation, which described in details in Chapter V. The results of alignment are shown in Figure 47.

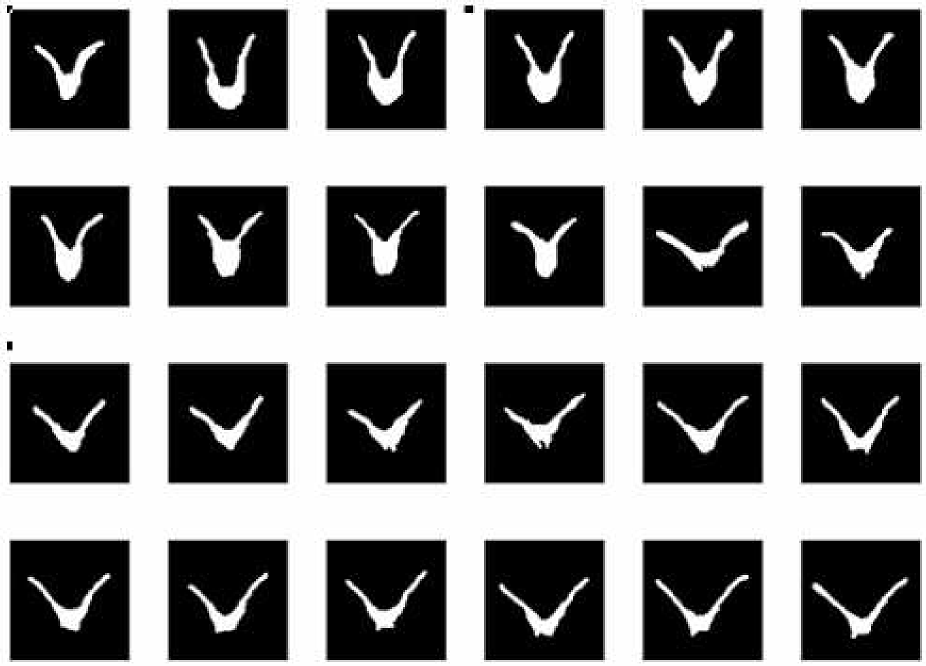

Figure 47 Examples of Aligned Levator Ani Muscle

In the second place, signed distance maps were calculated based on the aligned shapes (Figure 48). The results were 2D matrixes 160 by 160 pixels large. Each element of the matrix belongs to the float type data that denotes the distance of each pixel to the nearest shape border. Since the digital images can only be shown with integer grayscale intensity, ranging from 0 to 255, the float type data was converted to integer type data.

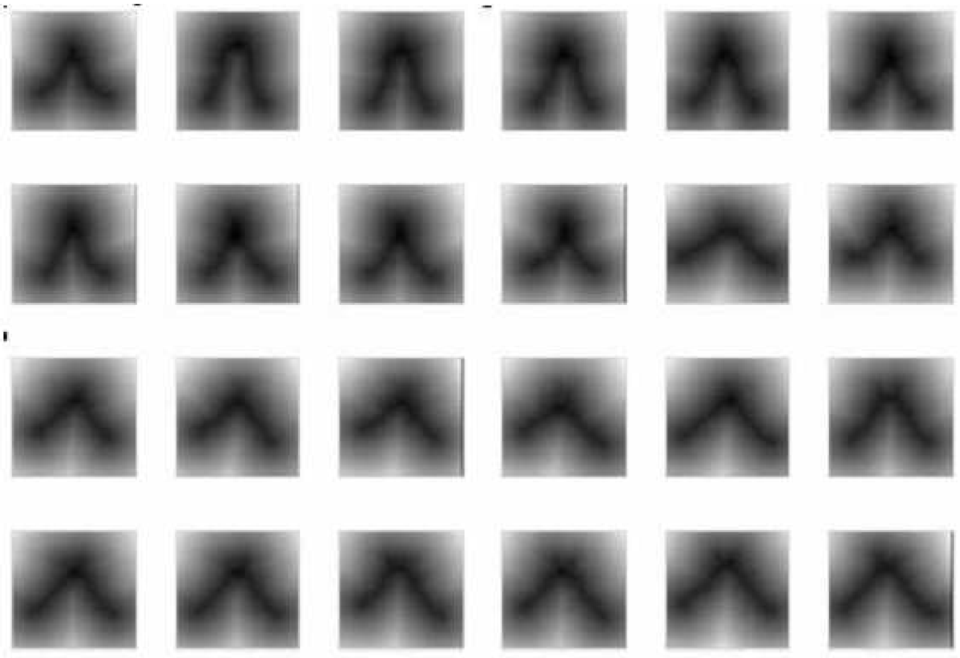

Figure 48 A Signed Distance Map of Levator Ani Muscle

Once again, PCA was applied to the distance maps to generate mean shape and shape variation models. Although 24 principle components were generated in total, to describe the variation model in a compact form, only the five most significant principle components were selected with reference to their sorted eigenvalues (Figure 49).

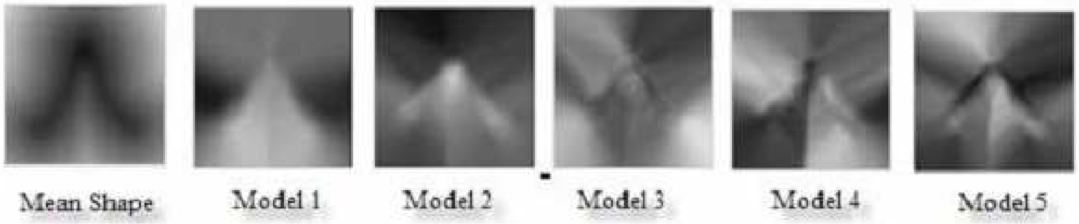

Mean Shape Model 1 Model 2 Model 3 Model 4 Model 5

Figure 49 A Signed Distance Map of Mean Shape and Shape Variation Model

7.2.2 Generate Feature Map of Unseen Data

The unseen images were selected from the same MRI database. Local image feature maps were obtained by applying the sigmoid window and level filter, the anisotropic smoothing filter, the gradient filter, and the normalization filter on unseen images sequentially (Figure 50). Proper values need to be assigned to control parameters of those filters. The topic of how to choose the proper values will be covered in a later section on Taguchi analysis (Section 7.2.4).

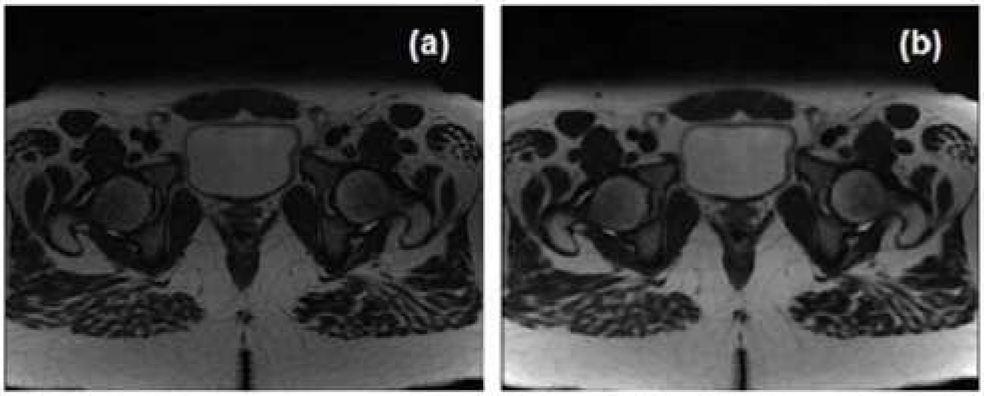

(a) Original Image

(b) Window/Level and Anisotropic Smoothing

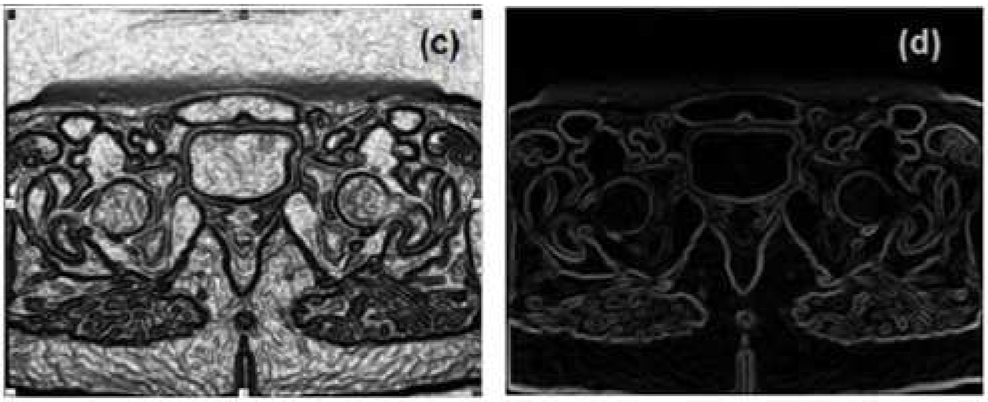

(c) Gradient Magnitude

(d) Normalization

Figure 50 Processing of Unseen Data

7.2.3 Model Matching

By imposing an evolutionary contour onto unseen images, the statistical model and feature map guide the expansion and evolution of contour. Local image feature map attracts the contour to the border of the structure while the statistical model keeps a reasonable shape of contour by updating the best-fit shape parameters and transformation parameters. In Figure 51, (a) is the initial guess of the levator muscle in unseen data and (b) is the final best-fit results. Figure (c) is the overlap of segmented result (red color region) with unseen image.

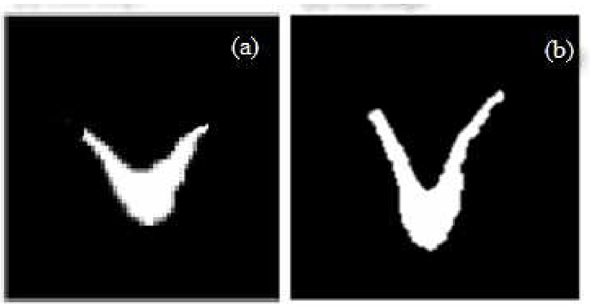

(a) Initial Shape (b) Final Shape

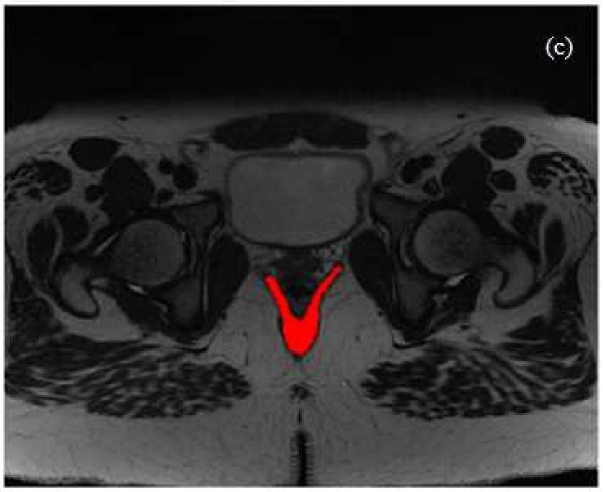

(c) Model Search Results (500 Iterations)

Figure 51 Model Matching Method for Levator Ani Muscle

7.2.4 Taguchi Analysis

For the proposed segmentation, there are seven parameters (control factors) that need to be predefined, in which α and β are for the sigmoid intensity mapping, k and σ are for anisotropic smoothing, and J, K, c are for the model matching. In order to determine which control parameter is significant to the performance of segmentation and how to adjust them to achieve better result, a Taguchi analysis is performed and investigated in this study.

First, the table containing the list of control factors was established, defining the value range and levels for each parameter. In the study, three levels were used for each parameter with level 1 standing for the lowest value, level 2 standing for the mean value and level 3 standing for the highest value (Table VIII).

Control Factor	Value Range	Level 1	Level 2	Level 3
α	[0.5 2]	0.5	1.25	2
β	[-2 2]	-2	0	2
σ	[0.1 0.5]	0.1	0.3	0.5
k	[1 3]	1	2	3
J	[0.1 0.9]	0.1	0.5	0.9
K	[0.1 0.9]	0.1	0.5	0.9
c	[0.1 0.9]	0.1	0.5	0.9

Table VIII Taguchi Control Factors Table

According to the previous section 6.2.2.2, the DOF was calculated as 1+7*(3-1) =15. Therefore, the L27 orthogonal array was used to design experimental runs here. For each experimental run, the outcome value was calculated as 1-similarity (based on the Dice coefficient equation), which means that the smaller the outcome value, the more accuracy the segmentation result. Results are shown in Table IX.

Experimental Runs	Sigmoid Mapping		Anisotropic Filter		Model Matching			Outcome
	α	β	σ	k	J	K	c	
1	1	1	1	1	1	1	1	0.1472
2	1	1	2	2	2	2	2	0.0469
3	1	1	3	3	3	3	3	0.1164
4	1	2	1	2	2	3	3	0.0927
5	1	2	2	3	3	1	1	0.1532
6	1	2	3	1	1	2	2	0.0702
7	1	3	1	3	3	2	2	0.0766
8	1	3	2	1	1	3	3	0.1678
9	1	3	3	2	2	1	1	0.1046
10	2	1	1	2	3	2	3	0.0911
11	2	1	2	3	1	3	1	0.1378
12	2	1	3	1	2	1	2	0.0899
13	2	2	1	3	1	1	2	0.1278
14	2	2	2	1	2	2	3	0.0556
15	2	2	3	2	3	3	1	0.1303
16	2	3	1	1	2	3	1	0.0941
17	2	3	2	2	3	1	2	0.1211
18	2	3	3	3	1	2	3	0.0894
19	3	1	1	3	2	3	2	0.0923
20	3	1	2	1	3	1	3	0.1344
21	3	1	3	2	1	2	1	0.0864
22	3	2	1	1	3	2	1	0.0897
23	3	2	2	2	1	3	2	0.1258
24	3	2	3	3	2	1	3	0.0977
25	3	3	1	2	1	1	3	0.1289
26	3	3	2	3	2	2	2	0.0458
27	3	3	3	1	3	3	1	0.1123

Table IX Taguchi L27 Orthogonal Table

Since the design objective is to minimize the output value, the smaller-the-better equation was applied here to calculate the S/N value (Table X).

S/N	Sigmoid Mapping		Anisotropic Filter		Model Matching		
	α	β	σ	k	J	K	c
Lower the Better	18.77	19.26	19.42	18.94	18.14	18.1	18.44
Mean the Better	19.4	19.26	18.52	19.38	21.62	22.55	20.59
Higher the Better	19.6	19.22	19.9	19.42	18.7	18.33	18.98

Table X S/N Table

Based on the above s/n table, the significance index and the trend for each parameter were acquired (Table XI).

	Sigmoid Mapping		Anisotropic Filter		Model Matching		
	α	β	σ	k	J	K	c
Max-Min	0.822	0.04	1.381	0.481	3.479	4.454	2.157
Significance Index	0.185	0.009	0.31	0.108	0.781	1	0.484
Trend	HB	MB	HB	HB	MB	MB	MB

Table XI Significance Index and Trend

From the significance index table above, it can be concluded that the weight of the shape model is more important than that of the feature map for model-based segmentation. In addition, the weight cannot be too large or too small. It must be reasonable, because if the weight is too large, the segmentation method will omit the image features; and if the weight is too small, the shape model will have the least influence on the segmentation, resulting in the misleading results similar to model-free methods. The best weight ratio for the shape model and feature map here is 1:1. Beside the above considerations, the propagation step/force factor c is also important, and the mean value is the best choice. Enlarging, shrinking the contour too fast, or too slow all lead to a lower segmentation performance. Anisotropic smoothing for unseen data has certain influence on segmentation performance too, which suggests that σ should be carefully chosen to reduce noise while keeping the edge features of the structure's border. Compared to model matching parameters, the intensity mapping parameters are less significant. In the last, according to the trend table, the following values should be assigned to the parameters: α =2 and β=0 are for sigmoid intensity mapping, k=3 and σ=0.5 are for anisotropic smoothing and J=0.5, K=0.5, c=0.5 are for model matching. By running the experiment with the above parameter values, the output turns out to be 0.0414 (the dice coefficient is 1-0.0414=0.9586), which is better than the lowest value in experimental runs.

7.3 3D Segmentation on Obturator Muscles

The proposed segmentation method can be extended from 2D to 3D images in a simple way. Here the obturator muscle was used as an example and the execution steps are similar to that of 2D segmentation.

7.3.1 Build Statistical Model

Because obturator muscles have less shape variations than the levator ani muscle, only 8 instead of 24 samples were chosen from the MR volume images and were manually segmented using Amira software to generate 3D binary masks. The region of interest was first cropped and the 3D shapes were aligned using the same centered affine transformation method. The isosurfaces of aligned shapes are shown in Figure 52.

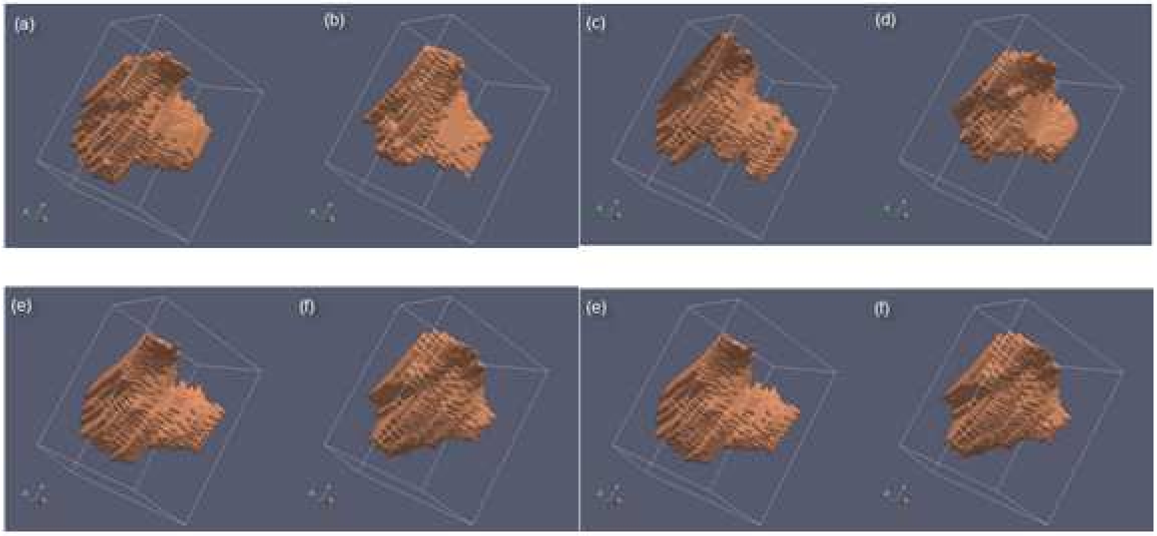

Figure 52 Isosurface of Aligned Shapes of Obturator Muscles from (a) to (h)

The 3D distance maps were then calculated based on 3D binary images. The following images show the 2D intersection of those 3D distance maps, in which all intensity values were converted from float to integer and are normalized to the range from 0 to 255 (Figure 53).

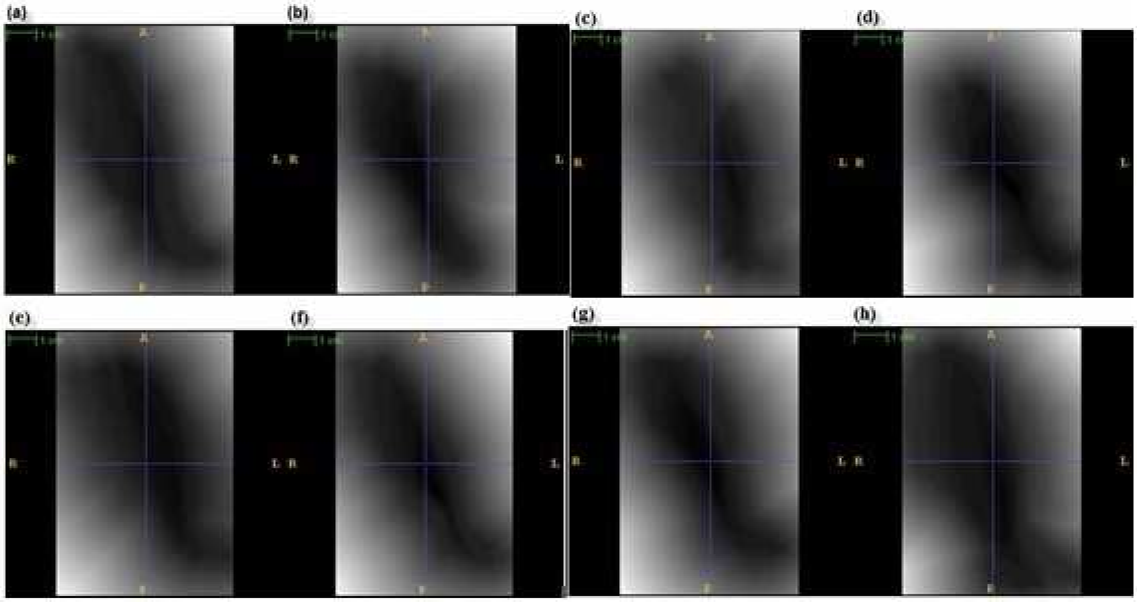

Figure 53 3D Distance Map of Obturator Muscles from (a) to (h)

Based on the 3D distance maps, PCA was applied and the mean shape and shape variation model was obtained. The most significant principle components were selected here to build the compact variation model (Figure 54).

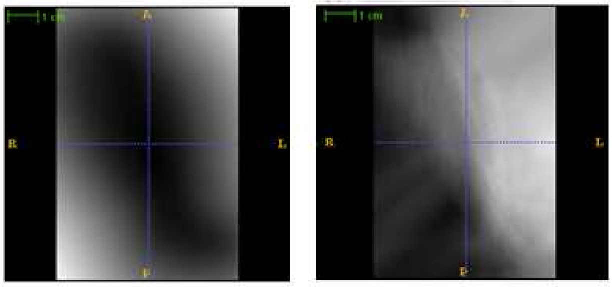

(a) Mean Shape

(b) Variation Model (1071470)

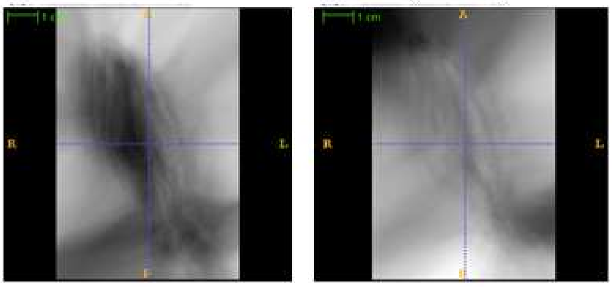

(c) Variation Model (472119)

(c) Variation Model (308772)

Figure 54 Shape Model of Obturator Muscles Sample from (a) to (d)

7.3.2 Generate Feature Map of Unseen Data

Similar to the 2D images, the 3D volume images were processed by the same sequences of the filters to get a local image feature map to be used as the inputs for the model-based segmentation. After the sigmoid intensity mapping, the contrast of obturator muscles was enhanced, and with the anisotropic smooth filtering, a clear edge of the structure was acquired by calculating its gradient magnitude (Figure 55).

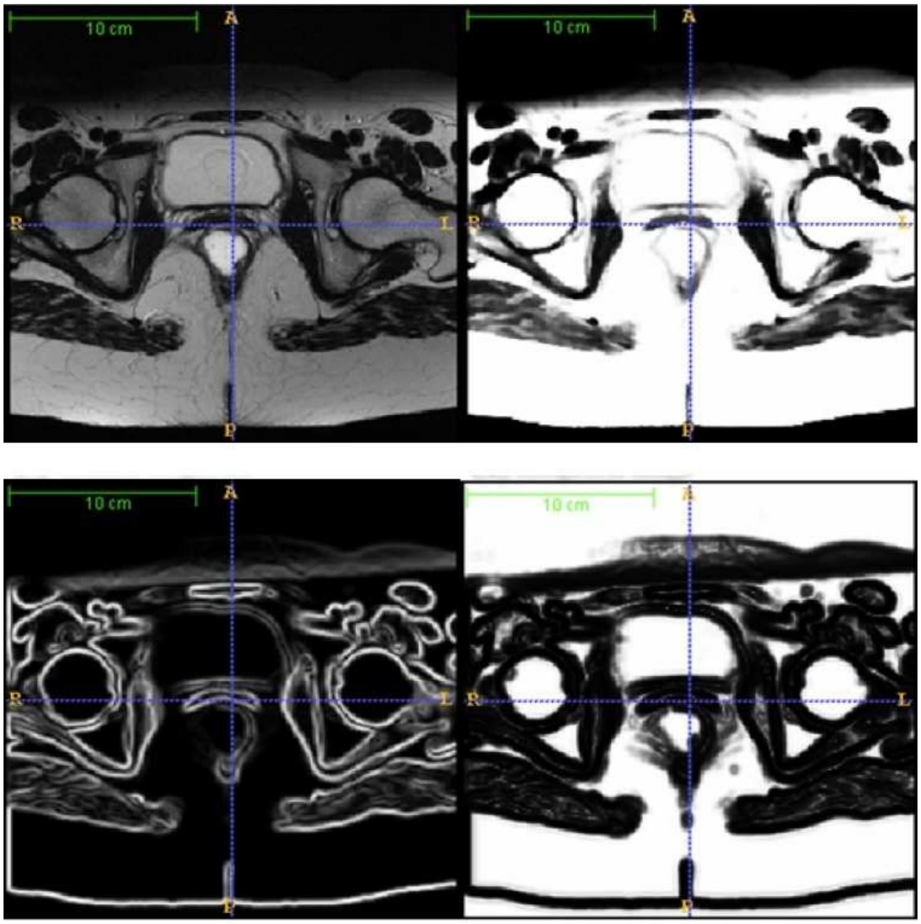

Figure 55 Feature Map of Unseen Data

7.3.3 Model Matching Results

The initial shape model and final shape model are shown in Figure 56 (a) and (b). To demonstrate the difference, the overlapped 3D shapes are shown in Figure 56 (c), and the overlapped image of original image and 3D segmented result is shown in Figure 57.

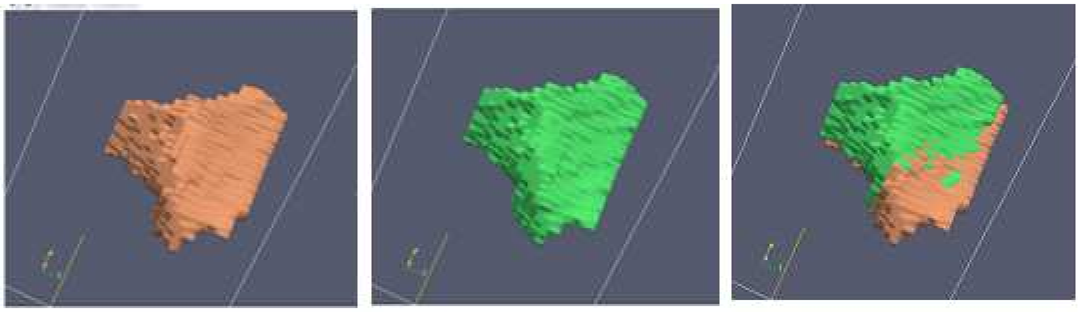

(a) Initial Guess (b) Final Shape (c) Overlapped 3D shape

Figure 56 Model Matching for Obturator Muscles

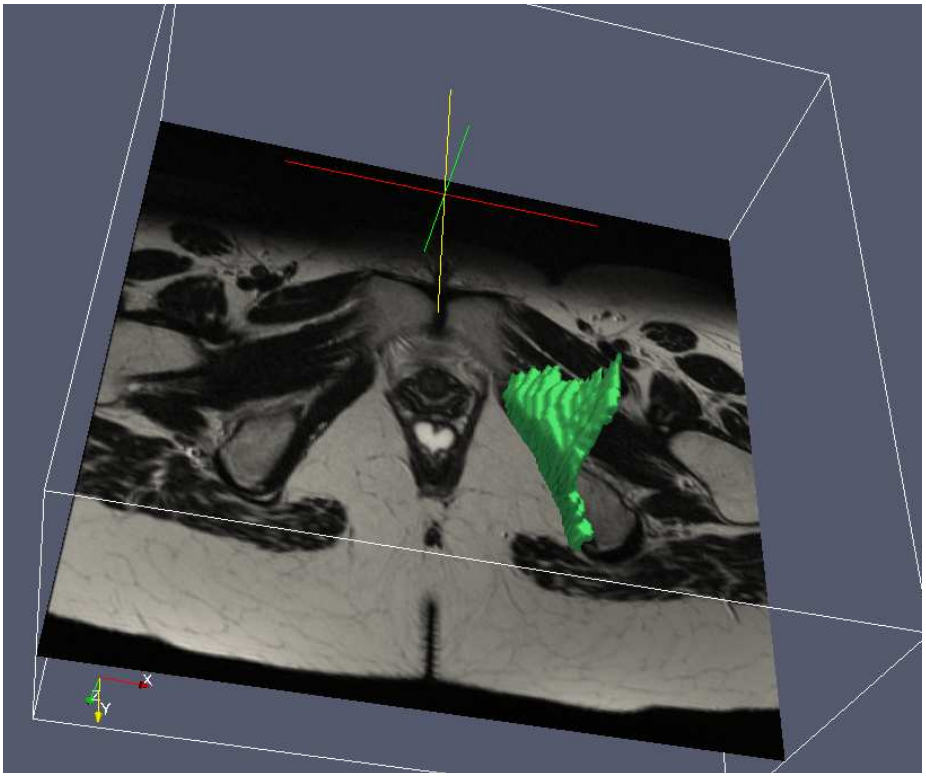

Figure 57 Overlap of MR Image and Segmentation Result of Obturator Muscles

7.3.4 Taguchi Analysis

Since the same control parameters were used for the 3D segmentation, the Taguchi control factor table and orthogonal table is same as the tables used for 2D segmentation. The specific results for the experimental runs are shown in Table XII.

Experimental Runs	Sigmoid Mapping		Anisotropic Filter		Model Matching			Outcome
	α	β	σ	k	J	K	c	
1	1	1	1	1	1	1	1	0.2072
2	1	1	2	2	2	2	2	0.0494
3	1	1	3	3	3	3	3	0.1564
4	1	2	1	2	2	3	3	0.0827
5	1	2	2	3	3	1	1	0.1732
6	1	2	3	1	1	2	2	0.0632
7	1	3	1	3	3	2	2	0.086
8	1	3	2	1	1	3	3	0.1278
9	1	3	3	2	2	1	1	0.0934
10	2	1	1	2	3	2	3	0.0998
11	2	1	2	3	1	3	1	0.1059
12	2	1	3	1	2	1	2	0.0911
13	2	2	1	3	1	1	2	0.1507
14	2	2	2	1	2	2	3	0.0822
15	2	2	3	2	3	3	1	0.1554
16	2	3	1	1	2	3	1	0.0883
17	2	3	2	2	3	1	2	0.1421
18	2	3	3	3	1	2	3	0.0957
19	3	1	1	3	2	3	2	0.0732
20	3	1	2	1	3	1	3	0.1372
21	3	1	3	2	1	2	1	0.0754
22	3	2	1	1	3	2	1	0.0799
23	3	2	2	2	1	3	2	0.1358
24	3	2	3	3	2	1	3	0.0812
25	3	3	1	2	1	1	3	0.1472
26	3	3	2	3	2	2	2	0.0559
27	3	3	3	1	3	3	1	0.1075

Table XII Taguchi L27 Orthogonal Table

The S/N value and the significance index and trend for each control factor are shown in Table XIII and Table XIV.

S/N	Sigmoid Mapping		Anisotropic Filter		Model Matching		
	α	β	σ	k	J	K	c
Lower the Better	17.99	18.43	18.37	18.32	17.72	16.99	17.83
Mean the Better	18.74	18.54	18.49	19.64	22.07	22.15	19.91
Higher the Better	19.65	19.29	19.43	18.39	17.7	18.53	18.73

Table XIII S/N Table

	Sigmoid Mapping		Anisotropic Filter		Model Matching		
	α	β	Σ	k	J	K	c
Max-Min	1.661	0.861	1.062	1.321	4.368	5.156	2.08
Significance Index	0.322	0.167	0.206	0.256	0.847	1	0.403
Trend	HB	HB	HB	MB	MB	MB	MB

Table XIV Significance Index and Trend

Some of the same control parameters have significance and trends in 3D segmentation of obturator muscles, as is 2D segmentation of the levator ani muscle. These include J, K, and c for model searching. However, the significance of intensity mapping is become greater for 3D segmentation of obturator muscles. This could because obturator muscles have higher contrast than the levator ani muscle in MR imaging so obturator muscles can have clearer borders using an intensive mapping operation. Besides this, the significance value of the weight for the feature map of the 3D segmentation is increased compared to 2D segmentation, suggesting that for a better quality image or higher contrast structures, segmentation should rely more on the local image features.

Finally, based on the trend table, the following values should be assigned to the following parameters: α =2 and β=2 for sigmoid intensity mapping, k=3 and σ=0.3 for anisotropic smoothing, and J=0.5, K=0.5, c=0.5 for model matching. By running the experiment with the above parameter values, the output turns out to be 0.0455 (1-Dice Coefficient), once again, a little bit better than the lowest value in experimental runs.

CHAPTER VIII

CONCLUSIONS AND FUTURE WORK

8.1 Conclusions

In this dissertation, a semi-automatic segmentation method based on a statistical shape model is proposed to reduce the time spent building a VR model of the normal female pelvic floor. This method can be applied to the case of pelvic floor structures with low contrast in MR images, or the case of pelvic floor structures having similar intensity values to surrounding tissues. In both above-mentioned cases, model-free segmentation methods such as thresholding, clustering and contouring are not effective. This method can also be used for various medical applications of segmentation of other organs and structures with relatively fixed shapes in medical images, such as bones, brain, kidney, and lungs. In general, the proposed method offered the following features:

1) The proposed model-based methods can be performed on both 2D and 3D images without modifying the pipeline. All of the components of the segmentation pipeline (including modeling building and model matching) are designed to accept both 2D and 3D images, thus the method can be easily applied with dimensional increase or decrease for the images.

2) A special filtering sequence is designed to extract local image features from the MR scans. Specifically, a sigmoid nonlinear intensity mapping filter is used to increase the contrast of target structures, an anisotropic smoothing filter is applied to reduce noise signal while maintaining the features of border of structures, and the gradient magnitude is calculated by a 2D or 3D Sobel operator to separate the edge of structures from the image background. The resulting feature maps together with a statistical shape model are used as the inputs for the model matching (segmentation) to guide the evolving of contour or surface.

3) An easy and robust method is developed to extract shape information from the training samples. Usually, the statistical shape model is built from a set of corresponding points of the target shape (landmarks). It is time-consuming to manually label all of the corresponding points, and is impossible for complicated 3D shapes. The proposed segmentation method utilizes the distance maps instead of the landmarks to calculate the shape correspondence and aligns those shapes automatically via the method

of centered affine transformation, which greatly speeds the process of building the statistical model and increases accuracy.

4) A performance evaluation standard for image segmentation is proposed. Specifically, the Dice coefficient is used to calculate the similarity value for semi-automatic segmentation and manual segmentation. Compared to the visual evaluation, the proposed quantitative measurement is more objective and easier to perform.

5) For the proposed method, seven control parameters are involved in the segmentation pipeline and each parameter has its own value range. Different values can lead to different segmentation performance. However, running experiments on every possible combination to find a suitable one is extremely inefficient. A Taguchi analysis method is applied in this study to analyze the segmentation results. By using the Taguchi orthogonal table and the according S/N equation based on the objective setup, the parameter that is most significant to the outcome can be shown quickly and adjusted to achieve improved segmentation performance.

The proposed method was tested for segmentation of image of 2D levator ani muscle and 3D image of obturator muscles. Both provided the satisfying results. By running a Taguchi analysis on both 2D and 3D image, it is concluded that the model matching parameters, i.e. the weight for feature map, the weight for statistical shape model and propagation step/force, are the most significant factors influencing the segmentation performance. The best value of weights for shape model and feature map is 0.5 in this example.

For the segmentation of obturator muscles, control factors of sigmoid intensity mapping are more important than factors of anisotropic smoothing. On the contrary, for the levator ani muscle, control factors of anisotropic smoothing are more important than factors of sigmoid intensity mapping. This is because the obturator muscle has higher intensity contrast value in the images. With proper sigmoid intensity mapping, the clearer border of the structure of obturator muscles can be obtained, and segmentation performance can be improved.

On the other hand, the levator ani muscle has lower contrast compared to obturator muscles. Therefore, noise reduction and proper edge-preserving smoothing is more critical. For both cases, segmentation performance can be improved using the suggested tuning trend for each parameter with Taguchi analysis.

8.2 Future Work

8.2.1 Performance Improvement

Although the proposed method achieves good results for segmentation of the levator ani and obturator muscles, there is a lot of room to improve the segmentation performance.

1) During the statistical model building process, more samples of target structures can be selected, and therefore more shape variations can be covered in the training set. As a result, more principle components can be applied in the shape variation model. However, efficiency and performance need to be balanced carefully. It is true that the more complicated the shape model, the more robust for the model built. It also requires extensive computation for the model searching.

2) In local image feature extraction, either modification of the existing filters or applying more filters in the sequence may improve the performance of segmentation. For example, some other nonlinear functions can be used in intensity mapping to enhance the contrast of target structures. A wavelet filter could be used for noise reduction and smoothing [141]. Morphological operations, such as opening, closing, dilution and erosion, can be used for repairing the extracted edge when small parts of the border is missing or blurred with other tissues [142].

3) In model searching, gradient magnitude of the feature map is used to attract the contour or surface to the structure borders. Although the gradient direction (angle) can also be acquired in the feature map, it is not used in the current model matching pipeline. However, if one can utilize this information to guide evaluation of the contour or surface, it may speed model searching and improve segmentation performance. In addition, improvement could be done with an optimization algorithm, which needs to be balanced by efficiency and performance. Although the 1+1 ES performs well on the

test examples, it is worth trying and comparing more optimization methods based on other examples to find the best candidate.

8.2.2 Automatically Build VR Model of Female Pelvic Floor

The objective of this research is to develop a semi-automatic segmentation method to speed up building a VR model of female pelvic floor. However, it is also possible to build a VR model from MR images automatically based on the developed technique and other segmentation algorithms. The proposed segmentation method could be used for any pelvic floor structures without large shape variations such as pelvic bones and urethra, and a combined shape model of those structures could be developed with additional parameters of distance and angles of structures. Such a combined model is expected to result in segmentation results that are more robust since missing or blurred shape information in one structure could be best estimated by the parameters of other reliable structures. Besides, such a model will be more efficient since it matches all of the structures to the image simultaneously, not just one by one (Figure 58).

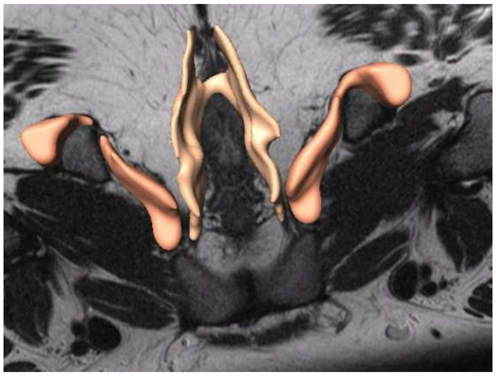

Figure 58 A Combined Model of the Levator Ani Muscle and Obturator Muscles

Some structures of the pelvic floor have large shape variations and model-based segmentation cannot be applied, such as bladders and vessels. However, since they have high contrast on MR images, model free methods can be applied to these structures for a semi-automatic segmentation. In our preliminary study, a 3D region growing algorithm achieved a satisfying result for segmentation of vessels, and a contouring algorithm worked well for segmentation of bladder (Figure 59 and Figure 60).

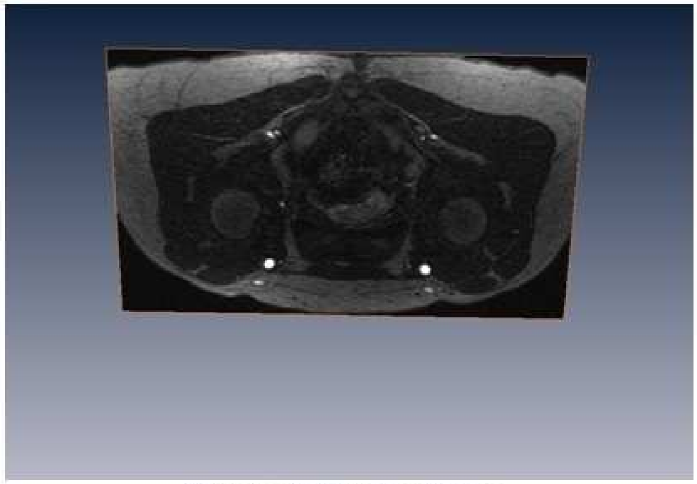

(a) Original MRI Images of Vessels

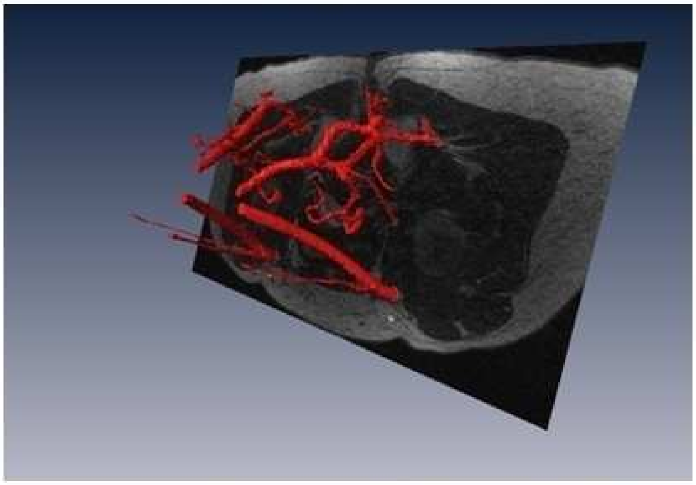

(b) Segmentation of Vessels based on 3D Region Growing

Figure 59   3D Segmentation of the Vessel

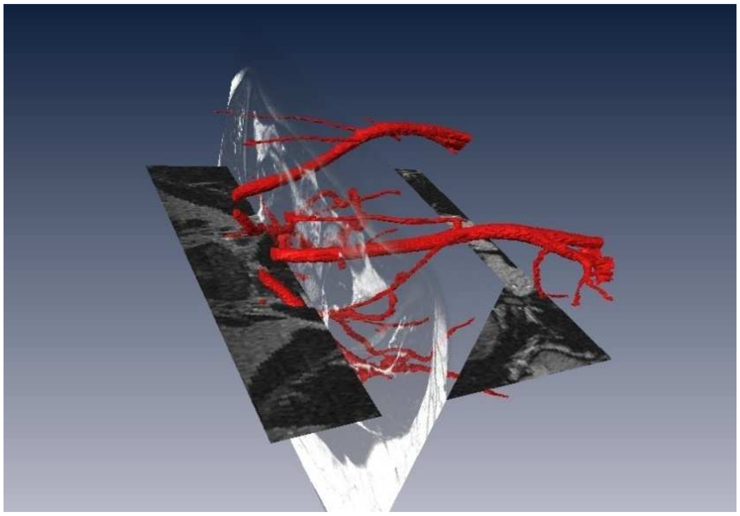

Figure 60 Segmentation Result with Axial and Coronal MRI Scans

As a conclusion, proposed model-based segmentation method can be used to segment female pelvic floor structures and build 3D and VR models. Compared to conventional manual segmentation, it is more efficient. The model is based on statistical analysis of shapes of the target structure, which makes the segmentation robust and reliable for low contrast structures in medical images. Furthermore, using Taguchi analysis can quickly reveal the significance of segmentation parameters with fewer experimental runs, which is very useful when many parameters are involved in the segmentation pipeline. Future studies should focus on enhancing the segmentation performance by improving current modeling pipeline and model matching algorithms, or developing combined shape models.

REFERENCE

1. Hu, T.W., *Impact of urinary incontinence on healthcare costs.* Journal of the American Geriatrics Society, 1990. **38**(3): p. 292-295.

2. Drutz, H.P. and M. Alarab, *Pelvic organ prolapse: demographics and future growth prospects.* International Urogynecology Journal, 2006. **17**: p. 6-9.

3. Thom, D., Variation in estimates of urinary incontinence prevalence in the community: effects of differences in definition, population characteristics, and study type. Journal of the American Geriatrics Society, 1998. **46**: p. 473-480.

4. Sutherland, S. and H. Goldman, *Treatment options for female urinary incontinence.* Medical Clinics of North America, 2004. **88**(2): p. 345-366.

5. Ortiz, O.C., *Stress urinary incontinence in the gynecological practice.* International Journal of Gynecology & Obstetrics, 2004. **86**: p. 6-16.

6. Carlson, K.J., S.A. Eisenstat, and T.D. Ziporyn, *The Harvard Guide to Women's Health*. 1996.

7. Deutchman, M. and M. Wulster-Radcliffe, Stress Urinary Incontinence in Women: Diagnosis and Medical Management. MedGenMed, 2005. **7**: p. 62.

8. Tinker, A., *Women's health: the unfinished agenda.* International Journal of Gynecology & Obstetrics, 2000. **70**(1): p. 149-158.

9. Shah, A.D., N. Kohli, and L. Hoyte, *The age distribution, rates, and types of surgery for pelvic organ prolapse in the USA.* International Urogynecology Journal, 2008. **19**(3): p. 421-428.

10. Bidmead, J., *Incontinence and Prolapse-An Integrated View* European Urology Supplements, 2002. **1**(10): p. 33-37.

11. MARINKOVIC, S.P. and S.L. STANTON, *Incontinence and Voiding Difficulties Associated With Prolapse* The Journal of Urology, 2004. **171**(3): p. 1021-1028.

12. Mouritsen, L., *Classification and evaluation of prolapse* Best Practice and Research Clinical Obstetrics and Gynaecology, 2005. **19**(6): p. 895-911.

13. Shafik, A., Dilatation and closing urethral reflexes: Description and clinical significance of new urethral reflexes. preliminary report World Journal of Urology, 1996. **9**(2): p. 105-108.

14. Matthew, D.B., *Contempory views on female pevlic anantomy.* Cleveland Clinic Journal of Medicine, 2005. **72**(4).

15. Wallner, C., et al., *Levator ani has a crucial role in the maintenance of continence* European Urology Supplements, 2009. **55**(4): p. 932-944.

16. Aung, H.H., et al., Anatomical study of the obturator internus, gemelli and quadratus femoris muscles with special reference to their innervation The Anatomical Record, 2001. **263**(1): p. 41-52.

17. Yu, J.S., *Hip and Femur Trauma* SEMINARS IN MUSCULOSKELETAL RADIOLOGY, 2000. **4**(2): p. 205-220.

18. Elsner, P., *Anatomy, physiology and microbiology of the vulva and the vagina.* Journal of the European Academy of Dermatology and Venereology, 1995. **5**: p. 64.

19. Kovac, S.R. and C.W. Zimmerman, *Advances in reconstructive vaginal surgery*. 2006.

20. Krasnopolskji, V.I., L.I. Titchenko, and N.V. Dub, *3D-Ultrasound diagnostics in the determination of normal bladder anatomy and at the incontinence.* International Journal of Gynecology and Obstetrics, 2000. **70**: p. 75.

21. Ellis, H., *Anatomy of the uterus.* Anaesthesia and Intensive Care Medicine, 2005. **6**(3): p. 74-75.

22. Heald, R.J. and B.J. Moran, *Embryology and anatomy of the rectum.* Seminars in Surgical Oncology, 1998. **15**(2): p. 66-71.

23. Gray, H., Anatomy of the Human Body. 1918.

24. Fielding, J.R., et al., MR-Based Three Dimensional Modeling of the Normal Pelvic Floor in Women Quantification of Muscle Mass. American Journal of Roentgenology, 2000. **174**(3): p. 657-660.

25. Parikh, M., et al., *Three Dimensional Virtual Reality Model of the Normal Female Pelvic Floor.* Annals of Biomedical Engineering, 2004. **32**(2): p. 292-296.

26. Manetta, C. and R. Blade, *Glossary of Virtual Reality Terminology.* International Journal of Virtual Reality, 1995. **1**(2).

27. Popovic, A., et al., *Statistical validation metric for accuracy assessment in medical image segmentation* International Journal of Computer Assisted Radiology and Surgery, 2007. **2**(3): p. 169-181.

28. Rankin, S.C., *CT and MRI.* Surgery (Oxford), 2005. **23**(5): p. 162-165.

29. Davies, R., *Multislice CT.* Australasian Radiology, 2002. **46**(4): p. 450.

30. Meyers, M.A., *3D CT imaging in clinical practice.* Abdominal Imaging, 2009. **34**(2): p. 1-2.

31. Novelline, R., *Squire's Fundamentals of Radiology*. 5th ed: Harvard University Press.

32. Storto, M.L., *Diseases of the Heart, Chest & Breast*. Current Approaches to Imaging Acute and Chronic Airway Disease ed. J. Hodler, C.L. Zollikofer, and G.K.v. Schulthess. Vol. 1. 2007: Springer Milan.

33. Roos, A.d., et al., *Cardiac applications of multislice computed tomography* British Journal of Radiology, 2006. **79**: p. 9-16.

34. Martin, D.R. and R.C. Semelka, *Health effects of ionising radiation from diagnostic CT.* The Lancet, 2006. **367**(9524): p. 1712-1724.

35. Olstad, B. and H. Torp, *Real-time display of ultrasound in slow motion.* The Journal of the Acoustical Society of America, 2002. **112**(3): p. 795.

36. Valdueza, J.M., et al., Examination technique and normal values of the intracranial veins: A transcranial Doppler ultrasound study. Journal of the Neurological Sciences, 1997. **150**: p. 193.

37. Devlin, V.J., *Spine Secrets*. 2003.

38. Andrews, C., A. Simmons, and S. Williams, *Magnetic resonance imaging and spectroscopy.* Physics Education, 1996. **31**(2): p. 80-85.

39. Beutel, J., H.L. Kundel, and R.L.V. Metter, *Handbook of Medical Imaging*. Physics and Psychophysics. Vol. 1. 2000, Bellingham: SPIE. 949.

40. Bae, J.-H., et al., *The fabrication of superconducting magnet for MRI.* Physica C, 2002. **372**: p. 1342-1345.

41. Olabarriaga, S.D. and A.W.M. Smeulders, *Interaction in the segmentation of medical images: A survey.* Medical Image Analysis, , 2001. **5**(2): p. 127-142.

42. Chen, L., et al., Measurement of the pubic portion of the levator ani muscle in women with unilateral defects in 3-D models from MR images. International Journal of Gynecology and Obstetrics, 2005. **92**: p. 234-241.

43. Hannah, I., D. Patel, and R. Davies, *The use of variance and entropic thresholding methods for image segmentation.* Pattern Recognition, 1995. **28**(8): p. 1135-1143.

44. Erdi, Y.E., et al., Segmentation of lung lesion volume by adaptive positron emission tomography image thresholding Cancer, 1997. **80**(12): p. 2505 - 2509.

45. Sifre-Maunier, L., et al., A global unimodal thresholding based on probabilistic reference maps for the segmentation of muscle images Image and Vision Computing, 2006. **24**(10): p. 1080-1089.

46. Zahara, E., S.-K.S. Fan, and D.-M. Tsai, *Multiresolution MRI Brain Image Representation and Segmentation.* Pattern Recognition Letters, 2005. **26**(8): p. 1082-1095.

47. Ding, L. and A. Goshtasby, *On the Canny edge detector.* Pattern Recognition 2001. **34**(3): p. 721-725.

48. Ishak, N.F., R. Logeswaran, and W.-H. Tan, *Artifact and noise stripping on low-field brain MRI.* INTERNATIONAL JOURNAL OF BIOLOGY AND BIOMEDICAL ENGINEERING, 2008. **2**(2): p. 59-68.

49. Ding, L. and A. Goshtasby, *On the Canny edge detector.* Pattern Recognition, 2001. **34**(3): p. 721-725.

50. Cinque, L., G. Foresti, and L. Lombardi, *A clustering fuzzy approach for image segmentation.* Pattern Recognition, 2004. **37**(9): p. 1797-1807.

51. Liao, L., T. Lin, and B. Li, MRI brain image segmentation and bias field correction based on fast spatially constrained kernel clustering approach. Pattern Recognition Letters, 2008. **4**(4).

52. Mehnert, A. and P. Jackway, *An improved seeded region growing algorithm.* Pattern Recognition Letters, 1997. **18**(10): p. 1065-1071.

53. Xinquan, S., M. Spann, and P. Nacken, Segmentation of 2D and 3D images through a hierarchical clustering based on region modelling. Pattern Recognition, 1998. **31**(9): p. 1295-1309.

54. Maintz, J.B.A. and M.A. Viergever, *A survey of medical image registration.* Medical Image Analysis, 1998. **2**(1): p. 1-36.

55. Lipson, P., et al. Deformable templates forfeature extraction from medical images. in 1st European Conference on Computer Vision. 1990. New York: Springer-Verlag,.

56. Kass, M., A. Witkin, and D. Terzopoulos, *Active contour models.* International Journal of Computer Vision, 1987. **1**(4): p. 321-331.

57. C.A., D. and P.J. L., *An Active Contour Model for Mapping the Cortex.* IEEE TRANSACTIONS ON MEDICAL IMAGING MI, 1995. **14**(1): p. 65.

58. Kauffmann, C., B. Godbout, and J.A. De Guise, *Simplified Active Contour Model applied to bone structure segmentation in digital radiographs.* PROCEEDINGS-SPIE THE INTERNATIONAL SOCIETY FOR OPTICAL ENGINEERING, 1998. **1**(3338): p. 663-672.

59. Ray, N., et al., Merging Parametric Active Contours Within Homogeneous Image Regions for MRI-Based Lung Segmentation. IEEE TRANSACTIONS ON MEDICAL IMAGING MI, 2003. **22**(2): p. 189-199.

60. Staib, L.H. and J.S. Duncan, *Boundary finding with parametrically deformable models.* IEEE Transactionson Pattern Analysis and Machine Intelligence, 1992. **14**(11): p. 1061-1075.

61. Szekely, G., et al., Segmentation of 2-d and 3-d objects from mri volumedata using constrained elastic deformations of flexible fourier contour and surface models. Medical Image Analysis, 1996. **1**: p. 19-34.

62. Brock, K.K., et al., Accuracy of finite element model-based multi-organ deformable image registration. Medical Physics, 2005. **32**(6): p. 1647-1659.

63. Pentland, A.P. and S. Sclaroff, *Closed-form solutions for physically based modelling and recognition.* IEEETransactions on Pattern Analysis and Machine Intelligence, 1991. **13**(7): p. 715-729.

64. T.F.Cootes and C.J.Taylor, *Combining point distribution models with shape models based on finite element analysis.* Proc. British Machine Vision Conference, 1994: p. 419-428.

65. Dryden, I. and K.V. Mardia, *The Statistical Analysis of Shape*. 1998, London: Wiley.

66. Cootes, T.F., et al., *Active Shape Models - Their Training and Application.* Computer Vision and Image Understanding, 1995. **61**(1): p. 38-59.

67. K.Babalola, et al., Comparison and Evaluation of Segmentation Techniques for Sub-cortical Structures in Brain MRI. Proc. MICCAI, 2008. **1**: p. 409-416.

68. Thodberg, H.H. and A. Rosholm, *Application of the active shape model in a commercial medical device for bone densitometry* Image and Vision Computing, 2003. **21**(13-14): p. 1151-1161.

69. Lötjönen, J., et al., Artificial Enlargement of a Training Set for Statistical Shape Models: Application to Cardiac Images. Proc. Functional Imaging and Modelling of the Heart, 2005: p. 92-101.

70. Kitasaka, T., et al., Lung area extraction from 3D chest X-ray CT images using a shape model generated by a variable Bezier surface Systems and Computers in Japan, 2003. **34**(4): p. 60-71.

71. Edwards, G.J., T.F. Cootes, and C.J. Taylor. Face Recognition Using Active Appearance Models. in Proc. European Conference on Computer Vision 1998: Springer.

72. Edwards, G.J., T.F. Cootes, and C.J. Taylor, *Advances in Active Appearance Models.* Proc International Conference on Computer Vision, 1999: p. 137-142.

73. Bankman, I.N., Handbook of Medical Image Processing and Analysis 2nd ed. 2008. 984.

74. Duncan, J.S. and N. Ayache, *Medical Image Analysis: Progress over Two Decades and the Challenges Ahead.* IEEE Transactions on Pattern analysis and machine intelligence, 2000. **22**(1): p. 85-106.

75. Maintz, J.B.A. and M.A. Viergever, *A Survey of Medical Image Registration.* Medical Image Analysis, 1998. **2**(1): p. 1-16.

76. Ayache, N., *Medical Computer Vision, Virtual Reality and Robotics.* Image and Vision Computing, 1995. **13**(4): p. 295-313.

77. Heinone, T., et al., *Semi-automatic tool for segmentation and volumetric analysis of medical images* Medical and Biological Engineering and Computing, 1998. **36**(3): p. 291-296.

78. Zhang, H., J.E. Fritts, and S.A. Goldman, *Image segmentation evaluation: A survey of unsupervised methods* Computer Vision and Image Understanding, 2008. **110**(2): p. 260-280.

79. Clarke, L., R. Velthuizen, and J. MA Camacho, *MRI segmentation: methods and applications.* Magnetic Resonance Imaging, 1995. **13**(3): p. 343-368.

80. Brandon, C.J., et al., *Anatomy of the perineal membrane as seen in magnetic resonance images of nulliparous women* American Journal of Obstetrics and Gynecology, 2009. **200**(5): p. 583.e1-583.e6.

81. Shi, J. and J. Malik, *Normalized Cuts and Image Segmentation.* IEEE TRANSACTIONS ON PATTERN ANALYSIS AND MACHINE INTELLIGENCE PAMI, 2000. **22**(8): p. 888-905.

82. Agaian, S., et al., Transform Coefficient Histogram-Based Image Enhancement Algorithms Using Contrast Entropy. IEEE TRANSACTIONS ON IMAGE PROCESSING, 2007. **16**(3): p. 741-758.

83. Styner, M.A., et al., *Evaluation of 3D Correspondence Methods for Model Building* Vol. 0302-9743. 2003: Springer Berlin / Heidelberg.

84. Sclaroff, S. and L. Liu, *Deformable Shape Detection and Description via Model-Based Region Grouping.* IEEE TRANSACTIONS ON PATTERN ANALYSIS AND MACHINE INTELLIGENCE PAMI, 2001. **23**(5): p. 475-489.

85. Kamber, M., et al., Model-Based 3D Segmentation of Multiple Sclerosis Lesions in Dual-Echo MRI Data. Proceedings of SPIE Wells 1992. **1808**.

86. Rajapakse, J.C., J.N. Giedd, and J.L. Rapoport, *Statistical Approach to Segmentation of Single-Channel Cerebral MR Images.* IEEE TRANSACTIONS ON MEDICAL IMAGING MI, 1997. **16**(2): p. 176-186.

87. Ahmad, T., et al. Tracking and Recognising Hand Gestures using Statistical Shape Models. in Proc. British Machine Vision Conference. 1995.

88. R.H.Davies, et al., *Building optimal 2D Statistical Shape Models.* Image and Vision Computing, 2003. **21**: p. 117-182.

89. Tingelhoff, K., et al., *Analysis of manual segmentation in paranasal CT images* European Archives of Oto-Rhino-Laryngology, 2008. **265**(9): p. 1061-1070.

90. Pekar, V., T.R. McNutt, and M.R. Kaus, *Automated model-based organ delineation for radiotherapy planning in prostatic region* International Journal of Radiation Oncology, Biology,Physics., 2004. **60**(3): p. 973-980.

91. Yang, H., et al. Evolution of T-Spline Level Sets with Distance Field Constraints for Geometry Reconstruction and Image Segmentation. in International Proceedings of the IEEE International Conference on Shape Modeling and Applications. 2006. Washington: IEEE Computer Society

92. Aggarwal, J.K., R.O. Duda, and A. Rosenfeld, *Computer methods in image analysis* 1977: IEEE Computer Society. 466.

93. Frisken, S.F. and R.N. Perry, Designing with Distance Fields in International Conference on Shape Modeling and Applications 2005 2005: Cambridge, Massachusetts

94. Payne, B.A. and A.W. Toga, *Distance Field Manipulation of Surface Models.* IEEE Computer Graphics, 1992. **12**(1): p. 65-71.

95. Zheng, Z., et al., *Facial feature localization based on an improved active shape model* Information Science, 2008. **178**(9): p. 2215-2223.

96. Nawaz, T., K.A. Qazi, and M.I. Ashraf, *Performance Evaluation of Noise Removal Algorithms for Scanned Images.* International Journal of Computer Science and Security, 2008. **3**(3): p. 226-228.

97. Juell, P. and R. Marsh, *A hierarchical neural network for human face detection.* PATTERN RECOGNITION, 1996. **29**(5): p. 781-788.

98. Frakes, W.B. and R. Baeza-Yates, *Information Retrieval, DataStructure and Algorithms*. 1992: Prentice Hall.

99. Roy, R.K., Design of experiments using the Taguchi approach. 2001: John Wiley & Sons Inc.

100. Roy, R.K., *A primer on the Taguchi method* 1990: SME. 247.

101. Tile, M., D. L.Helfet, and J. F.Kellam, *Fractures of the pelvis and acetabulum* 2003, philadephia: Lippincott williams & Wilkins. 830.

102. Cardozo, L. and D. Staskin, *Textbook of female urology and urogynecology*. 2 ed. Vol. 1. 2006: Informa Healthcare. 1415.

103. Baba, K. and D. Jurkovic, *Three-dimensional ultrasound in obstetrics and gynecology* 1997: The Parthenon Publishing Group Inc. 110.

104. Levienaise-Obadia, B. and A. Gee, *Adaptive segmentation of ultrasound images* Image and Vision Computing, 1999. **17**(8): p. 583-588.

105. Aukee, P., J.-P. Usenius, and P. Kirkinen, *An evaluation of pelvic floor anatomy and function by MRI.* European Journal of Obstetrics and Gynecology and Reproductive Biology, 2004. **112**(1): p. 84-88.

106. Handa, V.L., et al., Magnetic resonance assessment of pelvic anatomy and pelvic floor disorders after childbirth International Urogynecology Journal, 2009. **20**(2): p. 133-139.

107. Cavagna, F.M., et al., *Trends and developments in MRI contrast agent research* European Radiology, 1997. **7**(14): p. 222-224.

108. Ramaker, H.-J., et al., The effect of the size of the training set and number of principal components on the false alarm rate in statistical process monitoring. Chemometrics and Intelligent Laboratory Systems, 2004. **73**(1): p. 181-187.

109. P. Perona and Malik, *Scale space and edge detection using anisotropic diffusion.* IEEE Transaction. Pattern Analysis, 1990. **12**: p. 629-639.

110. Mortensen, E.N. and W.A. Barrett, *Intelligent scissors for image composition.* SIG-Graph'95, 1995.

111. Klein, F., Elementary Mathematics from an Advanced Standpoint: Geometry. 2004: Dover Publications, Inc.

112. Cottle, R. and C.E. Lemke, *Nonlinear programming*. 1975: American Mathematical Society.

113. Buessler, J.-L. and J.-P. Urban, *Visually guided movements: learning with modular neural maps in robotics* Neural Networks, 1998. **11**(7-8): p. 1395-1415.

114. Fabbri, R., et al., *2D Euclidean distance transform algorithms: A comparative survey* ACM Computing Surveys (CSUR), 2008. **40**(1): p. 1-44.

115. Ritter, G.X. and J.N. Wilson, *Handbook of computer vision algorithms in image algebra*. 2001: CRC Press LLC.

116. Ye, Q.-Z., The signed Euclidean distance transform and its applications. Pattern Recognition, 1988. **1**: p. 495-499.

117. Shih, F.Y., Image Processing and Mathematical Morphology: Fundamentals and Applications. 2009: CRC Press LLC.

118. Jolliffe, I.T., *Principal component analysis*. 2002: Springer.

119. Li, Z., Y. Xuan-dong, and L. Kai-yang, *Digitization and DICOM standardization of X-ray image signal.* Wuhan University Journal of Natural Sciences, 2008. **9**(4): p. 463-467.

120. Mildenberger, P., M. Eichelberg, and E. Martin, *Introduction to the DICOM standard.* European Radiology, 2002. **12**(4): p. 920-927.

121. Flanders, A.E. and J.A. Carrino, *Understanding DICOM and IHE.* Seminars in Roentgenology, 2003. **38**(3): p. 271-281.

122. McRobbie, D.W., E.A. Moore, and M.J. Graves, *MRI From Picture to Proton*. 2003: Cambrige University Press.

123. Gonzales, R.C., R.E. Woods, and S.L. Eddins, *Digital Image Processing Using Matlab*. 2004: Pearson Education Inc.

124. Kim, D.-H. and E.-Y. Cha, *Intensity surface stretching technique for contrast enhancement of digital photography.* Multidimensional Systems and Signal Processing, 2009. **20**(1): p. 81-95.

125. Goshtasby, A., *Piecewise linear mapping functions for image registration* Pattern Recognition, 1986. **19**(6): p. 459-466.

126. Feissel, M. and W. Lewandowski, *A comparative analysis of Vondrak and Gaussian smoothing techniques.* Pattern Recognition, 1984. **58**(4): p. 464 - 474.

127. Caselles, V., et al., A Geometric Model for Active Contours in Image Processing Recovery. Numer. Math., 1993. **66**.

128. Doncker, E.d., A. Gupta, and G. Greenwood, *Applications of evolutionary strategies to finegrained task scheduling.* Parallel Processing Letters, 1996. **6**(4): p. 551-561.

129. Dianati, M., I. Song, and M. Treiber, An introduction to genetic algorithms and evolution strategies. 2002.

130. Zhang, Y.J., *Evaluation and comparison of different segmentation algorithms.* Pattern Recognition Letters, 1997. **18**(10): p. 963-974.

131. Heimann, T., et al., *Empirical discrepancy measures for the evaluation of segmentation results.* International Congress Series, 2004. **12**(68): p. 1276.

132. Pan, L.K., B.D. Chang, and D.S. Chou, *Optimization for solidification of low-level-radioactive resin using Taguchi analysis.* Waste Management, 2001. **21**(8): p. 767-772.

133. Maghsoodloo, S., et al., Strengths and limitations of taguchi's contributions to quality, manufacturing, and process engineering. Journal of Manufacturing Systems, 2004. **23**(2): p. 73-126.

134. Pan, L.K., et al., *Optimizing multiple quality characteristics via Taguchi method-based Grey analysis.* Journal of Materials Processing Tech, 2007. **182**(1-3): p. 107-116.

135. Brue, G. and R.G. Launsby, *Design for Six Sigma* 2003: McGraw-Hill Professional. 193.

136. J.Lo, et al., Design, manufacturing and applications of composites: proceedings of the 4th joint canada-japan workshop on composites. 4th ed. 2002, Vancouver: CRC Press. 552.

137. Ross, P.J., *Taguchi techniques for quality engineering*. 1996: The McGraw-Hill Companies.

138. Barker, T.B., Engineering quality by design: interpreting the Taguchi approach. 1990: Marcel Dekker, Inc. 225-250.

139. Ostergard, D.R., et al., *Ostergard's urogynecology and pelvic floor dysfunction*. 2003: Lippincott Williams & Wilkins.

140. Macura, K.J., *Magnetic Resonance Imaging of Pelvic Floor Defects in Women.* Topics in Magnetic Resonance Imaging, 2006 **17**(6): p. 417-426.

141. saleem, Z. and G. Goelman, *Complex denoising of MR data via wavelet analysis: Application for functional MRI.* Magnetic Resonance Imaging, 2000. **18**(1): p. 59-68.

142. Itai, Y., et al., Automatic detection of blood vessels from CTA images employing morphological operation. Artificial Life and Robotics, 2009. **13**(2): p. 428 - 433.